

POLITECNICO DI TORINO

¹ Politecnico di Torino, Dipartimento di Ingegneria Meccanica e Aerospaziale
Corso Duca degli Abruzzi, 24 – 10129 Torino, Italy

Corso di Laurea Magistrale in Ingegneria Meccanica

Tesi di Laurea Magistrale

Performance of a Planetary Magnetic Gear for Powertrain Applications



Relatori

Prof. Elvio Bonisoli
Prof. Maurizio Repetto
Dott. Luca Dimauro

Candidato

Stefano Oggeri

Aprile 2022

Performance of a Planetary Magnetic Gear for Powertrain Applications

Stefano Oggeri

¹ Politecnico di Torino, Department of Mechanical and Aerospace Engineering
Corso Duca degli Abruzzi, 24 – 10129 Torino, Italy

Acknowledgments

Questo lavoro di tesi rappresenta la conclusione del mio percorso accademico presso il Politecnico di Torino, un percorso lungo e impegnativo che mi ha aiutato a sviluppare conoscenze e a formarmi anche nell'approccio ai problemi in diversi ambiti, un percorso tortuoso ma ricco di soddisfazioni.

Un primo ringraziamento va alla mia famiglia: i miei genitori, mio fratello Enrico, mia nonna, i miei zii e cugini. Grazie per aver sempre creduto in me e per avermi sostenuto anche nelle difficoltà nel raggiungere questo obiettivo.

Ci tengo a ringraziare Micol, la mia ragazza, che è stata al mio fianco dal primo giorno e che mi ha supportato e sopportato nel bene e nel male.

Ringrazio gli amici di una vita e le persone conosciute durante il percorso per i momenti di svago e serenità altrettanto importanti per arrivare al traguardo.

Nell'ambito di ricerca, ringrazio il mio relatore di tesi, il Prof. Elvio Bonisoli, per avermi dato questa stimolante opportunità di crescita e per preoccuparsi della maturazione delle persone con cui lavora.

Ringrazio molto il Dott. Luca Dimauro, relatore che mi ha seguito passo dopo passo nel lavoro ed è sempre stato disponibile ad aiutarmi e a confrontarsi.

Ringrazio inoltre il Prof. Maurizio Repetto, relatore di tesi per la disponibilità e l'opportunità fornitami, l'Ing. Paolo Squillari per il supporto tecnico e tutti i collaboratori e il personale del dipartimento per il loro lavoro e aiuto.

Index

Abstract	7
1. State of the art and literature review	8
1.1 Magnetic gear history.....	8
1.2 Comparison with mechanical gears	12
1.3 Functioning principles.....	13
2. Prototype in study	17
2.1 Selected structure	17
2.2 Test rig components	23
2.2.3 Frame	24
2.2.4 Motors	25
2.2.5 Torque transducers	26
2.2.6 Incremental encoders	27
2.3 LabView software	29
3. Experimental tests	32
3.1 Design of Experiments (Doe)	32
3.2 Engaged gearbox operation.....	39
3.2.1 No-load tests	39
3.2.1.1 Acquisitions.....	39
3.2.1.2 Signals filtering	40
3.2.1.3 Torque loss	42
3.2.2 Loaded tests.....	46
3.2.2.1 Acquisitions.....	46
3.2.2.2 Signals filtering	46
3.2.2.3 Efficiency of the magnetic gear	46
3.2.2.4 Internal efficiency	47
3.2.2.5 Mean efficiency	55
3.2.3 Loss contributions	64
3.2.3.1 Mechanical efficiency	70
3.2.3.2 Magnetic efficiency.....	71
3.2.3.3 Total efficiency	72
3.2.4 Efficiency considering the no-load data.....	72
3.2.5 Functional failure	73
3.2.6 Conclusions	76
3.3 Neutral gear.....	77
3.3.1 Neutral operation.....	77
3.3.2 Old data	78
3.3.2.1 Acquisitions.....	78
3.3.2.2 Signals filtering	78
3.3.2.3 Torque losses.....	78
3.3.2.4 Interpolation	81
3.3.3 New data	83
3.3.3.1 Acquisitions.....	83
3.3.3.2 Signals filtering	83
3.3.3.3 Torque losses.....	83
3.3.4 Curve fitting	86
3.3.5 Alternative curve fitting	88
3.3.6 Conclusions	90
4. Efficiency contributions	91

4.1 Efficiencies using neutral tests.....	91
4.1.2 Mechanical efficiency	92
4.1.3 Magnetic efficiency.....	101
4.2 Conclusions.....	112
5. Final conclusions.....	113
Reference	115

Abstract

The aim of this thesis is the analysis of the dynamic behaviour and performance of an innovative power transmission system, based on the technology of magnetic gears.

The magnetic gear has the capability to transmit motion and torque in a contactless way between two coaxial rotors with permanent magnets through the interaction with a modulator element holding ferromagnetic poles. Several potential benefits can be achieved using this technology, as the reduction of noise, wearing and vibrations, and the absence of lubrication, which are typical of mechanical power transmission systems.

This transmission device is called planetary magnetic gear (PMG), due to its topological and functional similarity with a planetary mechanical gearing device, from which the same working principles are derived. In previous research works, a test bench for testing the magneto-mechanical efficiency of the PMG prototype has been designed and realised. The PMG can be tested in different configurations, with regards to the input/output power, and using two different transmission gear ratios. The starting point of this thesis was the development of a design of experiment (DoE) of the experimental tests, which have been carried out on the PMG prototype at different loads, different rotational speeds, different transmission ratios and different working conditions (speed reducer or speed amplifier) to prove that the efficiency is practically independent from the power direction, in contrast with the traditional mechanical transmissions. Moreover, a methodology for the evaluation of transmission efficiency has been developed, for a complete characterisation of the magneto-mechanical properties. Tests in load and no engagement condition have been carried out to characterise the mechanical dissipations, due to friction inside the bearings, in order to obtain the two contributions of mechanical and magnetic efficiency. Mechanical and electromagnetic quantities are collected and then analysed in the post-processing phase.

For the sake of clarity, the rotational speeds of input and output shafts are acquired using two incremental magnetic encoder, two torque sensors are used to collect the torque values at the two sides of transmission, while an oscilloscope is used to evaluate the magnetic flux inside the device. The LabView software is used to control and manage the experimental tests, allowing the two electric motors to work in speed or torque control, supplying power, or applying a resistive torque. Eventually, the MATLAB software is used for data post-processing.

The results of the data analysis and post-processing has helped to gain insight into the operation of the magnetic gear and to draw convergent conclusions for all the different conditions tested, regarding how losses are distributed and how efficiency trends. Starting from this point, and therefore knowing the strengths of this technology, new studies can be performed to even better the performance.

Chapter 1

1. State of the art and literature review

Magnetic gears are alternative power transmission systems to the widespread mechanical gears. The principle behind this technology relies on the removal of physical contact between the active parts, which have magnetic properties, to guarantee a magnetic interaction in order to generate torque. In this way, the magnetic gearbox operates not only in substitution to the mechanical gearbox, but also removing the need for other two complex components such as the clutch and the torque limiter. The possible applications for this technology are many, going from space and marine to industrial and wind energy [1] [2] [3], even if the target for the prototype analysed is the powertrain field.

1.1 Magnetic gear history

The technology of magnetic gears has been thought of since the early 1900s, when Armstrong described the first electromagnetic spur gear [4], as his aim was the development of a contactless power transmission starting from a standard mechanical gear and adding coils to the teeth. Then, in 1941, H. T. Faus was the first to develop a real concept using permanent magnets with a similar design to mechanical gears (Figure 1.1) [5].

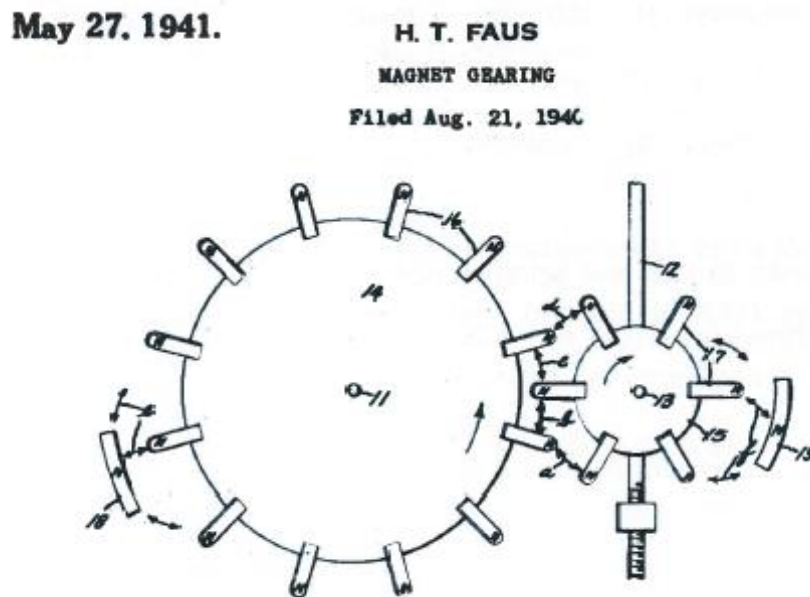


Figure 1.1 – Scheme of Faus’s magnetic gear patented in 1940, resembling a mechanical spur gear with magnets instead of teeth.

However, for a long time this technology did not see great improvements given the fact that the results in terms of torque were not comparable to the mechanical counterpart. The main reasons are found in the poor geometric configuration properties, still too reliant on mechanical gear design, so that only one couple of magnets at a time would produce torque, and in the use of ferromagnetic permanent magnet rotors that limited performance. In fact, almost all possible mechanical gearing combinations can be converted into the magnetic one, as illustrated in Figure 1.2.

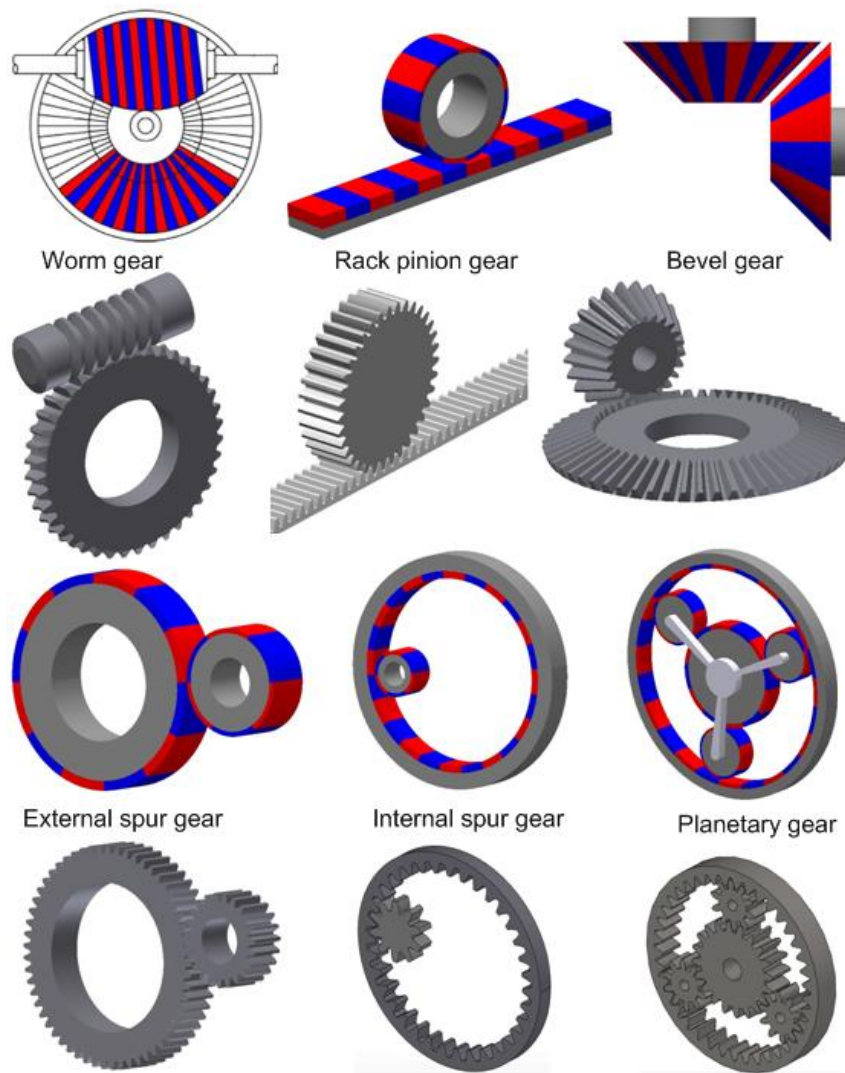


Figure 1.2 – mechanical gear topologies and magnetic counterparts tried and tested.

One of the main improvements in the technology of magnetic gears was made in the 1980s when the ferric permanent magnets have been substituted with rare earth compounds like neodymium iron boron (NdFeB). In fact, ferrite has a significantly low flux density and low maximum energy production compared to rare earth as data comparing the two suggests [6]. The NdFeB permanent magnets have one of the best torque density performance among rare earths materials for magnets [7].

This improvement did not come without costs: the rare earths have a significantly higher price than most ferromagnetic materials such as ferrite and are less abundant. For this reason, many tries have been made to optimize material usage to save money and space without sacrificing the performance. For example, a reduction in PM material alone or a blend of rare earths and ferrite in what is called a hybrid approach has been made [8].

Another aspect to consider is the fact that the NdFeB alloy can come with the addition of dysprosium, a heavy metal with high costs, or without; in this last case, the alloy can either have high torque density and high risk of demagnetization, or low torque density and lower risk of demagnetization, so the choice is articulated [9].

Between these years and the end of the 20th century, many projects and patents have been released, especially trying the previously displayed designs: the most notable are the cylindrical gear of Hetzel (1974) [10], the planetary gear by Mabe (1991) [11], the worm gear by Kikuchi and Tsurumoto (1993) [12] and the bevel gear by Yao et al. (1996) [13].

Several researchers have explored the world of magnetic gears up to 2001 when Atallah and Howe created a new geometry: they started from the design of a planetary gear (PMG) and exported it to the magnetic counterpart. The difference lies in the planetary portion: the planets are substituted with a concentric carrier mounted with ferromagnetic pole-pieces, as shown in Figure 1.3 [14]. The peculiar aspect of this type of design is that it can function in three different ways: by keeping either the outer ring, the intermediate carrier, or the inner ring still, while letting the other two parts free to rotate.

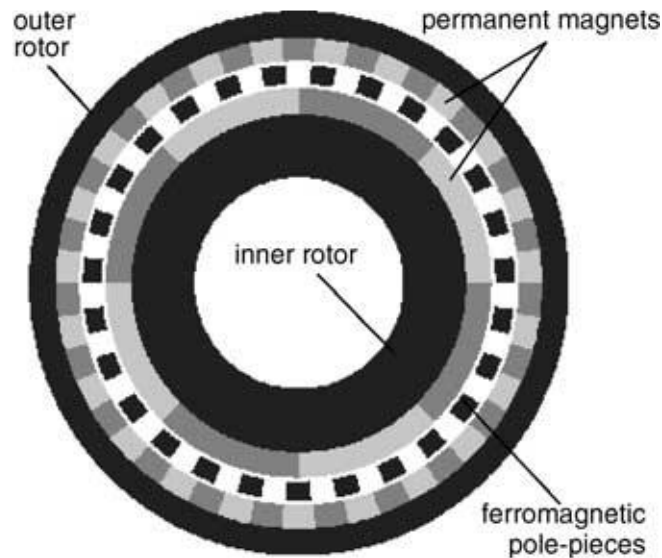


Figure 1.3 – Atallah and Howe’s model of concentric magnetic gear.

Moreover, in the solution with the static carrier the magnetic gear works with formulas that are similar to the ones for a mechanical spur gear [15], with the number of pole pairs on the rotor having the same role as the number of teeth for a toothed wheel.

This solution has shown to be the best so far, giving torque densities comparable with mechanical gears. Thus, it is the one used in this case.

This innovation enters in a new category of magnetic gears that doesn’t precisely mimic the mechanical gear functioning but is instead driven by the modulation of the magnetic flux between the rotating components. This type of operation cannot be translated in a mechanical counterpart and is at the same time the best in terms of performance so far (Figure 1.4) [9].

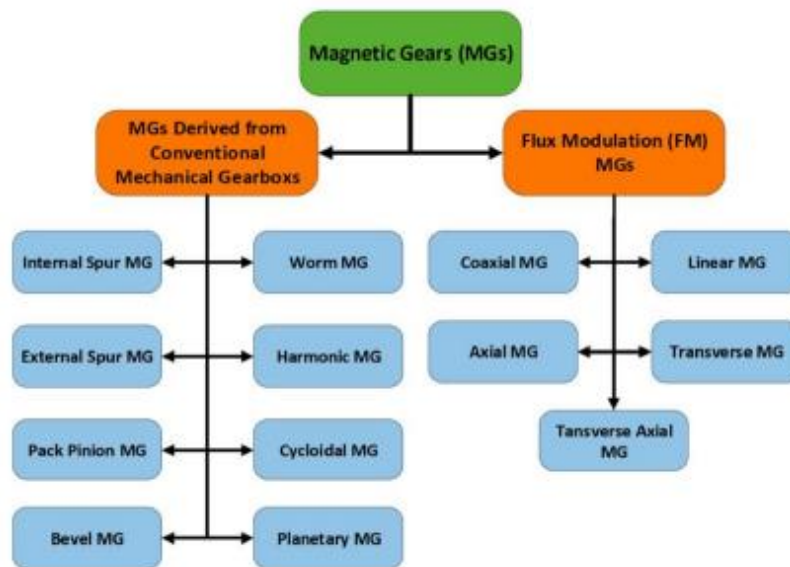


Figure 1.4 – Possible classification of MGs based on the direct interaction between magnetic fluxes (mechanical gear mimicking) or their modulation.

The overcoming of the main problems has led to an increase in interest for this type of technological solution, as the number of publications show in Figure 1.5 [16].

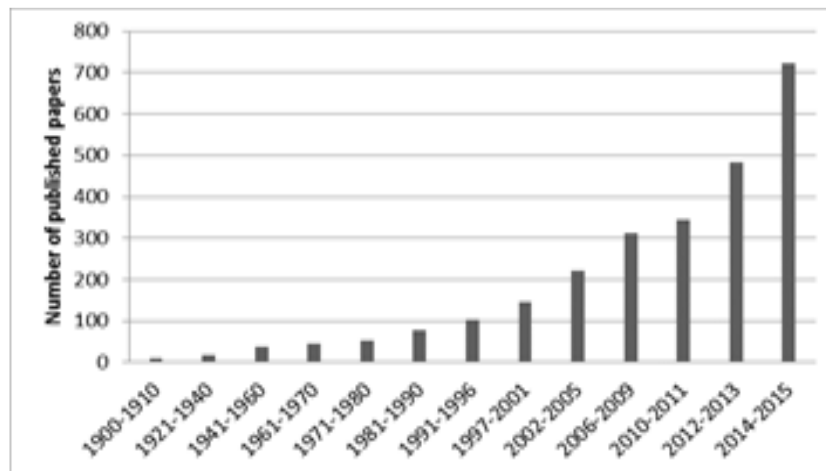


Figure 1.5 – evolution of the number of publications regarding magnetic gears between 20th and 21st century.

Nevertheless, some problems occur till these days: it is possible that the results obtained from a simulation before testing the component itself on the test bench produce a certain result that then is seen to be less performing in the real case scenario. Permanent magnets, in fact, have the risk of demagnetization over time [17].

1.2 Comparison with mechanical gears

Mechanical gears are an excellent mean to transmit motion thank to their torque density capabilities and for this reason they are used in all sorts of applications, but they also have some drawbacks concerning the life of the components and their wear, potentially leading to higher maintenance costs [18] [19]. The torque density gives a relativised torque capacity to the volume occupied for a machine and is therefore expressed in kNm/m^3 . In this way, it is possible to compare different machine with different sizes [20].

So, the introduction of magnetic gears results in potential benefits for a variety of reasons: first of all, the most evident difference from the mechanical gears is the total absence of contact between the parts of the gear. This has huge effects regarding reduced noises and vibrations, which can be a serious limiting factor in many applications. It also means that there is a greatly limited friction (being the rolling bearings the only left source for it) and therefore absence of lubrication need and minimized maintenance and damages. No contact also means that, in case of overload on the input or the output shaft, the two parts would slide not causing any physical damage. Another important factor is that peak torque transmission before reaching sliding is transmitted precisely [21] [22]. The contactless transmission even allows for slight axial misalignment. All of these factors can be summarized in one concept: the magnetic gearbox has a level of internal independence of the two sides that the mechanical gearbox doesn't have.

As previously stated, the most limiting factors are the scarcity of the raw materials for the construction of the gear and the low torque density intrinsic in the technology. Both problems have been solved to a great degree, and today magnetic gears can be a valid alternative to traditional mechanical gears. The delay in the development of this technology is the main reason why it is not widespread yet.

Some comparative values are given in Table 1.1.[23].

Table 1.1 – Torque densities of different gears, both mechanical and magnetic.

Gear type	Torque density (kNm/m^3)
Mechanical spur gear	100-200
Magnetic spur gear	10-20
Magnetic planetary gear	100
Concentric magnetic gear	70-150

It is clear that the chosen design, the concentric magnetic gear, has similar values compared to a mechanical spur gear.

1.3 Functioning principles

The prototype works using first all the laws of electromagnetism which explain, among other behaviours, the magnetic properties of the permanent magnets and the ferromagnetic modulator. The first important equation to describe the system is the second Maxwell equation, the Gauss's law for magnetism:

$$\oint_{\partial V} B \cdot dS = 0 \quad (0.1)$$

with B being the magnetic flux density (or magnetic induction) and dS the surface through which B passes. According to this formulation magnetic monopoles are not possible, and for every magnetic north pole there must be a south pole, therefore the poles of the PMs are counted in pairs.

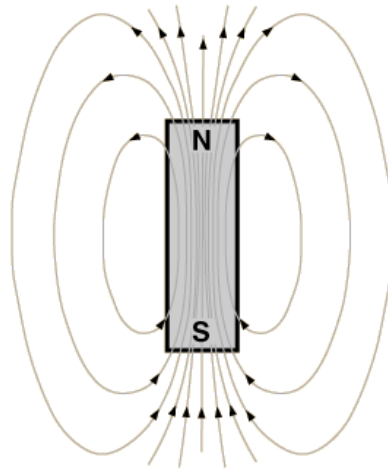


Figure 1.6 – Permanent magnet with magnetic field lines.

The magnetic flux (eq (1.2)) is the key element for the motion: the movement of one of the two rotors given by an input power makes the said flux referred to that specific rotor to vary in space and time. This movement makes the other rotor, whose produced magnetic flux interacts with the first flux, to move as a consequence of the magnetic interaction.

$$\Phi_B = \int_S B \cdot dS \quad (1.2)$$

As previously stated, the chosen functioning consists in the carrier being stationary while the two rings rotate. The characteristics of the permanent magnets, the interaction of their magnetic fluxes and the modulation of the carrier make the two rings rotate in the opposite direction while transmitting motion.

The components are shown in Figure 1.7.

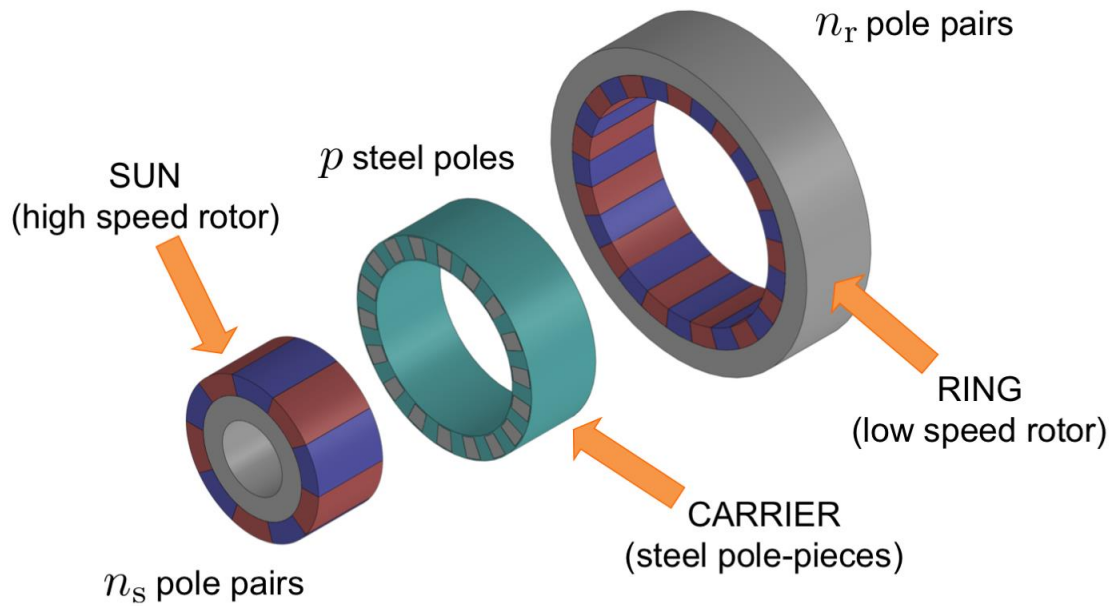


Figure 1.7 – PMG divided in its three concentric untouching components.

The advantage of this configuration is that each permanent magnet on the rotors is simultaneously involved in torque transmission. This potential is maximised if the relative numbers are determined as follows in eq (1.3):

$$p = n_s + n_r \quad (1.3)$$

where:

p : number of ferromagnetic pole-pieces in the static carrier;

n_s : number of rare earth pole-pairs in the sun rotor;

n_r : number of rare earth pole-pairs in the ring rotor,

as the number of pole-pairs generated by either rotor in the space harmonic flux density distribution is:

$$n_{m,k} = |m n + k p| \quad (1.4)$$

where:

n : number of pole-pairs of the other rotor;

m : a natural number;

k : an integer number.

The way in which these pole-pairs are generated is through the modulation of the magnetic flux made by the static carrier as shown in Figure 1.8. The modulation lets only the rotor poles that fully align at a certain moment to the ferromagnetic pole pieces to transmit the magnetic flux [24].

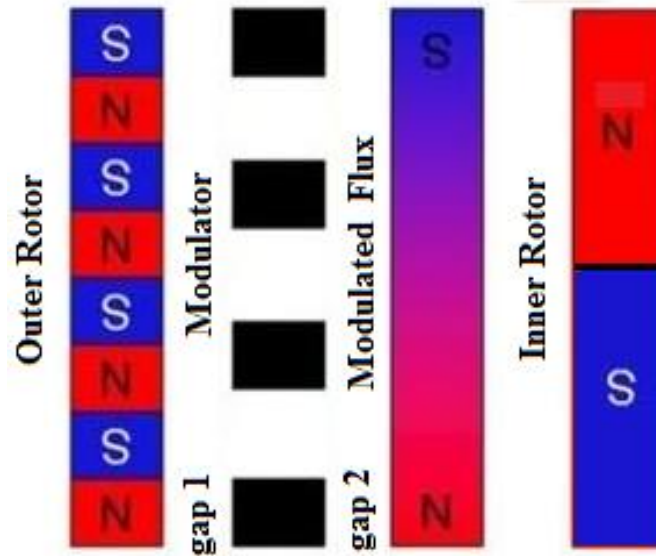


Figure 1.8 – Modulation of the magnetic flux from the outer rotor to the inner rotor through the ferromagnetic pole pieces in the carrier.

This phenomenon happens simultaneously from the outer rotor to the inner rotor and from the inner rotor to the outer rotor. In Figure 1.9 it is possible to see the same principle applied to the circular design used.

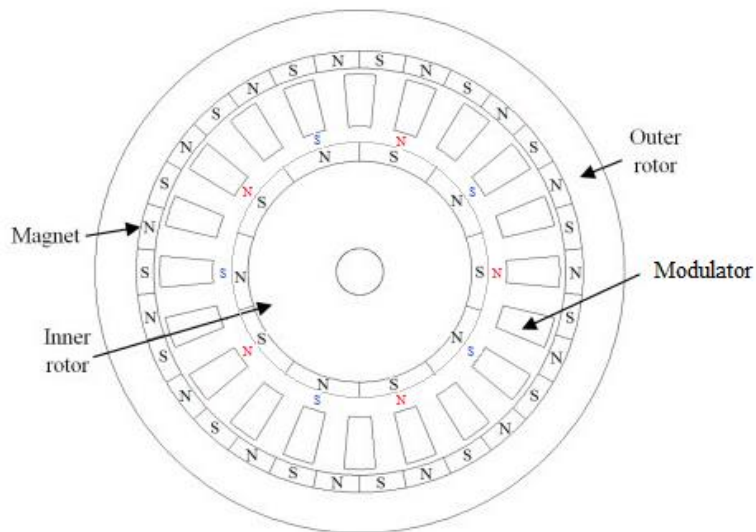


Figure 1.9 – Modulation of the magnetic flux from the outer rotor to the inner rotor through the ferromagnetic pole pieces in the PMG carrier.

Therefore, the speed of either rotor is:

$$\omega_{m,k} = \frac{mn}{mn + kp} \omega \quad (1.5)$$

where:

ω : the speed of the other rotor.

From these values we can easily derive the gear ratio:

$$\tau = \frac{n_r}{n_s} = -\frac{\omega_s}{\omega_r} \quad (1.6)$$

where:

ω_s : rotation speed of the sun;

ω_r : rotation speed of the ring.

The minus sign comes from the fact that the two sides rotate in an opposite direction [4].

This formulation is used both when the input side is the sun and the ring in order to always have a number bigger than the unit for clarity. Given the fact that the ring speed will be chosen as reference, depending on whether the ring side or the sun side is the input side, the gear ratio needs to be multiplied or divided respectively in order to get the other side speed.

Chapter 2

2. Prototype in study

2.1 Selected structure

On the basis of the concentric planetary magnetic gear design, a patented prototype has been realised [25].

This prototype has the opportunity to compete with the “state-of-the-art” mechanical gearboxes since it allows to reduce the physical contact, and therefore the lubrication, to the bearings only, and also permits to perform the gear shift without the use of a clutch and without making noises, reducing wear.

The proposed prototype gearbox has two different gear ratios that are given by two coaxial sets of rotors with different numbers of pole-pairs. The first gear has two concentric rotors, the inner one having 5 pole-pairs and the outer one having 13. The second gear mounts 7 pole-pairs on the inside and 11 pole-pairs on the outside instead. The PMs are made of the rare earth, neodymium alloy previously presented thanks to its capability to remain magnetized through time. The sum adds up to 18 in both cases, which is the number of ferromagnetic pole-pieces in the carrier, made of epoxy resin. The inner rotor is shown in Figure 2.1, the outer rotor in Figure 2.2 and the carrier in Figure 2.3.

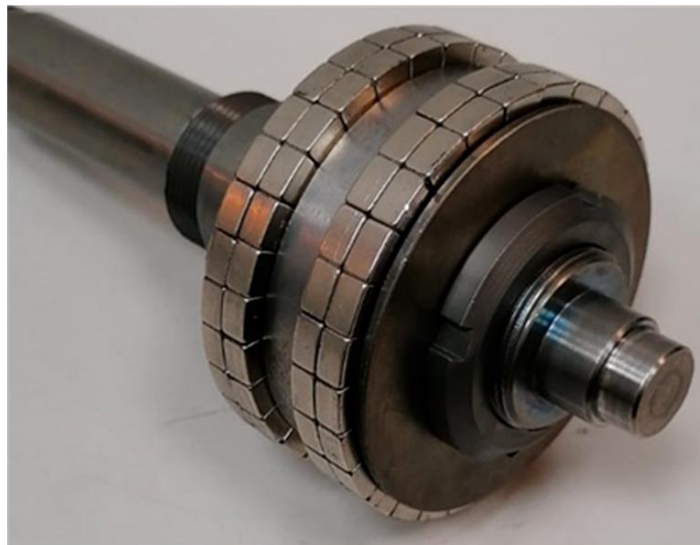


Figure 2.1 – Photo of the sun rotor with the first and second gear PMs mounted.

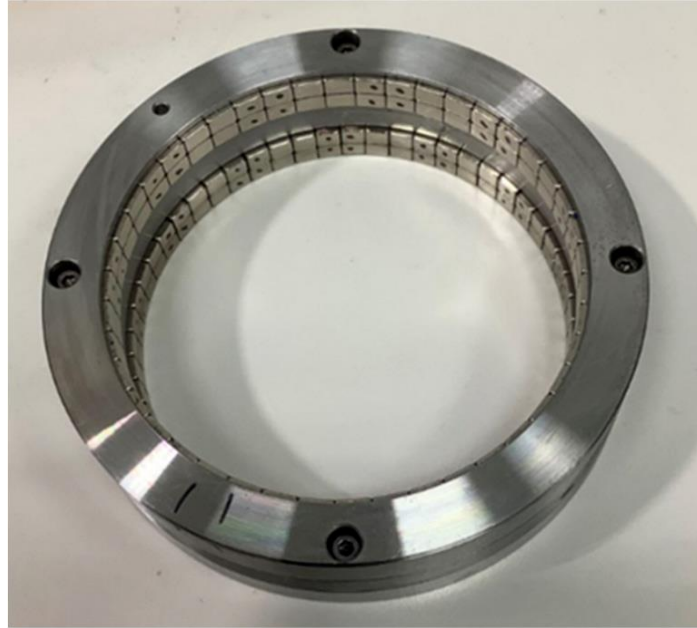


Figure 2.2 – Photo of the ring rotor with the first and second gear PMs mounted.



Figure 2.3 – Photo of the carrier with the ferromagnetic pole-pieces inside the resin structure and with winding attached for magnetic flux evaluation.

To select the wanted gear, the carrier needs to be in line with the corresponding rotors, so that it can convert the magnetic flux. The gear shift is performed by horizontally moving the carrier up to the next gear. A set of mechanical gears and screws enables the control of this operation to be held from the user.

The permanent magnets are partially mounted inside the material of the respective support iron yokes (the sun yoke is internal to the sun PMs, the ring yoke is external to the ring PMs) as shown in Figure 2.4 because studies have shown that, giving the high torques to which the outer rotor is especially subject, a surface configuration would generate great mechanical suffering to the structure, reducing that advantage peculiar to magnetic gears to alleviate damage [26]. Not only the

PMs need to be soundly mounted inside the yokes, but the ferromagnetic pole pieces too need to be secured, otherwise either a magnet or (not in this case since the carrier is static) a pole piece could move out of its place and cause damage [27]. It is still important to say that this type of configuration can slightly reduce the performance of the PMG compared to a surface mounted PMs configuration [28].

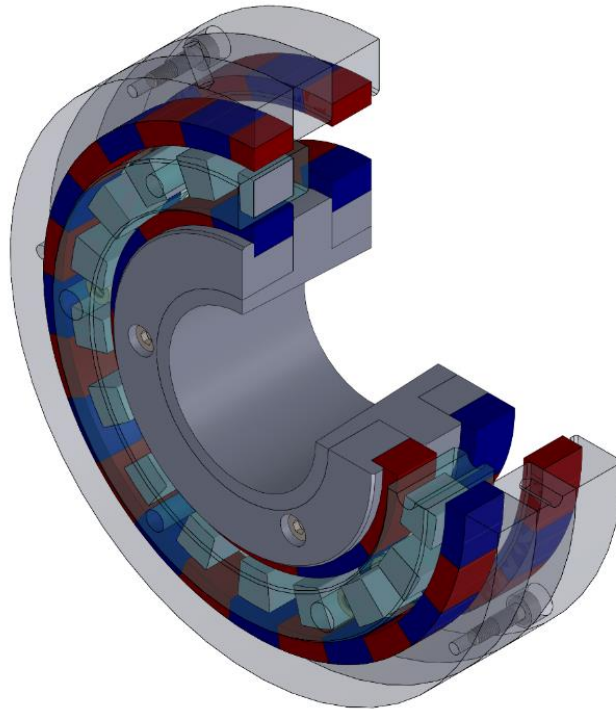


Figure 2.4 – 3D section view for the CAD project of the definitive PMG prototype showing the PMs that are partially mounted inside the iron yokes.

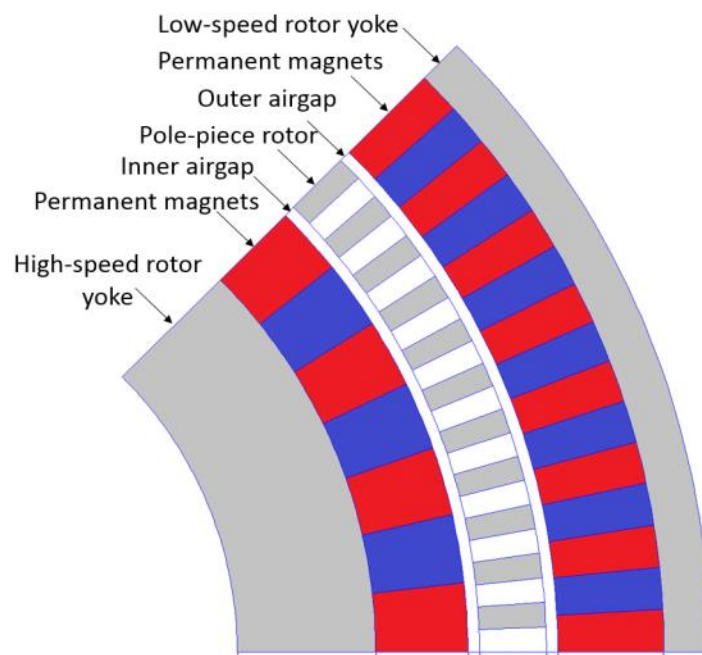


Figure 2.5 – Zoom on the schematic structure and key geometric elements for a planetary magnetic gear.

A 2D view of the gearbox is presented in Figure 2.6. The first gear is highlighted in tones of green (lighter for sun, darker for ring), the second gear in tones of blue, the movable carrier in yellow and the rolling bearings in red.

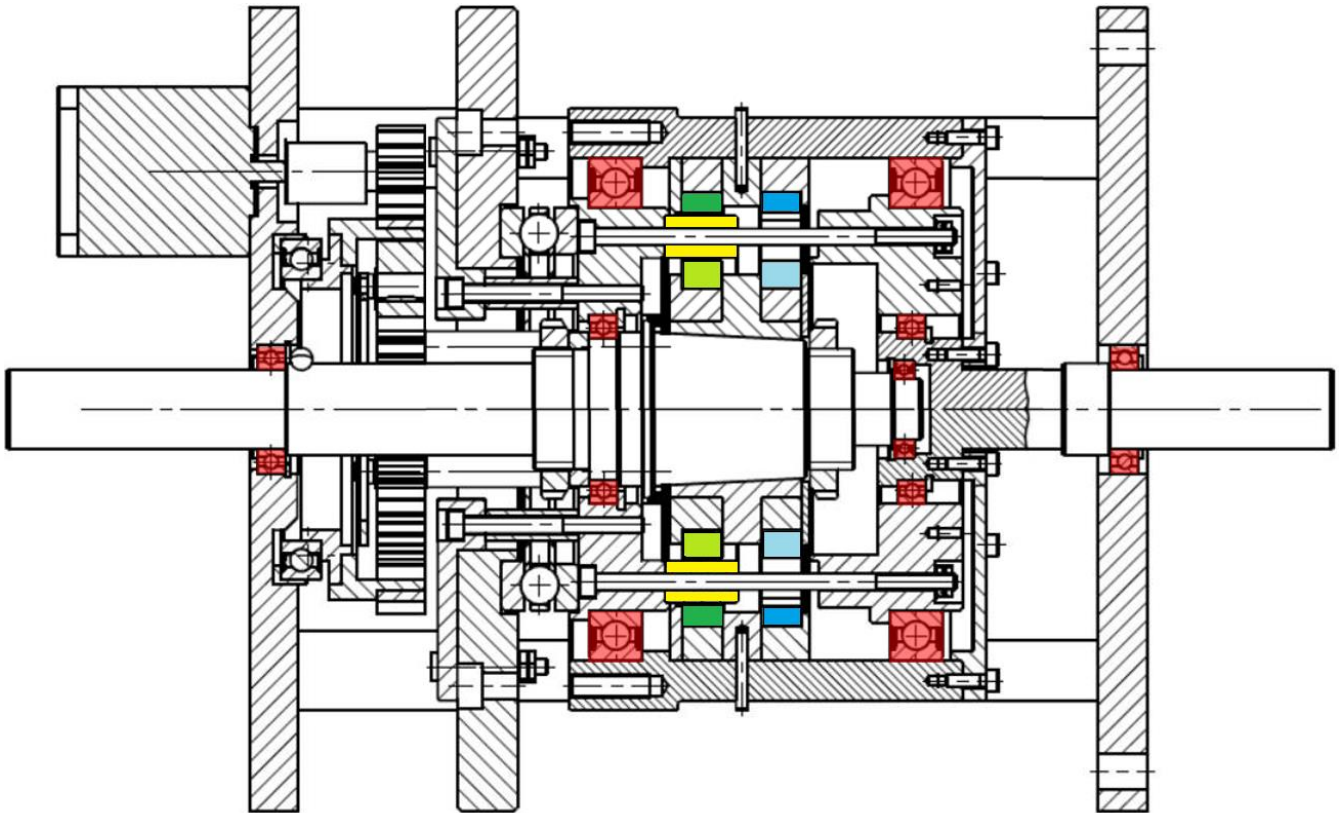


Figure 2.6 – 2D section view of the magnetic gearbox tested with active magnetic components and bearing highlighted.

Whit regards to dimensions, the values are shown in Table 2.1, derived from [29].

Table 2.1 – Physical dimensions of the PMG prototype.

Parameter	Value	Unit
Sun PM thickness	6.75	mm
Ring PM thickness	5	mm
Steel poles thickness	8.25	mm
Sun yoke thickness	6	mm
Ring yoke thickness	8.5	mm
Air gap	2	mm
Gear external radius	62.5	mm
Gear axial length	10	mm
Sun PM pole pairs, first gear	5	-
Ring PM pole pairs, first gear	13	-
Sun PM pole pairs, second gear	7	-
Ring PM pole pairs, second gear	11	-
Carrier pole pieces	18	-
First gear transmission ratio	2.6	-
Second gear transmission ratio	1.57	-
Sun torque, first gear	2.57	Nm
Sun torque, second gear	3.46	Nm

Focusing on the motion patterns, the magnetic gear is able to rotate thanks to the rolling bearings, whose ubication and sequence is presented in (Figure 2.7).

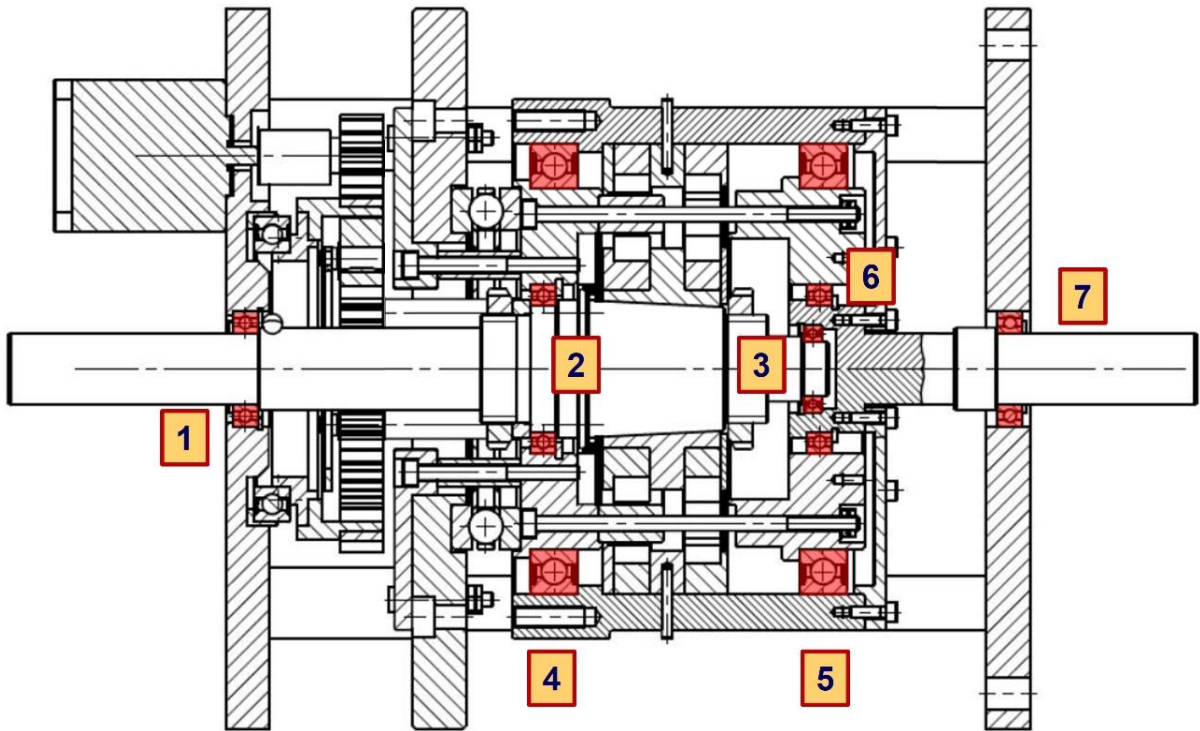


Figure 2.7 – 2D section view of the magnetic gearbox with the bearings highlighted and numbered for identification.

In Table 2.2 the bearings denominations are presented.

Table 2.2 – bearings denominations.

Number	Denomination
1	W 61804-2Z
2	W 61807-2Z
3	W 61802-2Z
4	61820-2RZ
5	61820-2RZ
6	W 61807-2Z
7	W 61804-2Z

So, bearings 1 and 7, 2 and 5, 4 and 5 are, respectively, the same kind. This choice is due to balance needs during rotation. Originally, there was a different set of bearings installed in the gearbox. It was replaced with the current set because the losses registered were higher than expected. The new bearings need to show if any improvement happened.

It is also possible to see that there is an extra axial bearing that is not highlighted. The prototype of magnetic gearbox tested in this work was constructed with the idea of being able to function both with the carrier fixed (the case studied) and with the ring fixed. This bearing would be activated in this last mode of operation; therefore, it is not relevant in our case.

2.2 Test rig components

The magnetic gear is but a component of the whole test rig. The rig itself then communicates with an electrical panel, and both are placed in the mechanical department lab as shown in Figure 2.8.



Figure 2.8 – test rig and electrical panel next to it.

The electrical panel represented works for both controlling and supplying electrical power to the brushless motors and for the acquisition sensors on the test bench. Five different voltage levels are used, namely:

- 400 V (AC): to supply the rectifier;
- 540 V (DC): to supply the inverter;
- 230 V (AC): to supply the converters 230 V (AC) / 24 V (DC) or
- 230 V (AC) / 5 V (DC);
- 24 V (DC): to supply motor stepper for gearshift, torque sensors, acquisition system (Compact Rio), the auxiliaries of inverter and its heatsink;
- 5 V (DC): to supply incremental magnetic encoders.

The gearbox (Figure 2.9) is linked to other parts, both with functional and structural roles.

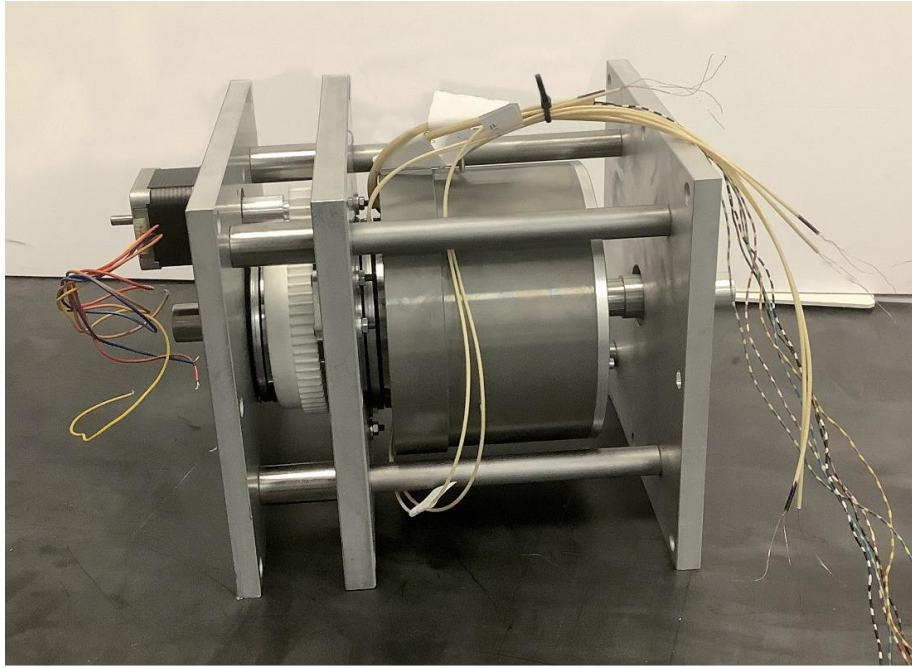


Figure 2.9 – external appearance of the PMG prototype used.

The gear, being of functional importance, is connected by two shafts to the two featured electric motors. On the shafts, two incremental magnetic encoders are placed in order to collect speed data, two torque sensors detect torque values and an oscilloscope connected directly to the magnetic gear evaluates the magnetic flux inside the gear, both the radial and circumferential components (Figure 2.10).



Figure 2.10 – focus on the active part of the test bench while magnetic fluxes are being sampled with an oscilloscope.

2.2.3 Frame

This is the structural element that keeps other elements steady and is design in a way in which the single elements can be extracted with minimum intervention. This structure is made of metal profiles [30].

Table 2.3 – Test bench frame elements and dimensions.

Dimension	Value	Unit
Profile height	40	mm
Profile width	80	mm
Structure height	1	m
Structure width	0.4	m
Structure length	1.3	m

2.2.4 Motors

The test bench is equipped with two DC brushless electric motors which are the same model with the same parameters, provided by Servotecnica [30].



Figure 2.11 – Brushless DC motors, model SVTM A by Servotecnica.

They present an IC 400 construction and an IP65 protection certification. The parameters are presented in Table 2.4.

Table 2.4 – Brushless DC motors, model SVTM A, and parameters associated.

Parameter	Value	Unit
Frame diameter	115	mm
Motor length	218	mm
Continuous stall torque	11.5	Nm
Nominal torque	9.3	Nm
Nominal speed	2800	rpm
Nominal power	5	kW
Peak torque	30	Nm
Mass	9.5	kg

2.2.5 Torque transducers

The two shafts have one torque transducer each to detect the loads on each side. The two transducers are chosen with different nominal torques since the two sides work under different conditions (the sun side has lower torques involved than the ring side) and then may reach overload at different values. Apart from this calibration, they are the same kind of transducer: the T21WN produced by HBM (Figure 2.12) [30].



Figure 2.12 – Torque transducer, HBM T21WM series.

And the parameters of importance are reported in Table 2.5.

Table 2.5 – Torque transducer HBM T21WM parameters.

Parameter	Value	Unit
Power supply	10 - 28.8	V _{DC}
Nominal torque sun	5	Nm
Nominal torque ring	10	Nm
Nominal speed	19000	rpm
Frequency output	5 - 15	kHz
Voltage output	-10 - 10	V
Frequency resolution	0.19	Hz
Voltage source	24	V
Deviation from linearity	< 0.1	%
Output frequency for T=0	10	kHz

2.2.6 Incremental encoders

Two incremental encoders are mounted on the two shafts for the detection of angular speed. They both are the same LM10IC05 model produced by RLS presented in Figure 2.13 [30].

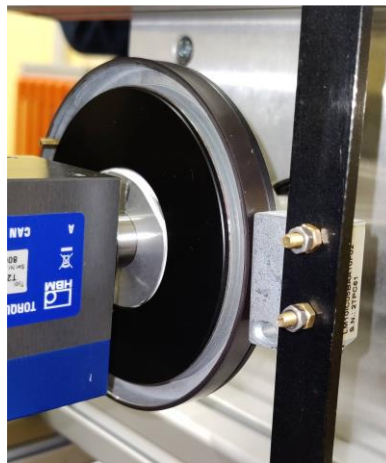


Figure 2.13 – Incremental encoder RLS LM10IC05 mounted on the test rig.

The parameters are once again reported in Table 2.6.

Table 2.6 – Incremental encoder RLS LM10IC05 and its parameters

Parameter	Value	Unit
Power supply	4.7 - 7	V _{DC}
Response time	< 10	μs
Switching time (10 to 90%)	< 30	ns
Output signals	3 square-wave signals and their inverted signals	-
Reference signals	1 or more square-wave pulse signal and its inverted pulse	-

2.3 LabView software

The functioning of the test bench is made possible only by controlling the two electric motors, whose rotation generates a certain mechanical power which is then transmitted to the opposite side. The control of the motors can be implemented by either controlling the speed or the torque. Controlling the speed means using a motor as a generator, since it will strive to maintain that speed no matter the value of the resistant torque. On the other hand, the motor controlled in torque is working as a user that gives a certain amount of resistance to motion. The eventual torque control of a motor that doesn't serve this purpose, like in the case of a generator without a resistant load on the other side, can make the system lose equilibrium and indefinitely increase the speed once the internal resistances of the structure are overcome. This scenario is to be thoroughly avoided to not damage any component.

Both these behaviours can be regulated by means of a software.

The software used in this occasion is LabView by NI. LabView is a platform that, through a visual programming language, allows to create a digital counterpart to real world scenarios. It uses elements called virtual instruments (VI) that can contain many different operations and process different types of data (numerical, boolean, string and others). In creating and properly connecting VIs, both a front panel (Figure 2.14) and a block diagram (Figure 2.15) are formed. In the former the programmer can interface during the operational phase inputting the needed data and receiving the outputs directly on the screen, while the latter is mostly reserved for the programming phase prior to the functioning, for the creation of the right structures and conditions.

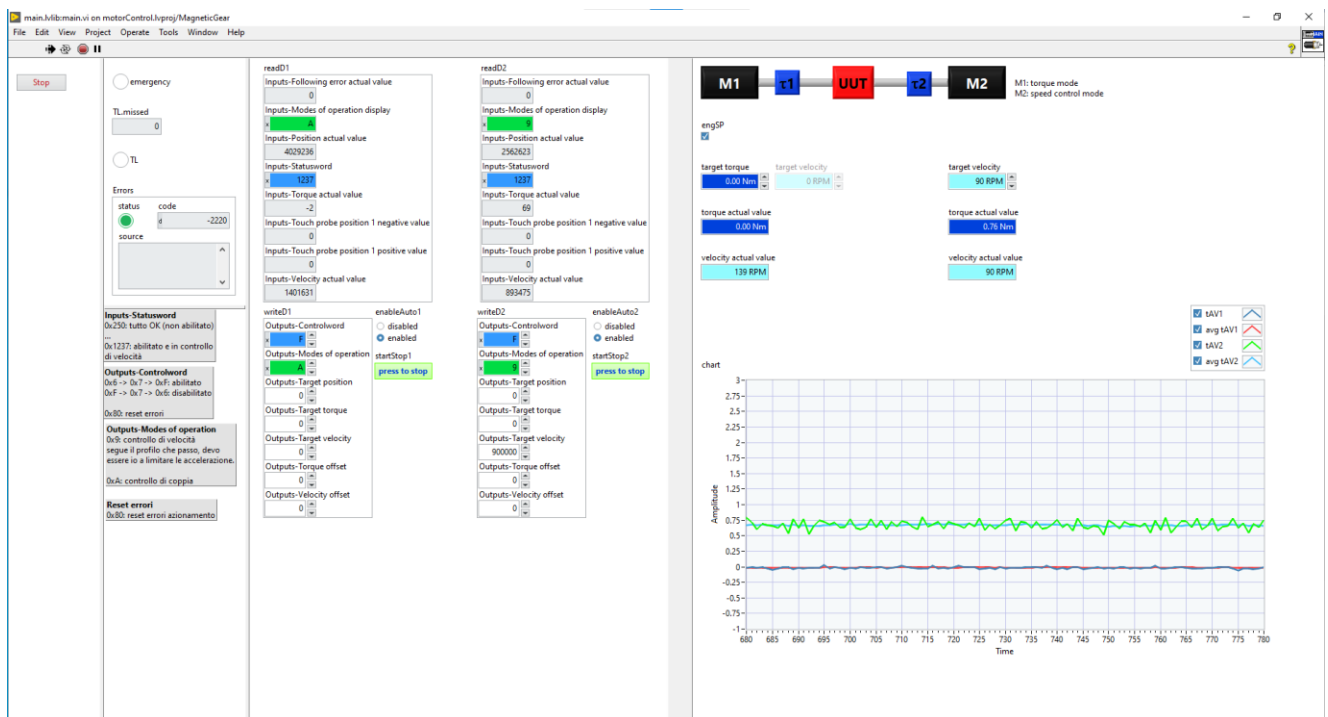


Figure 2.14 – front panel of the project with the speed and torque inputs and outputs.

In this case, in the front the speed and the torque of the sun and ring motor can be chosen. The choice of which between speed and torque is going to be inputted on a certain branch must be done previous to the opening of the file, editing a boolean parameter. The choice has to be reversed for the other branch to replicate real world conditions.

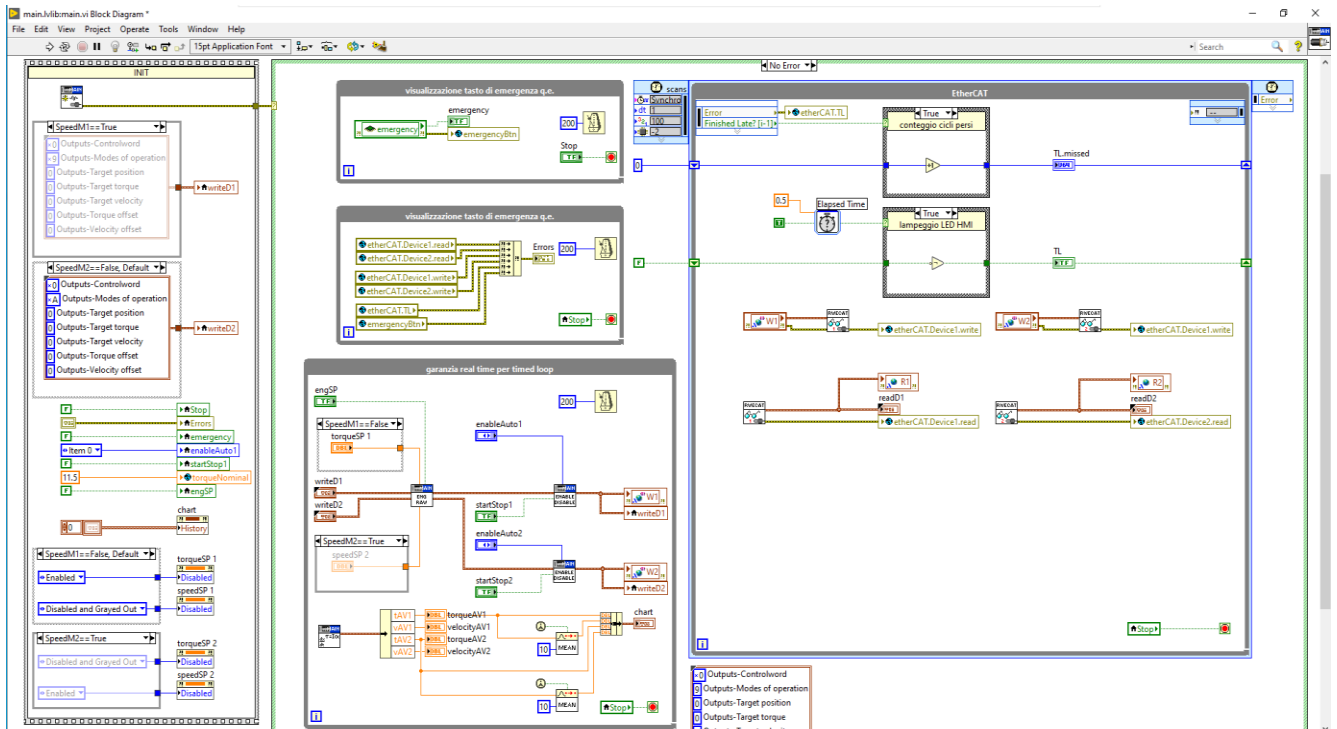


Figure 2.15 – block diagram of the project that commands the test bench.

In the block diagram it is possible to follow step by step the flow of commands in the order that the software follows by clicking on the light bulb icon, in case the program doesn't work as wanted. The acquisitions from the test bench are instead derived from another file just to separate the input block from the output block for the sake of clarity (Figure 2.16). In this file, the speed and the torque are sampled in a fixed chosen range of 5 seconds, and the sampling frequency can be chosen on the top left corner as shown. The minimum limit of speed at which the program acquires is 60 rpm, under that it just self-stops. A higher frequency gives more detail but gives also heavier samples and, for the tests in which the mean value only is required, it doesn't make a difference.

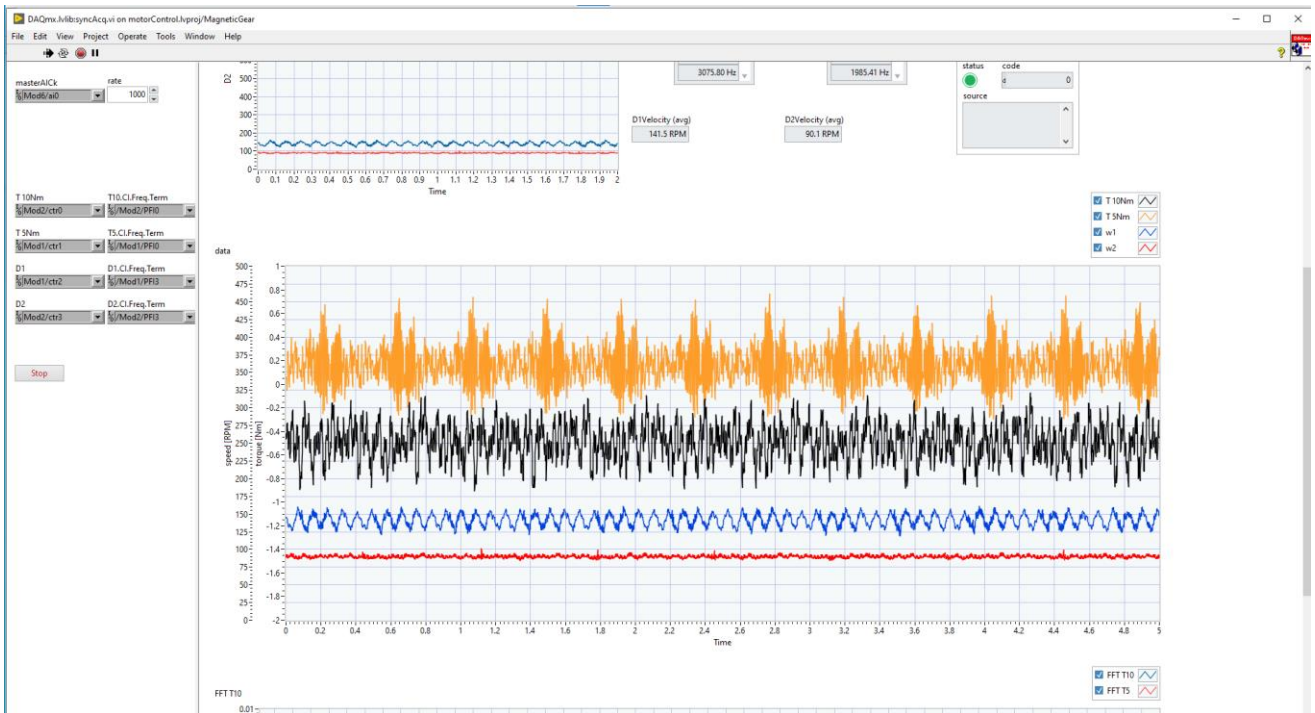


Figure 2.16 – front panel of the project with speed and torque outputs.

This file gives an important first feedback of what the processed data will look like if the system encounters some sort of resonance or if the sensors have imprecisions sampling and register false sudden spikes that, if not treated properly, could compromise the validity of the results..

Chapter 3

3. Experimental tests

3.1 Design of Experiments (Doe)

The most important aspect that needs to be analysed in detail is the behaviour of the test bench when subject to different functioning conditions. What this means is the analysis of the performance in terms of overall efficiency and its contributions: since there is a mechanical structure that couples with magnetic parts, there are two separate factors that need to be addressed properly.

Furthermore, since the gear previously featured a different set of bearings that were changed before the beginning of these tests, a comparison between previous and current data is needed to establish if there has been an improvement.

The tests have been divided based on various elements. A design of experiments (Doe) has been initially developed for a better organization and consists in the following steps.

First of all, a set of tests without any load has been carried out, since the available data from the previous bearings were taken in this way. In this scenario, the electric motor that is not used during a specific test is completely detached from the transmission through the linking joint.

This step has been articulated in four cases, as depicted in Figure 3.1 in the order in which the lab tests were conducted.

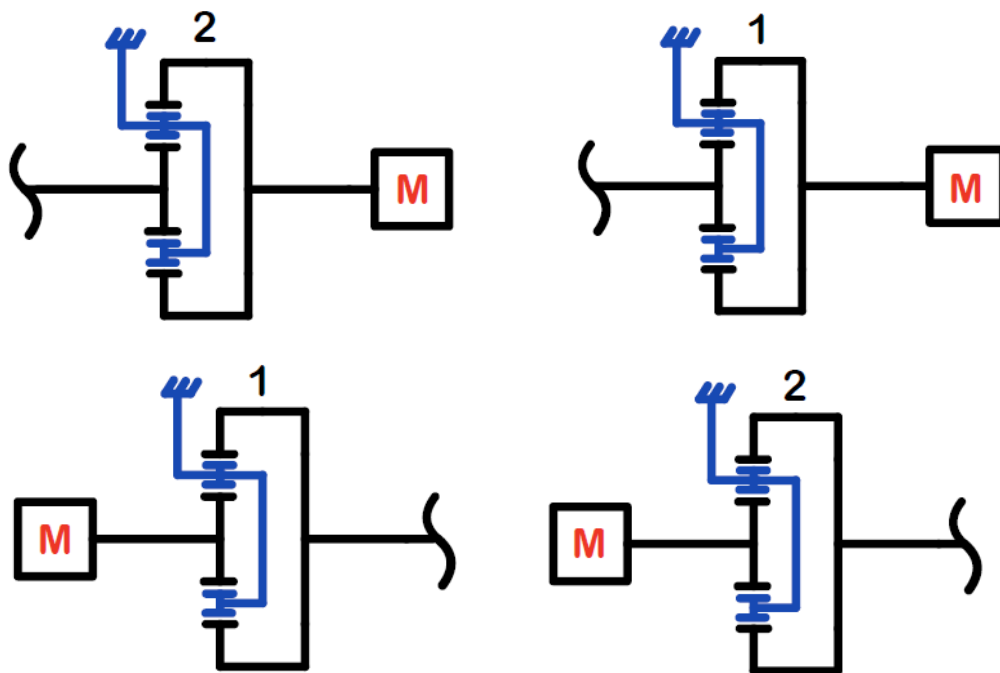


Figure 3.1 – Operational schemes for the no-load tests with the engaged gear reported over the schemes.

In these simple schemes the basic active components are featured. The motors are represented by a squared block, the shaft by straight lines, the magnetic gear by the equivalent scheme of a planetary gear with the ferromagnetic carrier highlighted in blue, being the static element, depicted as constrained to the structure.

The electric motor that is working as a generator is marked with a red M while on the free edge there is a curved line, and the selected gear is represented by a number over the magnetic gear scheme.

The four conditions are articulated in twelve speed cases each, and the specifics are reported in Table 3.1.

Table 3.1 – Input speeds on the active side for no-load tests.

First gear speed multiplier	First gear speed reducer	Second gear speed multiplier	Second gear speed reducer
Input speed (rpm)	Input speed (rpm)	Input speed (rpm)	Input speed (rpm)
60	156	60	94
120	312	120	189
180	468	180	283
240	624	240	377
300	780	300	471
360	936	360	566
420	1092	420	660
480	1248	480	754
540	1404	540	849
600	1560	600	943
660	1716	660	1037
720	1872	720	1131

The principle for these numbers is that the fixed reference is always the speed at the second gear going from 60 to 720 rpm with steps of 60 rpm. Speeds on the sun side are then obtained by multiplying these numbers by the current transmission gear ratio.

Here comes the first limitation during the acquisitions: the program only allows for integer numbers to be digitized. The second gear however results in a conversion that gives decimal numbers, not giving an exact reproduction of real conditions. The solution is to round the decimal to the nearest integer number.

After this first set come the loaded tests, in which both electric motors are connected, one being a generator and the other being a user.

In Figure 3.2 the combinations are reported.

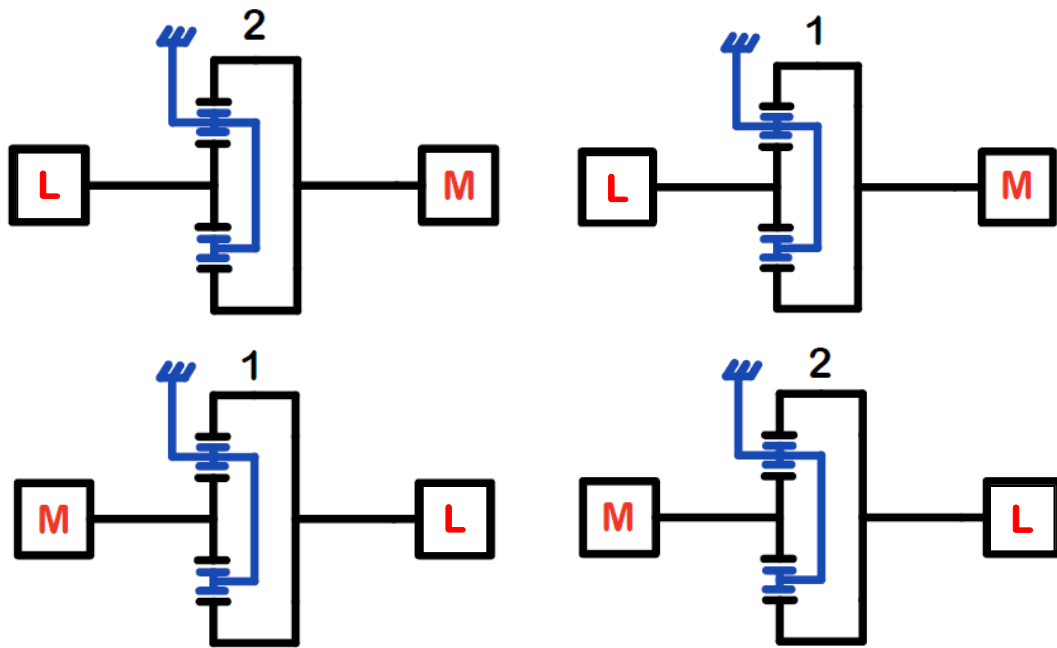


Figure 3.2 – operational schemes for the loaded tests with the engaged gear reported over the schemes.

The basic active components are featured as in the previous figure.

The electric motor that is working as a generator is marked with a red M and the one working as a user is empty.

In this case, for each working condition not only there are twelve different speeds, but also four resistant torque scenarios, amounting to a total of 192 possible combinations. Although in Table 3.2, Table 3.3, Table 3.4 and Table 3.5 all of them are presented, during the tests it will be shown that in some cases the limit conditions are reached before completing the full series. Here the full program is shown because it is how the DoE has been conceived.

The principle here is the same as before for the speeds. The novelty is the choice of torques; there still is a reference that is the torques on the sun side with the second gear on, the reason being that this is the first tested condition. The conventional values adopted are 0.5 Nm, 0.75 Nm, 1 Nm and 1.15 Nm. The detailed conversion logics will be explained in the dedicated chapters.

Table 3.2 – Ring input, second gear case.

Input speeds (rpm)	First torque (Nm)	Second torque (Nm)	Third torque (Nm)	Fourth torque (Nm)
60	0.5	0.75	1	1.15
120				
180				
240				
300				
360				
420				
480				
540				
600				
660				
720				

Table 3.3 – Ring input, first gear case.

Input speeds (rpm)	First torque (Nm)	Second torque (Nm)	Third torque (Nm)	Fourth torque (Nm)
60	0.3	0.45	0.6	0.75
120				
180				
240				
300				
360				
420				
480				
540				
600				
660				
720				

Table 3.4 – Sun input, first gear case.

Input speeds (rpm)	First torque (Nm)	Second torque (Nm)	Third torque (Nm)	Fourth torque (Nm)
156	0.78	1.17	1.57	1.96
312				
468				
624				
780				
936				
1092				
1248				
1404				
1560				
1716				
1872				

Table 3.5 – Sun input, second gear case.

Input speeds (rpm)	First torque (Nm)	Second torque (Nm)	Third torque (Nm)	Fourth torque (Nm)
94	0.78	1.17	1.57	1.96
189				
283				
377				
471				
566				
660				
754				
849				
943				
1037				
1131				

Eventually, a set of experiments with the magnetic gear in neutral position has been carried out. The geometry of the gear allows for the moving carrier to stop at an intermediate position and not be connected to either gears. The result is the detachment of the power generating branch from the user branch. With this technique it has been possible to simultaneously run the two branches of the test bench in an independent way (Figure 3.3).

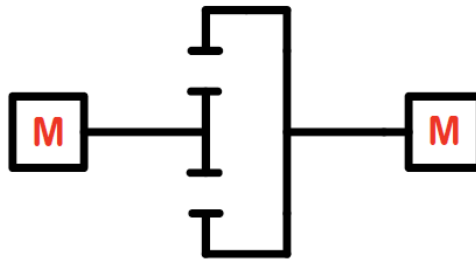


Figure 3.3 – Operational scheme for the neutral tests.

In this case, the initial DoE consists of a 11x11 grid of input speeds (11 for the sun and 11 for the ring) ranging from 60 to 360 rpm with a step of 30 rpm. However, this has needed an update since the values obtained from it have been considered not suitable; the updated DoE features a 15x12 grid that extends to the max values of speed for both the sun and the ring. The two grids are shown in Table 3.6, and Table 3.7.

Table 3.6 – 11x11 grid speed combinations, neutral operation.

		Ring speed n_2 (rpm)										
		60	90	120	150	180	210	240	270	300	330	360
Sun speed n_1 (rpm)	60											
	90											
	120											
	150											
	180											
	210											
	240											
	270											
	300											
	330											
	360											

Table 3.7 – 15x12 grid speed combinations, neutral operation.

		Ring speed n₂ (rpm)											
		60	120	180	240	300	360	420	480	540	600	660	720
Sun speed n₁ (rpm)	60												
	90												
	120												
	156												
	312												
	468												
	624												
	780												
	936												
	1092												
	1248												
	1404												
	1560												
	1716												
	1872												

3.2 Engaged gearbox operation

In this section, the engaged operation of the PMG is examined, and a detailed post processing is going to be executed, starting from the acquired lab data on the magnetic gear test bench.

The goal of the lab activity is to gather different sets of values in order to have a full understanding of the mechanical behaviour of the test bench. Once the acquisition phase is over, the post processing takes place so that a quantitative analysis can be implemented.

The magnetic gearbox has the capability to work in four different ways: as a reducer, as a multiplier and in 1st and 2nd gear. A view of the internal structure in 1st and 2nd gear from the CAD project is presented in Figure 3.4.

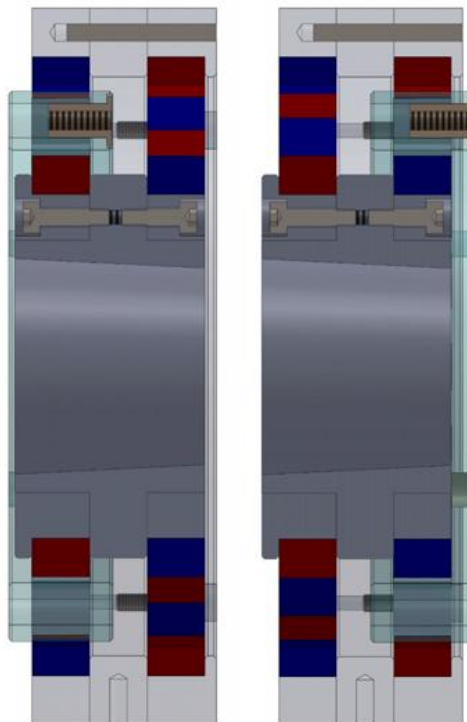


Figure 3.4 – Internal position of the carrier for 1st (left) and 2nd gear (right).

The post processing steps are conceptually identical for each of the four conditions; the variations are due to different conversions and are going to be detailed.

3.2.1 No-load tests

For the no-load tests, the downstream DC motor gives no resistance to the imposed motion because it gets detached by disconnecting the joint flange associated with it. This motor is then totally deactivated.

3.2.1.1 Acquisitions

As stated in §1.7, the tests are conducted referencing to the ring speed. When the ring is actually the generator, the speeds go from 60 rpm to 720 rpm with a step of 60 rpm. When the sun is the

generator, the numbers differ simply by a gear ratio coefficient: for the first gear, the ring numbers are all multiplied by the first gear ratio (13/5), for the second gear by the second gear ratio (11/7). This process is not implemented only once; it always involves cycles of speed increase and speed decrease by the same amounts and with the same extremes. The purpose is the evaluation of the hysteresis of the system, known to occur because of the previous tests with the old bearings. Due to acquisition limits, the samples do not have the same length: the ones at 60 RPM are at 1 kHz of sample frequency, the ones at 120 and 180 RPM are sampled at 2 kHz and the remaining ones are at 4 kHz. These sampling rates are sufficient for a detailed result. The total sample time for each test is 5 seconds.

3.2.1.2 Signals filtering

The data gathered at this point has some flaws that can already be noticed in the LabView graph: the digital encoders wrongly register sudden spikes in the speed trace, especially for the ring speed. These need to be filtered in order to reduce the noises and be able to better process the data; this was accomplished by developing a custom filter which cancels slopes on the signal that are over a given value, and the slopes filtered are customized to each point. Then, the load samples need to be filtered, too; in this case the digital filter was used, and the limit cutting frequency was chosen based on the frequency of acquisition in a proportional way in case the increased rate captured more details. The graphs for the speed filtering are presented in Figure 3.5 and Figure 3.6. The case taken into consideration is the second gear multiplier case, therefore with the ring being the input and the side where the torque is registered.

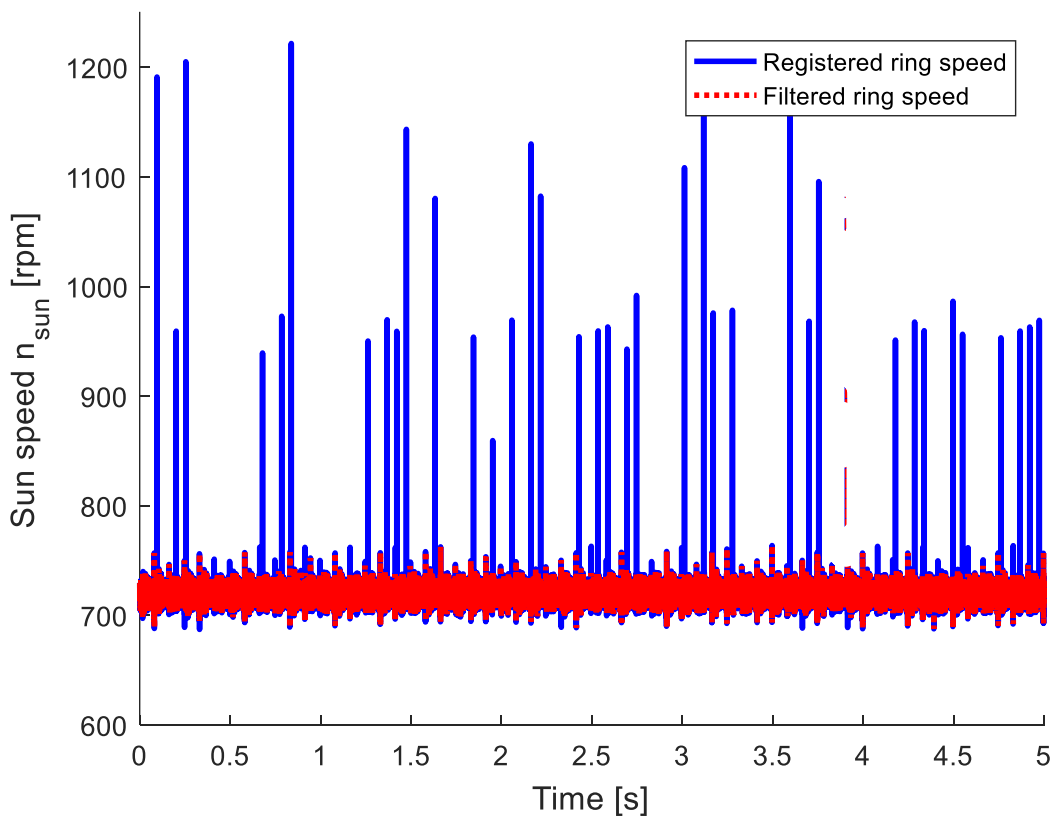


Figure 3.5 – Ring speed before and after the filtering using the custom filter.

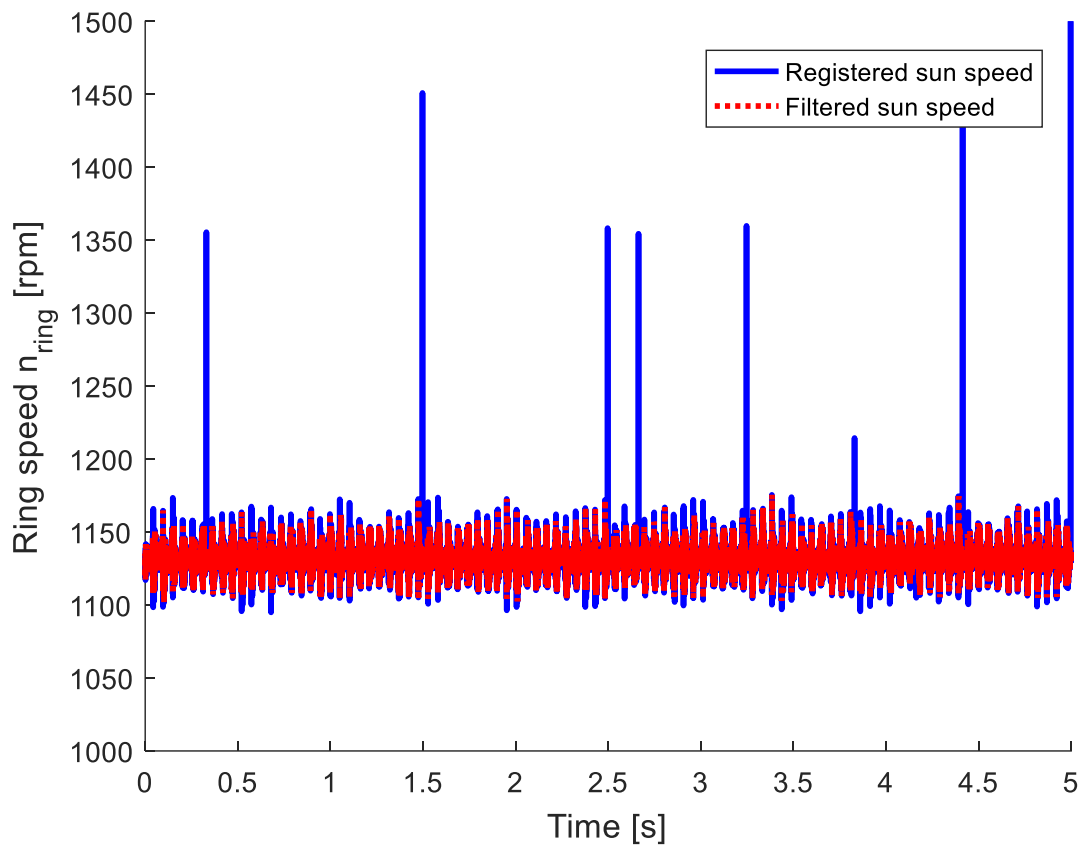


Figure 3.6 – Sun speed before and after the filtering using the custom filter.

It is possible to see how the prominent spikes, that are particularly abundant for values above the mean value, get dissipated in a significant way.

Then, in Figure 3.7 the graph for the torque filtering is shown.

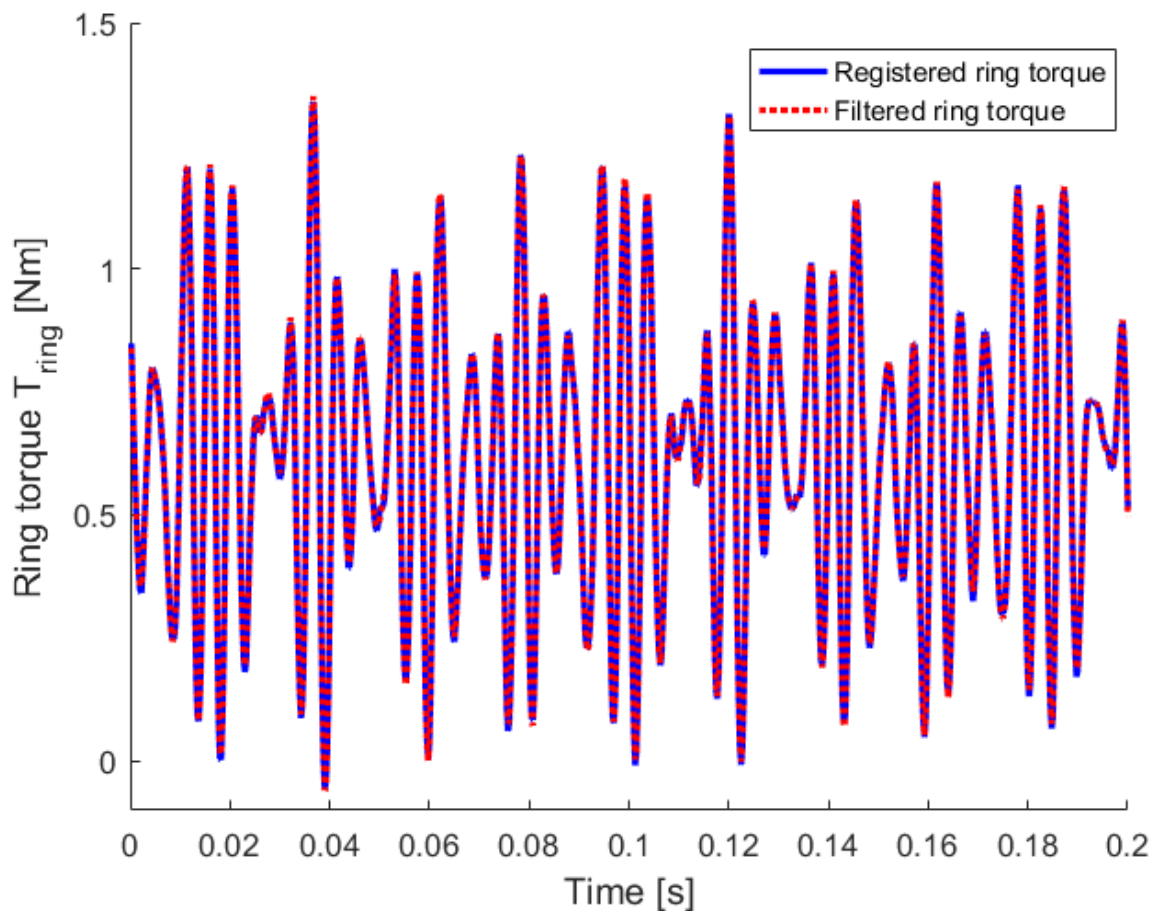


Figure 3.7 – Ring torque before and after the filtering using the digital filter.

In this case the graph presented is zoomed on a small fraction of the 5 total seconds for the sake of clarity; in fact, the improvement is difficult to notice by eye, and is mostly relegated to the points of relative maximum and relative minimum as a smoothing of the edges.

The digital filter that applies to the torque cuts off the frequency contents that are present in the chosen range of frequencies, going from 0.5 Hz up to infinity.

3.2.1.3 Torque loss

In this scenario, the whole torque provided by the DC motor gets dissipated without supplying the user. Therefore, once the values of input torque are registered on the input shaft torque sensor, the torque dissipation values are immediately obtained.

The magnetic gear previously featured a different set of bearings which absorbed too high a value of torque in the no-load case due to internal frictions. Therefore, they have been substituted with a new set. The comparison between then and now takes place as the graph shows in Figure 3.8. The old values are obtained with the PMG working as a speed multiplier at 1st gear, therefore the graph besides it in the figure is the analogous graph in the same conditions; the other graphs then are not to be compared as strictly but analysed nevertheless, and are presented in Figure 3.9, Figure 3.10 and Figure 3.11. All the values are referred to the ring speed .

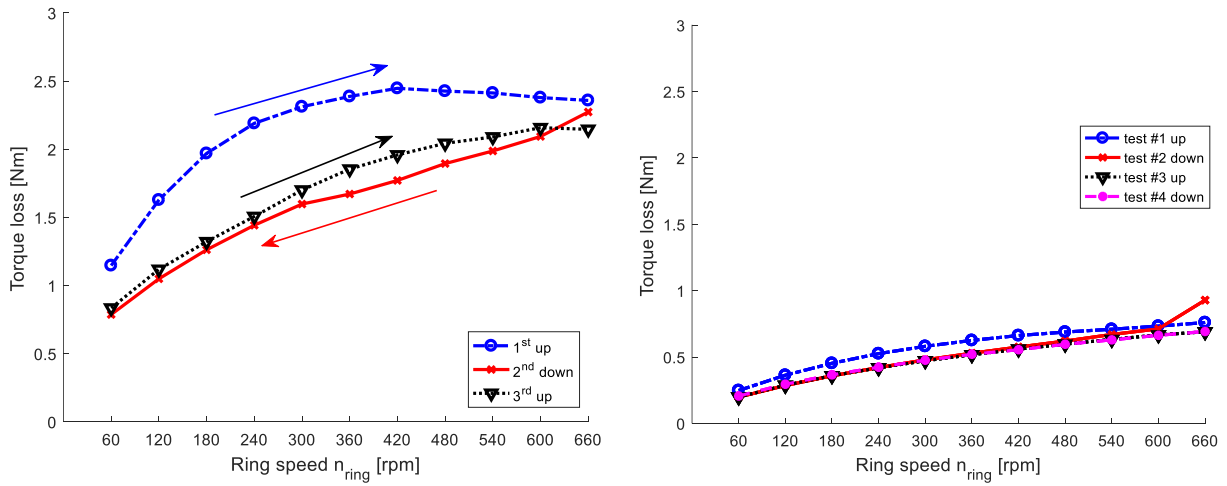


Figure 3.8 – Torque loss values and tendency lines with the old (left) and new bearings (right), 1st gear speed multiplier.

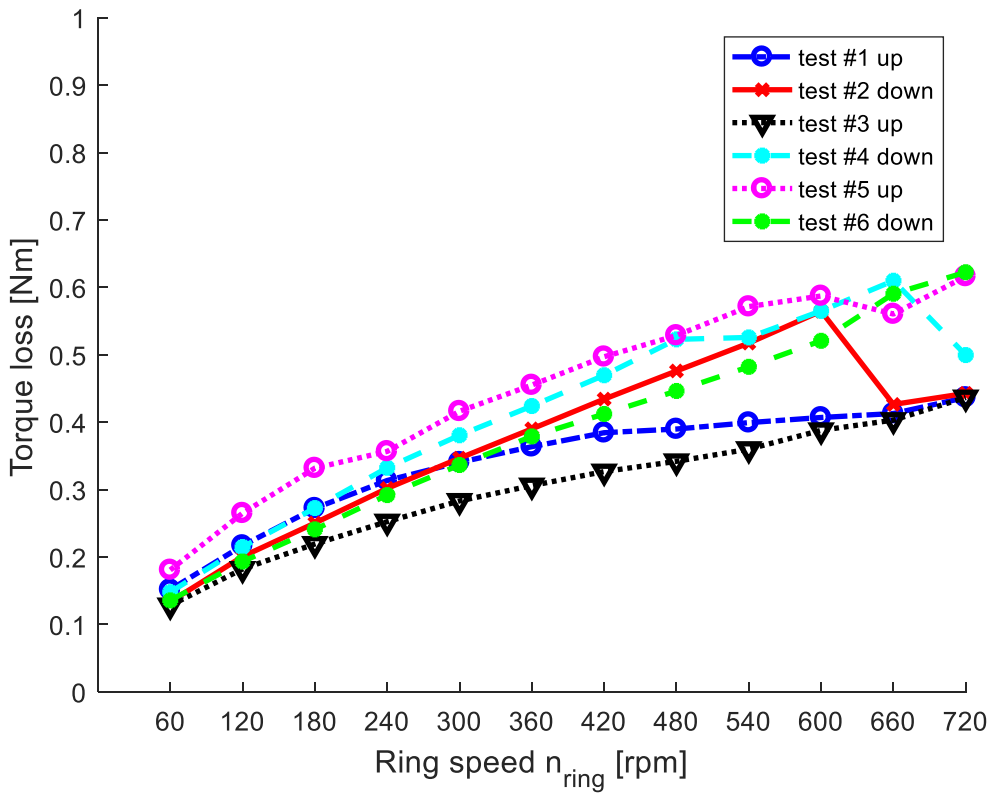


Figure 3.9 – Torque loss values and tendency lines with the new bearings, 2nd gear speed multiplier.

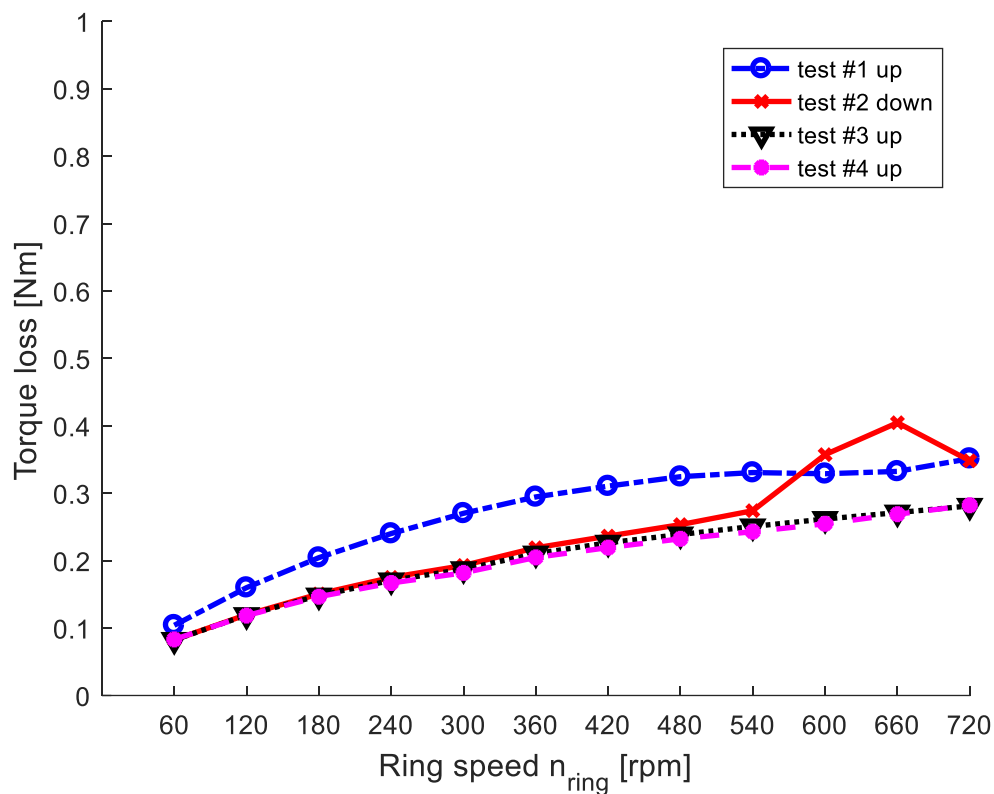


Figure 3.10 – Torque loss values and tendency lines with the new bearings, 1st gear speed reducer.

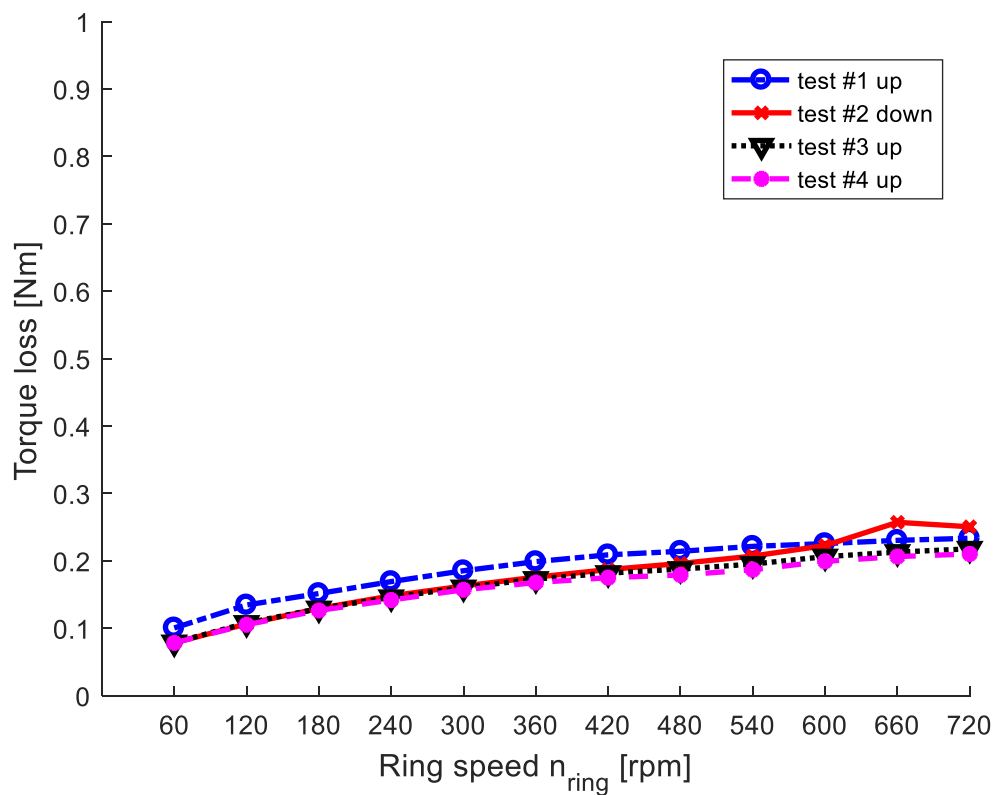


Figure 3.11 – Torque loss values and tendency lines with the new bearings, 2nd gear speed reducer.

The torque loss increases with speed, and therefore the power loss increases as well, as also stated in [31] through a numerical simulation using finite elements.

There is a decrease of about 70% in torque loss on equal terms, so the change has produced a positive effect.

However, there is also another phenomenon occurring at high speeds, noticeable in all the new graphs: once the highest rotation speeds are reached with the new bearings during the first ascent, there is a sudden increase in torque loss in the beginning of the first descent that maintains itself for a couple of speed stamps before going back to the main trend. For this reason, compared to the three paths of the old tests, now at least four successions are registered. For the first chronological test (the second gear multiplier), since this was a new phenomenon, six successions were made to further analyse it. Here however, the rise doesn't go back to normal and continues with a different rate of decline.

It is possible that this is caused by the protracted stop at the top speed that is needed for sampling reasons, since it needs to be registered two times and the processing time for the data is about 30 second, and this is the only difference in the PMG functioning compared to other speed stages.

The hysteresis is maintained in the new cases although with the new bearings it is much more limited. Since it was overheating in the bearings and for eddy currents that caused it in the old scenario [32], now it makes sense that with the new bearings that cause sensibly less heating in the structure this occurrence is witnessed.

3.2.2 Loaded tests

With regards to the loaded tests, the resistant load has been applied to the exit axis, opposed to the motion given by the motor.

3.2.2.1 Acquisitions

Depending on the operation mode requested, different torques are applied as shown in the tables of §1.7.

The parameters are still set based on the values in the second ring multiplier case. This involves going from an angular speed of 60 rpm up to 720 rpm, with a fixed step of 60 rpm, just as in the no-load scenario. However, now only one ascent is performed for each resistant load value.

Here, the load values at the sun side are 0.5 Nm, 0.75 Nm, 1 Nm and 1.15 Nm. The tests interrupted early since the PMG didn't bear the last load of 1.15 Nm when the speed of 180 rpm was exceeded. To get to the torques in the next condition, the first gear multiplier, the previous torques need to be transposed to the ring side by multiplying by the second gear ratio, and then adjusting it to the first gear by dividing by the first gear ratio. The results give the following torques: 0.3 Nm, 0.45 Nm, 0.6 Nm and 0.75 Nm. The last resistant load couldn't be applied at all because the system failed after 360 rpm with the 0.6 Nm load.

Then comes the first gear reduced mode, where to get the resistant ring torques it is enough to transpose the last torques to the ring side by multiplying by the first gear ratio, obtaining 0.78 Nm, 1.17 Nm, 1.57 Nm and 1.96 Nm. The input speeds are simply the reference ring speeds multiplied by the first gear ratio.

Eventually, there are the second gear reducer tests, where the torques are derived from the second gear multiplier scenario and transposed to the ring side, multiplying by the second gear ratio. The results are the same as the last case: 0.78 Nm, 1.17 Nm, 1.57 Nm and 1.96 Nm. The input speeds are the reference ring speeds multiplied by the second gear ratio. The tests stopped at 60 rpm with the 1.96 Nm load, after which functional failure occurred.

The samples are registered as in the no-load case: the ones at 60 rpm on the ring and the related sun transposition are at 1 kHz of sample frequency, the ones at 120 and 180 rpm on the ring and the related sun transposition are sampled at 2 kHz and the remaining ones are at 4 kHz. The total sample time for each test is 5 seconds.

3.2.2.2 Signals filtering

The same type of filtering used previously for the unloaded samples has been used for this set of data. In this case it is even more important to remove the noises because there is going to be a point by point analysis of every element sampled, too.

3.2.2.3 Efficiency of the magnetic gear

The global efficiency, η , is defined as follows in eq. (3.1):

$$\eta = \frac{T_{out}\omega_{out}}{T_{in}\omega_{in}} \quad (3.1)$$

Where the subscripts in and out respectively represent quantities on the input side and on the output side. T is the torque registered by the torque sensors and ω is the angular speed registered by the encoders.

It is sensible to expect the magnetic gear to have high levels of efficiency, given the fact that frictions are much smaller compared to the mechanical counterpart. For a detailed evaluation, the study is divided in two parts: a point-by-point analysis and a mean result.

In this phase, the global performance of the PMG is taken into account, considering the component as a black box in which only the power supply and the user are seen.

3.2.2.4 Internal efficiency

First, an internal evaluation has been carried out. In this case the singular experimental points for torque and speed have been picked and put into the formulation in eq. (3.1). This means that there is the same number of registrations for the torques and the speeds, and therefore the internal efficiency points are in the same number.

and the results show that the efficiency is overall higher when the speed is lower, declining steadily increasing the speed. This pattern is presented for the second gear speed multiplier operation in Figure 3.12, Figure 3.13, Figure 3.14 and Figure 3.15.

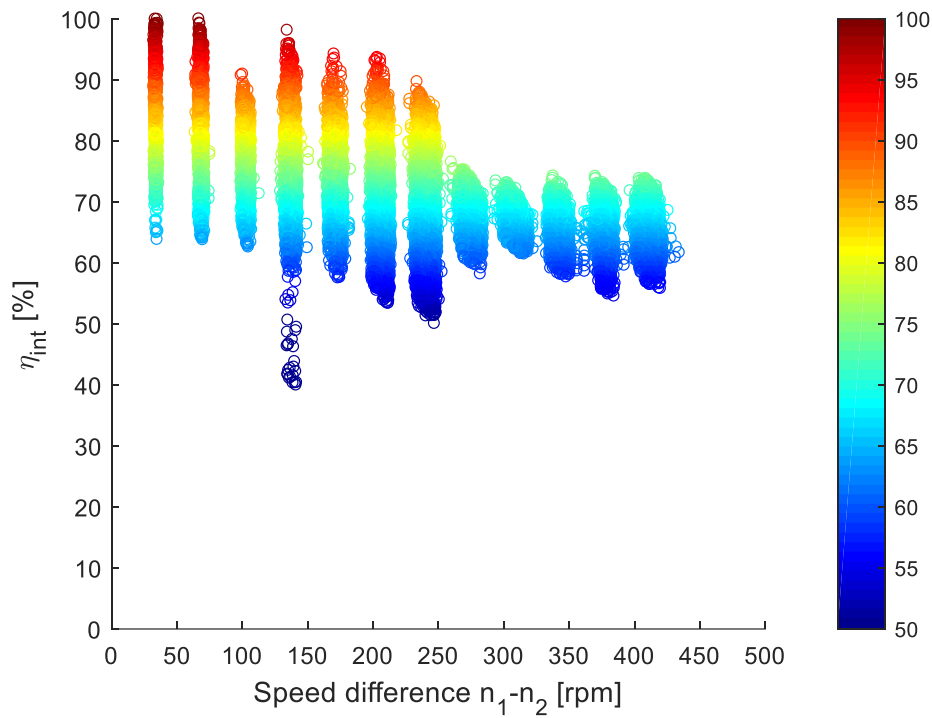


Figure 3.12 – Efficiency plot 2nd gear multiplier, $T_1=0.5$ Nm.

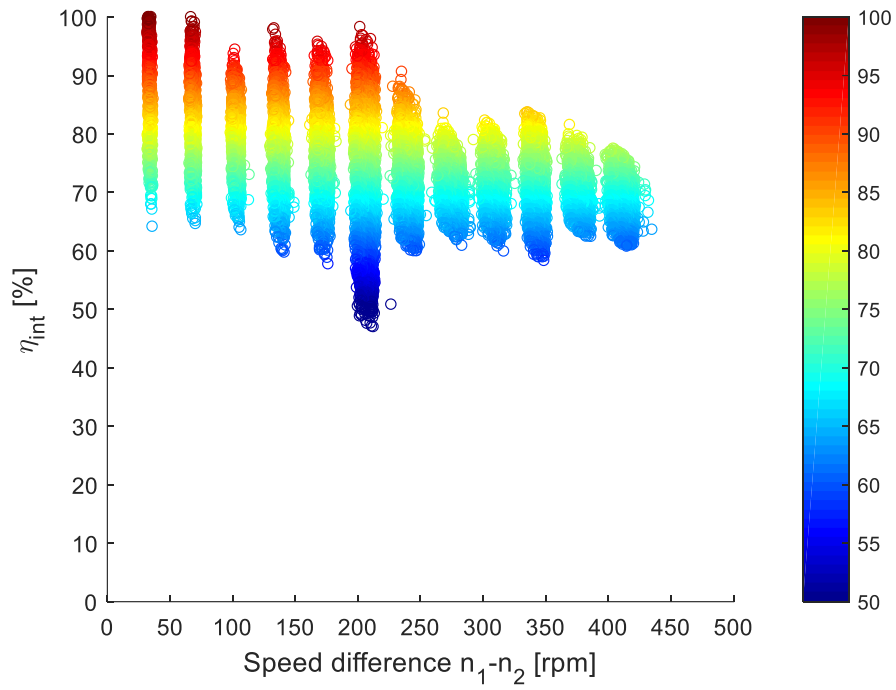


Figure 3.13 – Efficiency plot 2nd gear multiplier, $T_1=0.75$ Nm.

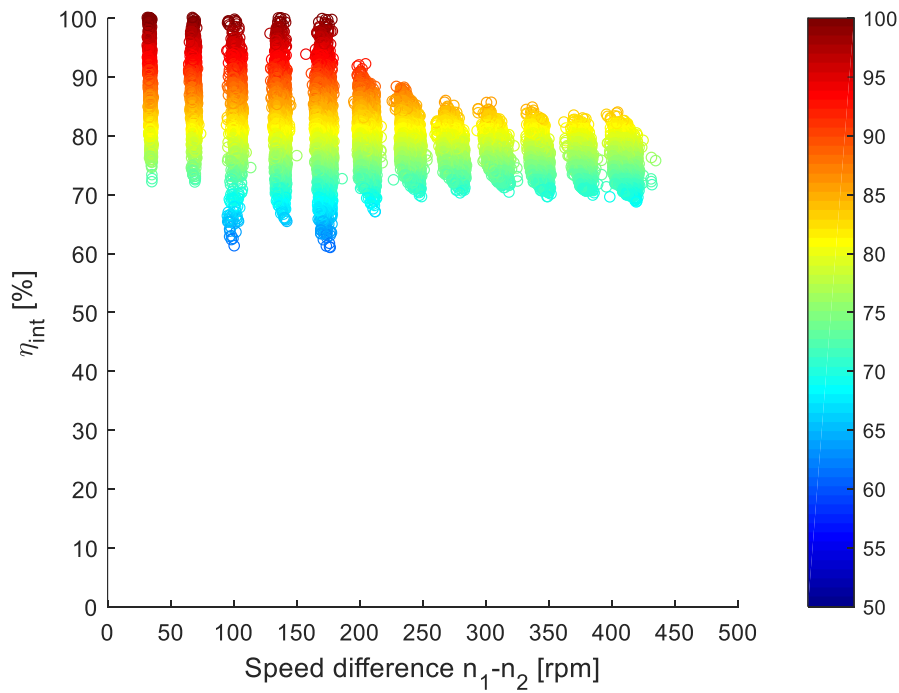


Figure 3.14 – Efficiency plot 2nd gear multiplier, $T_1=1$ Nm.

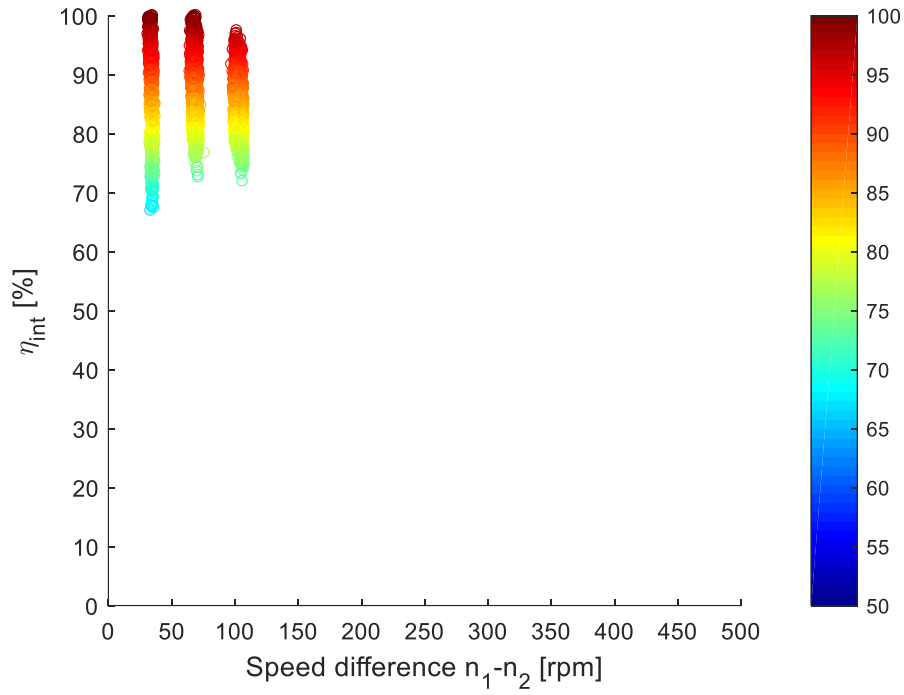


Figure 3.15 – Efficiency plot 2nd gear multiplier, $T_1=1.15$ Nm.

Then, for the first gear speed multiplier operation in Figure 3.16, Figure 3.17 and Figure 3.18.

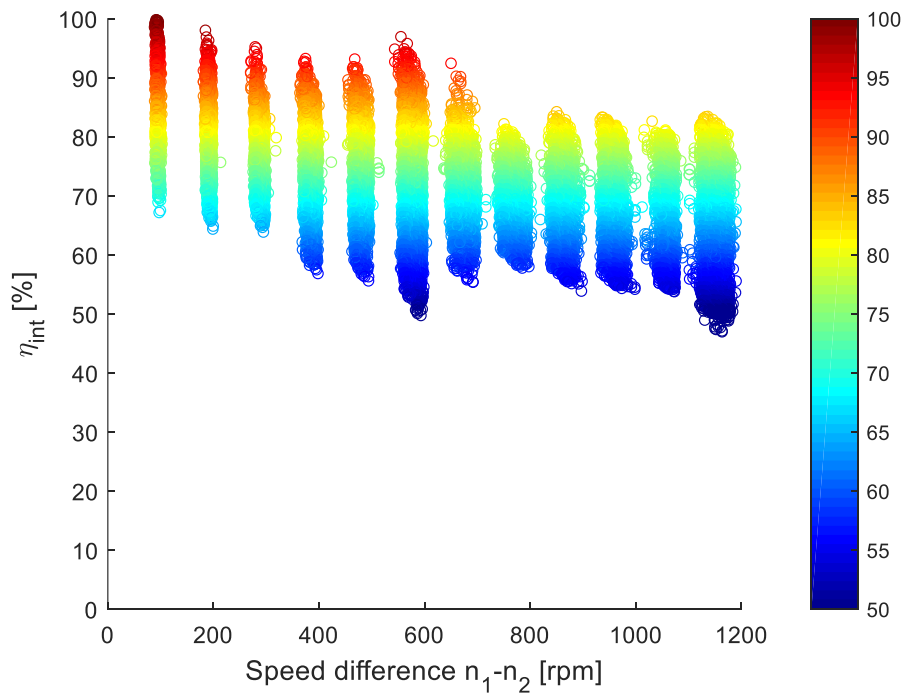


Figure 3.16 – Efficiency plot 1st gear multiplier, $T_1=0.3$ Nm.

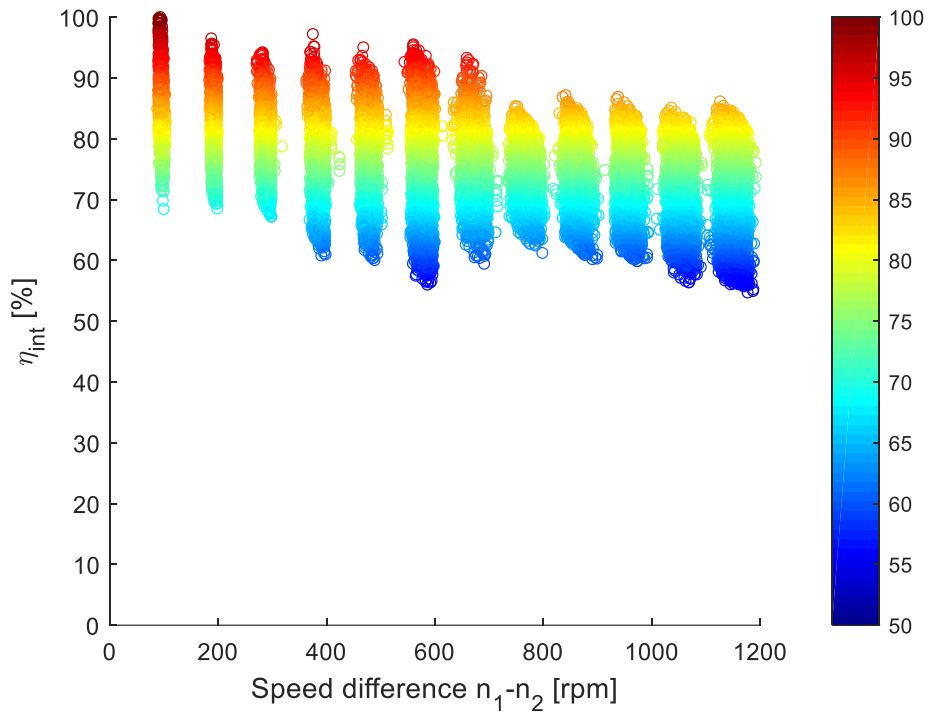


Figure 3.17 – Efficiency plot 1st gear multiplier, $T_1=0.45$ Nm.

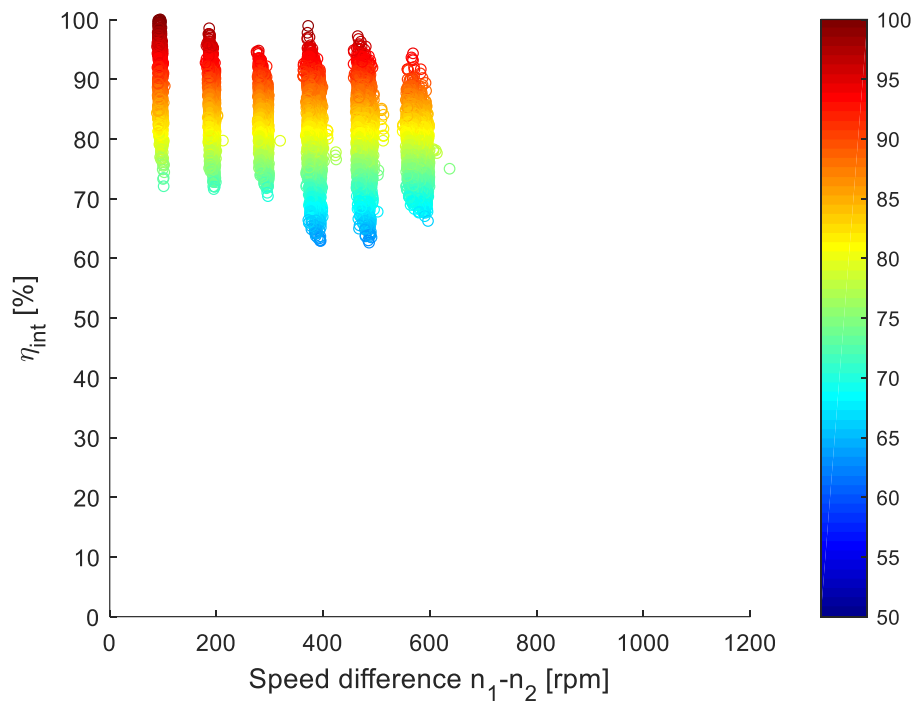


Figure 3.18 – Efficiency plot 1st gear multiplier, $T_1=0.6$ Nm.

Then comes in chronological order the first gear speed reducer operation in Figure 3.19, Figure 3.20, Figure 3.21 and Figure 3.22.

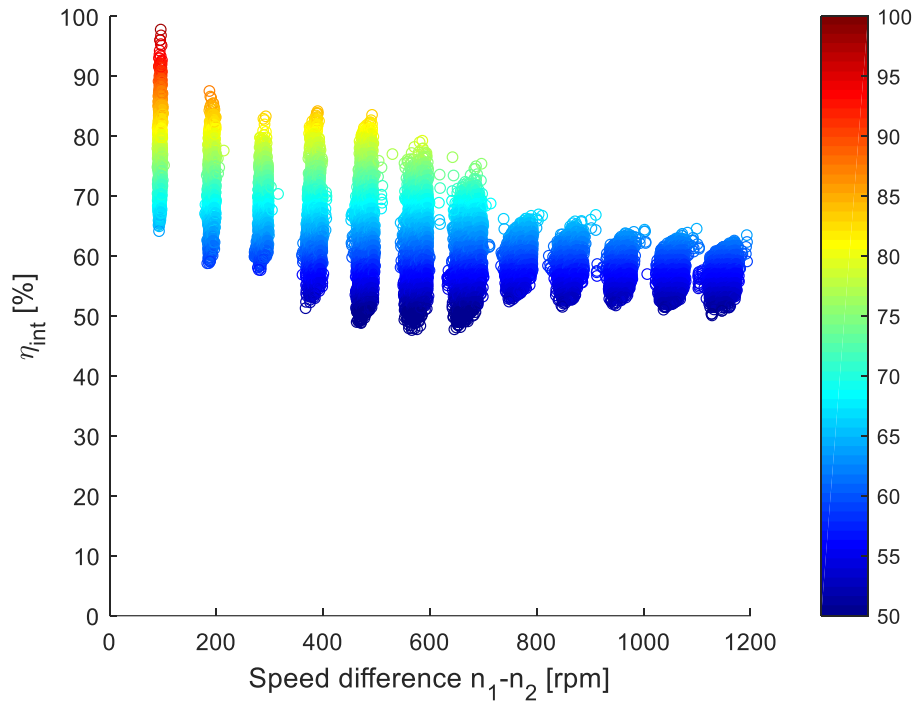


Figure 3.19 – Efficiency plot 1st gear reducer, $T_2=0.78$ Nm.

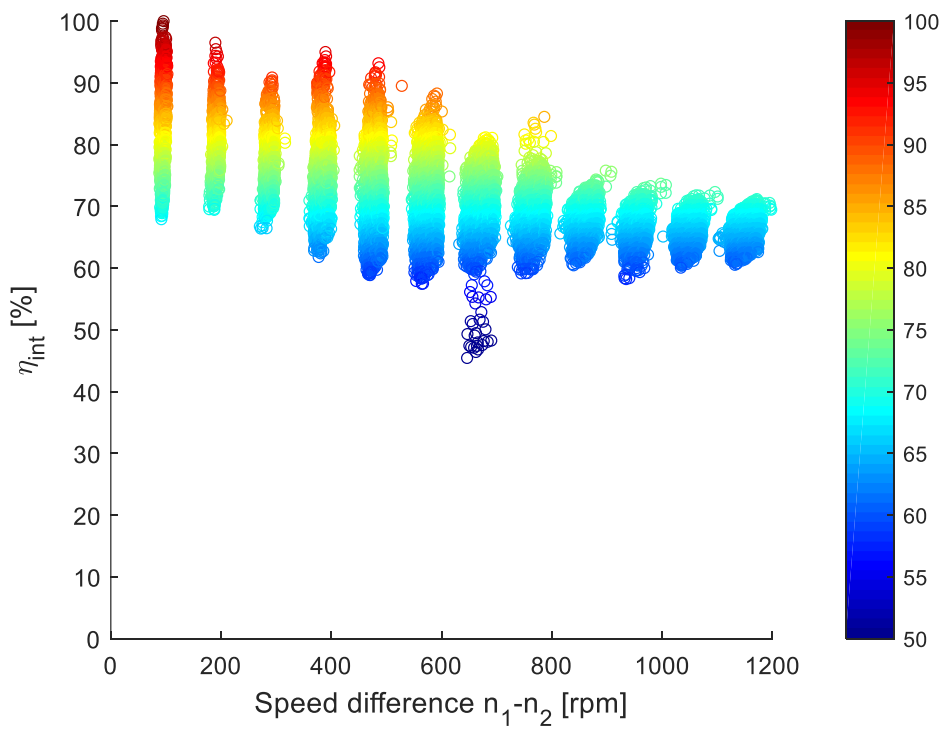


Figure 3.20 – Efficiency plot 1st gear reducer, $T_2=1.17$ Nm.

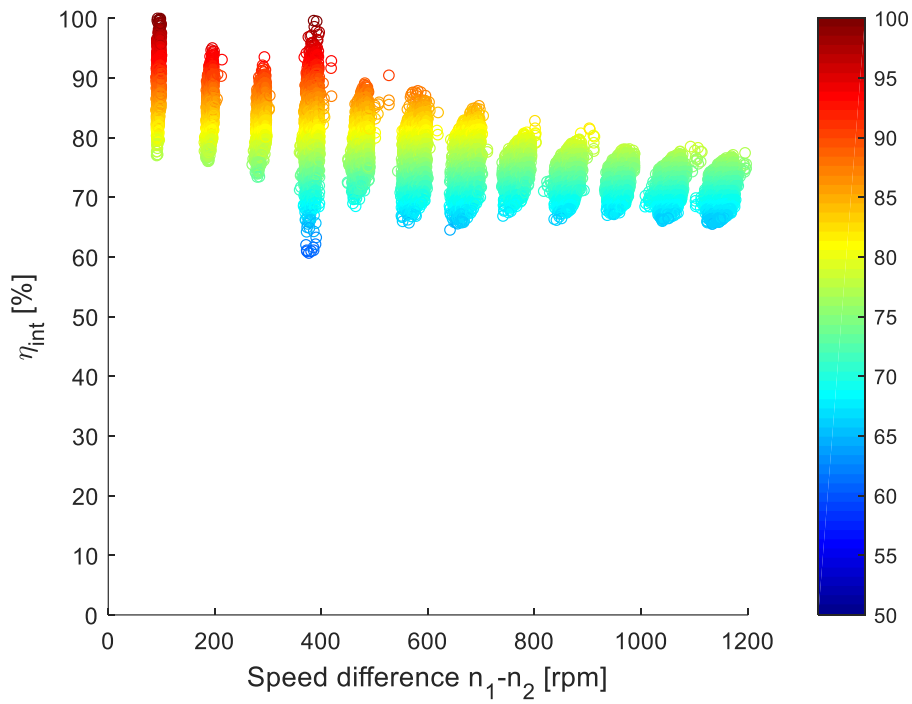


Figure 3.21 – Efficiency plot 1st gear reducer, $T_2=1.57$ Nm.

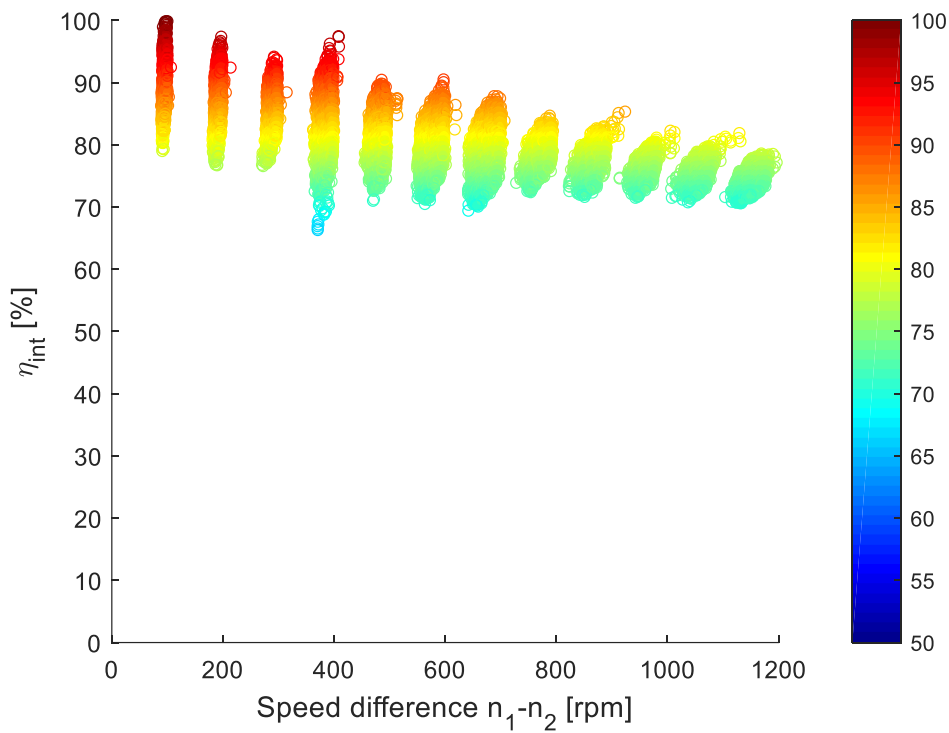


Figure 3.22 – Efficiency plot 1st gear reducer, $T_2=1.96$ Nm.

Eventually comes the second gear speed reducer operation presented in Figure 3.23, Figure 3.24, Figure 3.25 and Figure 3.26.

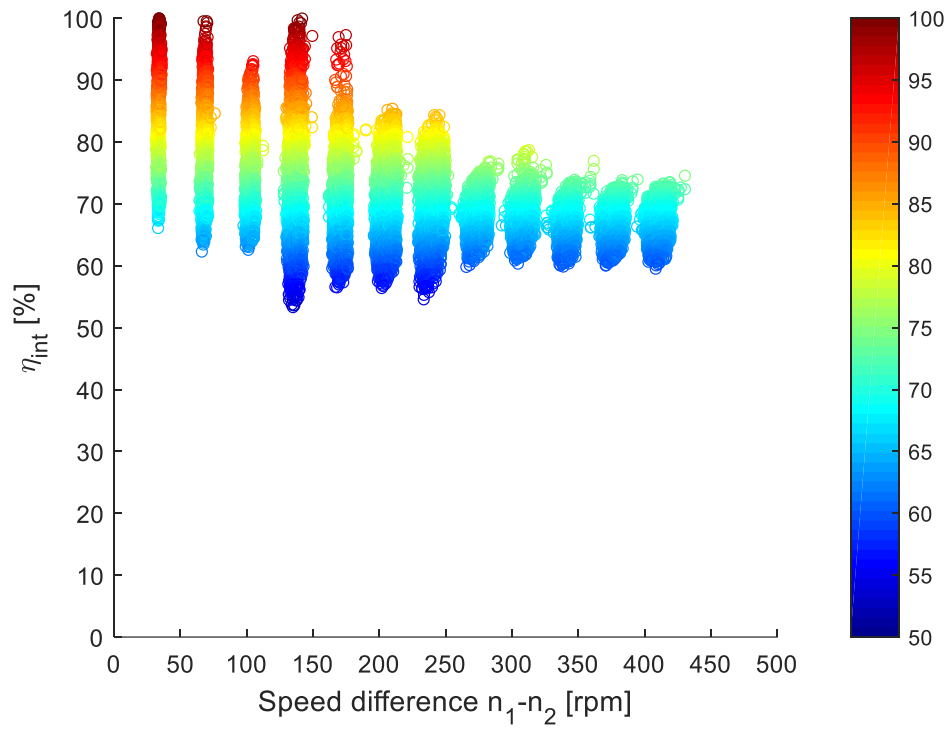


Figure 3.23 – Efficiency plot 2nd gear reducer, $T_2=0.78$ Nm.

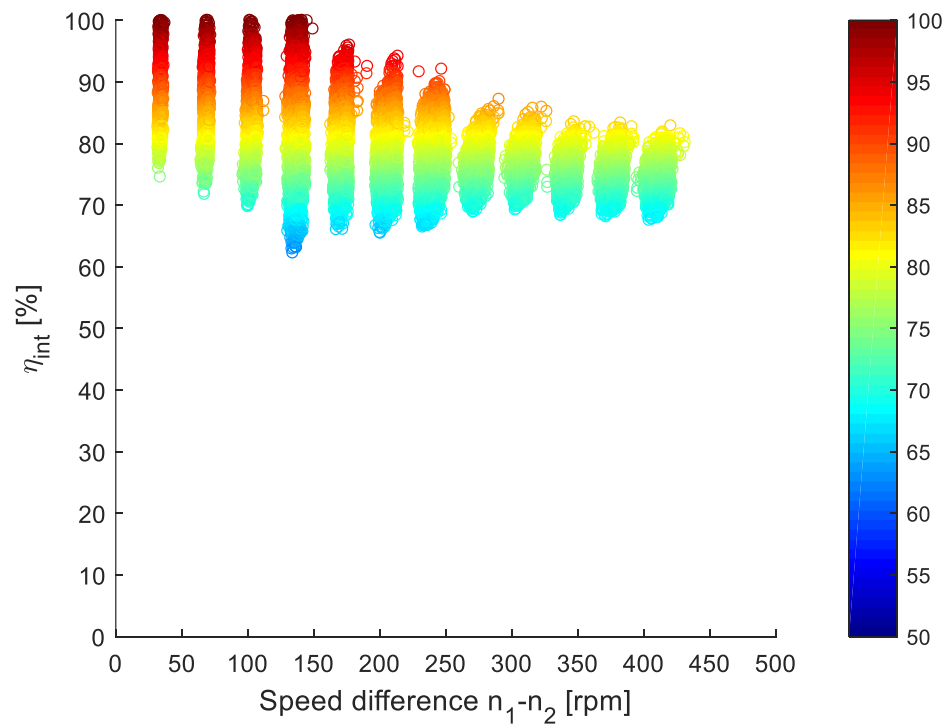


Figure 3.24 – Efficiency plot 2nd gear reducer, $T_2=1.17$ Nm.

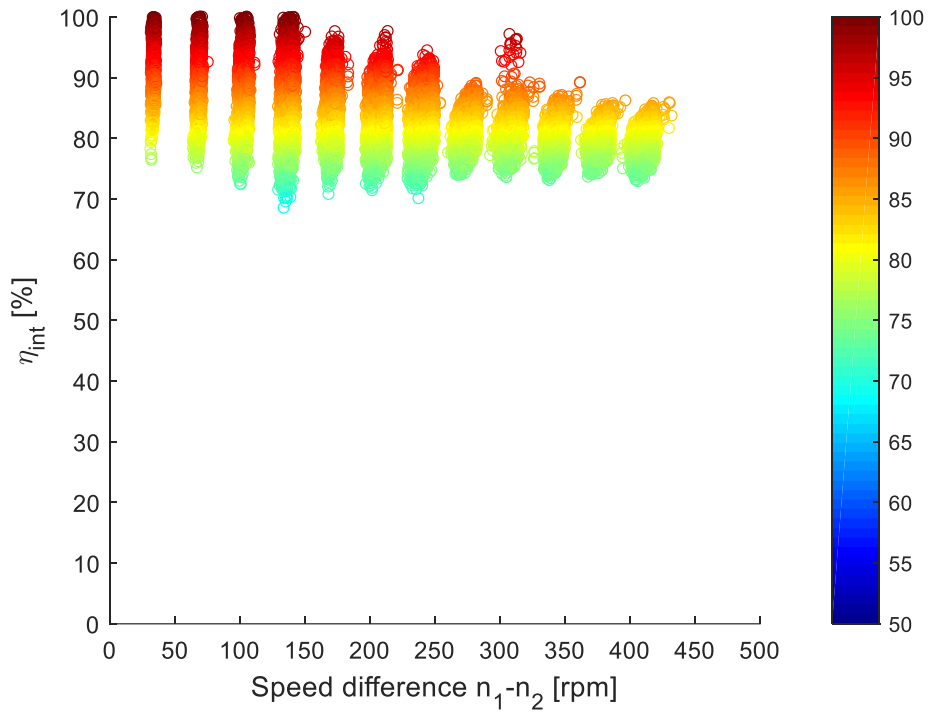


Figure 3.25 – Efficiency plot 2nd gear reducer, $T_2=1.57$ Nm.

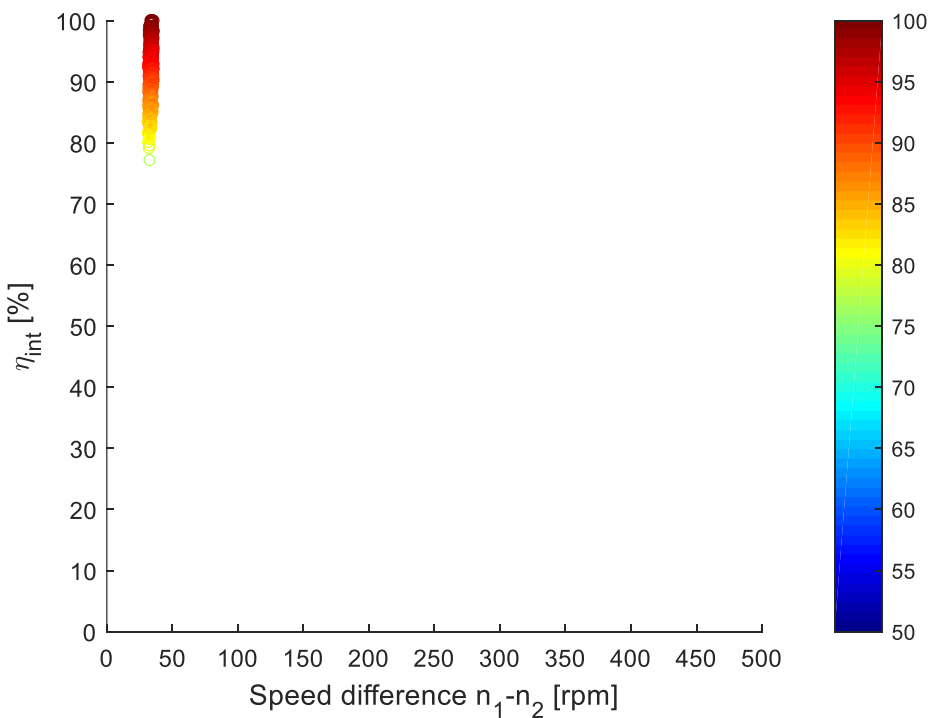


Figure 3.26 – Efficiency plot 2nd gear reducer, $T_2=1.96$ Nm.

Apart from the recurring trend with speed, there are a couple of aspects that emerge from these graphs.

The first thing is the wide range of internal efficiencies that can be featured at constant speed, and that this phenomenon diminishes with the increase of speed. This is due to the torque ripple that

occurs because of suboptimal manufacturing that leads to small unbalances during rotation, and as a consequence to more torque generated at certain angles and less torque at other angles. The second aspect is the fact that, even after the filtering of both speed and torque, some singular points would still reach over 100% efficiency due to sampling imprecisions, and therefore are just cut out in the graph.

3.2.2.5 Mean efficiency

A significant aspect is the mean total efficiency of the system. This is obtained by performing the average of the input torques and the average of the output torques at constant speed and inserting them in the formulation in §2.2.3, and not by making an average of the internal efficiencies. In the following Figure 3.27, Figure 3.28, Figure 3.29 and Figure 3.30 the graphs with the mean efficiencies are reported; the various cases of resistant torque are all presented in the same graph for comparison. Also, in the following tables, the numerical values are shown for better clarity. As previously stated, the efficiency decreases with an increase in speed (and therefore in speed difference, being the two proportional). With regards to torque ratio, the higher the resistant load imposed the higher the mean efficiency.

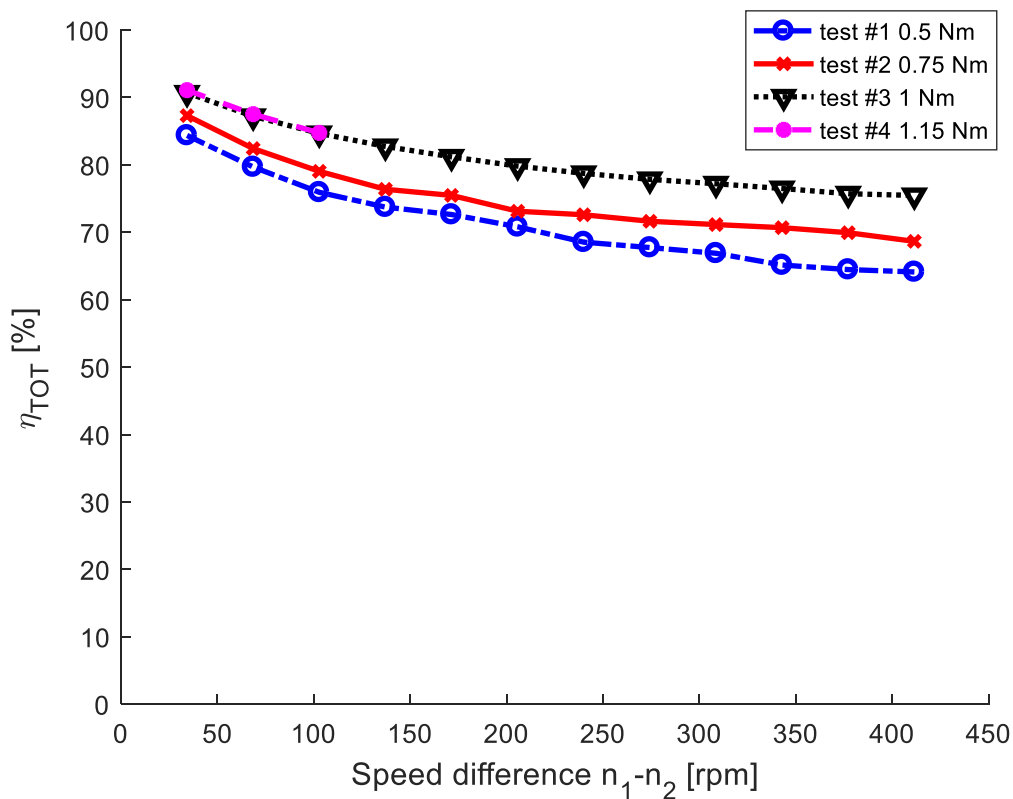


Figure 3.27 – Mean efficiency plot, 2nd gear multiplier.

Table 3.8 – Efficiency values for $T_1=0,5$ Nm, 2nd gear multiplier.

Input speed ω_2 [rpm]	Efficiency η [%]
60	84.43
120	79.71
180	75.93
240	73.76
300	72,67
360	70.84
420	68.55
480	67.73
540	66.98
600	65.14
660	64.53
720	64.16

Table 3.9 – Efficiency values for $T_1=0,75$ Nm, 2nd gear multiplier.

Input speed ω_2 [rpm]	Efficiency η [%]
60	87.33
120	82.43
180	79.05
240	76.41
300	75.50
360	73.16
420	72.67
480	71.60
540	71.12
600	70.74
660	69.98
720	68.62

Table 3.10 – Efficiency values for $T_1=1$ Nm, 2nd gear multiplier.

Input speed ω_2 [rpm]	Efficiency η [%]
60	90.70
120	87.24
180	84.73
240	82.77
300	81.20
360	79.86
420	78.72
480	77.84
540	77.23
600	76.57
660	75.73
720	75.58

Table 3.11 – Efficiency values for $T_1=1,15$ Nm, 2nd gear multiplier.

Input speed ω_2 [rpm]	Efficiency η [%]
60	91.13
120	87.52
180	84.77

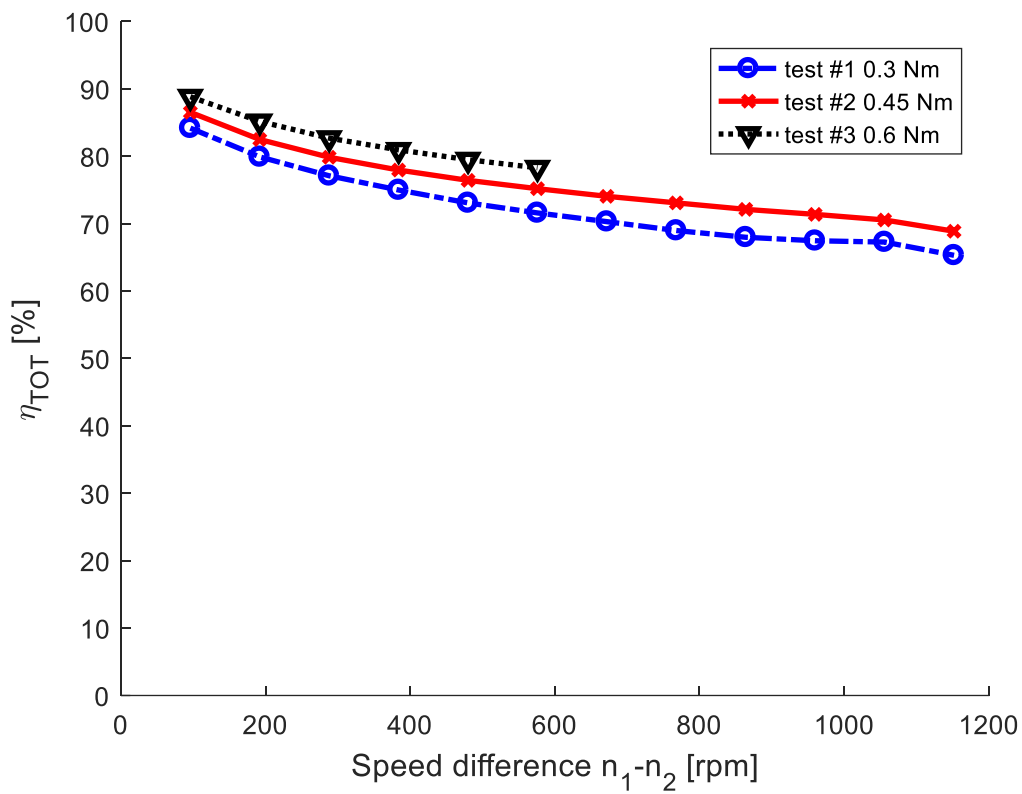


Figure 3.28 – Mean efficiency plot, 1st gear multiplier.

Table 3.12 – Efficiency values for $T_1=0.3$ Nm, 1st gear multiplier.

Input speed ω_2 [rpm]	Efficiency η [%]
60	84.22
120	79.94
180	77.15
240	75.02
300	73.17
360	71.65
420	70.33
480	69.07
540	68.02
600	67.44
660	67.32
720	65.33

Table 3.13 – Efficiency values for $T_1=0.45$ Nm, 1st gear multiplier.

Input speed ω_2 [rpm]	Efficiency η [%]
60	86.52
120	82.54
180	80.81
240	78.04
300	76.42
360	75.256
420	74.01
480	73.12
540	72.11
600	71.41
660	70.57
720	69.93

Table 3.14 – Efficiency values for $T_1=0.6$ Nm, 1st gear multiplier.

Input speed ω_2 [rpm]	Efficiency η [%]
60	88.82
120	85.15
180	82.74
240	80.94
300	79.50
360	78.31

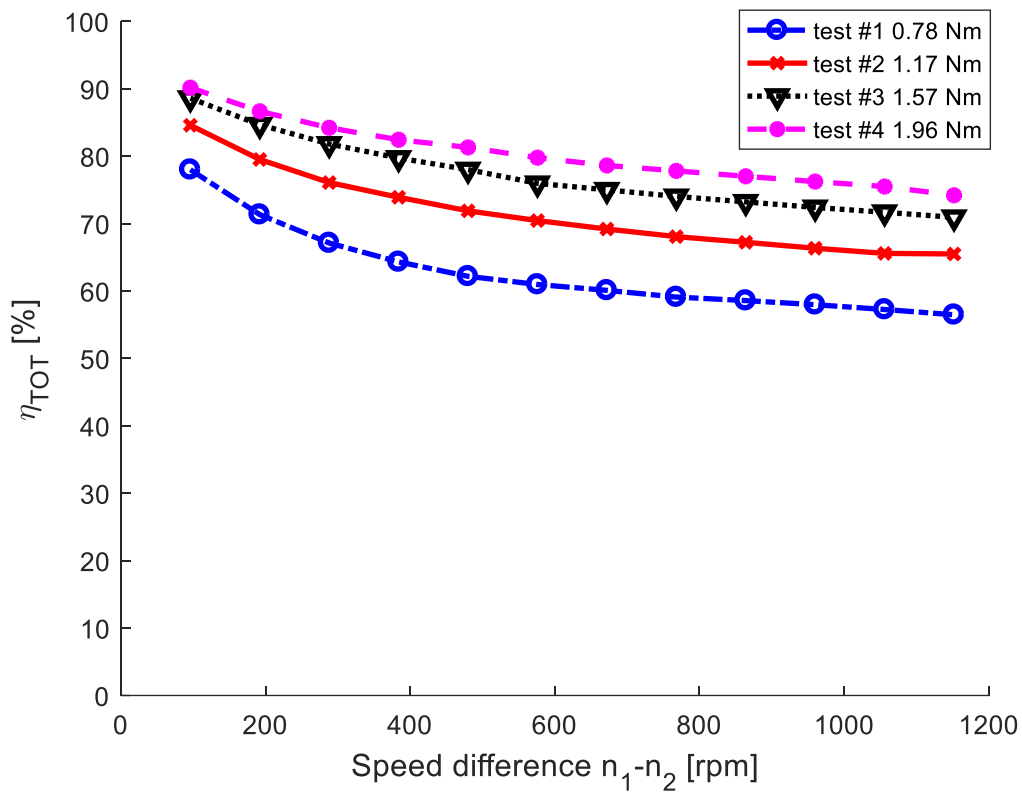


Figure 3.29 – Mean efficiency plot, 1st gear reducer.

Table 3.15 – Efficiency values for $T_2=0.78$ Nm, 1st gear reducer.

Output speed ω_2 [rpm]	Efficiency η [%]
60	78.03
120	71.32
180	67.15
240	64.37
300	62.22
360	60.95
420	60.13
480	59.16
540	58.63
600	57.96
660	57.34
720	56.51

Table 3.16 – Efficiency values for $T_2=1.17$ Nm, 1st gear reducer.

Output speed ω_2 [rpm]	Efficiency η [%]
60	84.64
120	79.53
180	76.18
240	73.95
300	71.91
360	70.40
420	69.26
480	68.15
540	67.25
600	66.37
660	65.66
720	65.52

Table 3.17 – Efficiency values for $T_2=1.57$ Nm, 1st gear reducer.

Output speed ω_2 [rpm]	Efficiency η [%]
60	88.63
120	84.62
180	81.87
240	79.74
300	78.05
360	75.93
420	75.02
480	74.06
540	73.24
600	72.47
660	71.75
720	70.95

Table 3.18 – Efficiency values for $T_2=1.96$ Nm, 1st gear reducer.

Output speed ω_2 [rpm]	Efficiency η [%]
60	90.14
120	86.62
180	84.25
240	82.47
300	81.31
360	79.80
420	78.64
480	77.86
540	77.01
600	76.22
660	75.54
720	74.26

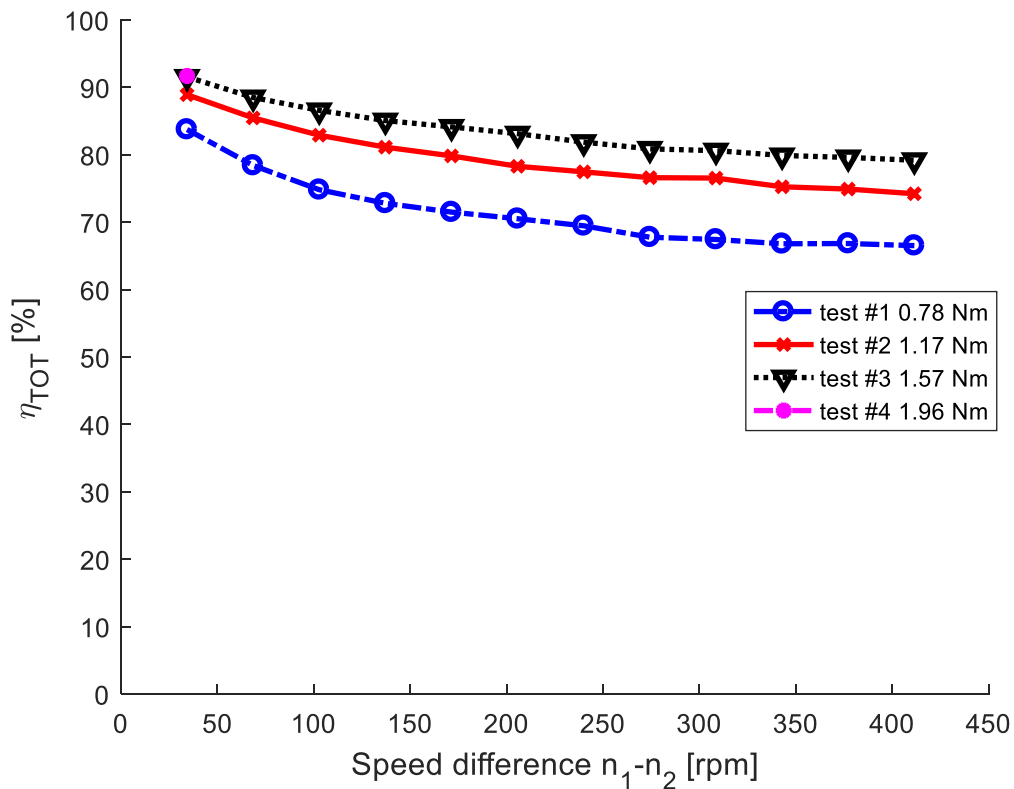


Figure 3.30 – Mean efficiency plot, 2nd gear reducer.

Table 3.19 – Efficiency values for $T_2=0,78$ Nm, 2nd gear reducer.

Output speed ω_2 [rpm]	Efficiency η [%]
60	83.83
120	78.42
180	74.86
240	72.85
300	71.55
360	70.52
420	69.58
480	67.86
540	67.43
600	66.82
660	66.83
720	66.51

Table 3.20 – Efficiency values for $T_2=1,17$ Nm, 2nd gear reducer.

Output speed ω_2 [rpm]	Efficiency η [%]
60	88.91
120	85.53
180	82.92
240	81.17
300	79.84
360	78.38
420	77.59
480	76.62
540	76.51
600	75.36
660	74.94
720	74.23

Table 3.21 – Efficiency values for $T_2=1,57$ Nm, 2nd gear reducer.

Output speed ω_2 [rpm]	Efficiency η [%]
60	91.63
120	88.52
180	86.65
240	85.16
300	84.17
360	83.13
420	81.94
480	80.93
540	80.60
600	79.92
660	79.61
720	79.23

Table 3.22 – Efficiency values for $T_2=1,96$ Nm, 2nd gear reducer.

Output speed ω_2 [rpm]	Efficiency η [%]
60	91.75

3.2.3 Loss contributions

After the total efficiencies have been calculated, the next step is to understand how to break them down to the two contributions of mechanical efficiency, which is mainly the result of friction inside the rolling bearings, and of magnetic efficiency, which is due to the magnetic effects during the transmission and conversion of motion through the permanent magnets and the ferromagnetic pole pieces.

The division, as stated in [33] and shown in Figure 3.31, needs to put the mechanical contributions ahead of the electromagnetic ones.

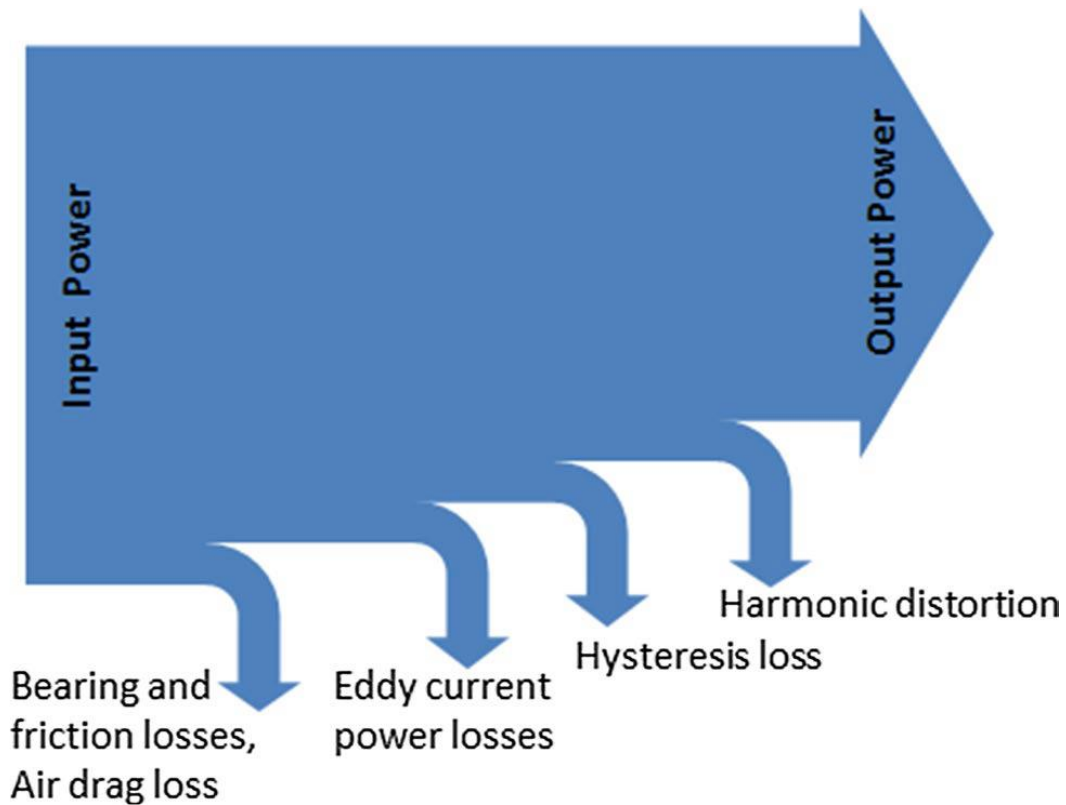


Figure 3.31 – Ordered sequence of loss contributions in PMG power transmission.

Therefore, starting from the mechanical parts, the first thing to be done is determining which bearings are subject to which angular speeds. In this way, even the contributions inside the mechanical losses can be separated. The only possible way without disassembling the structure is to use the online SKF tool for bearings. This tool allows to input the kind of bearing and the value of speed and load to which the bearing is subject. Furthermore, in the case of the bearing W 61802-2Z, there are both the internal and the external ring rotating (counterphase); so, the relative speed has been considered.

A loss coefficient has been used to put into numbers the mechanical dissipations (eq. (3.2)). The concept behind this formula is to isolate the bearings frictions and to equal these to the whole mechanical dissipations occurring; the quantities treated are powers, therefore the singular torques obtained from the SKF tool need to be multiplied by the speed at which each bearing rotates. The numbers for the bearings are presented once again for clarity in Figure 3.32.

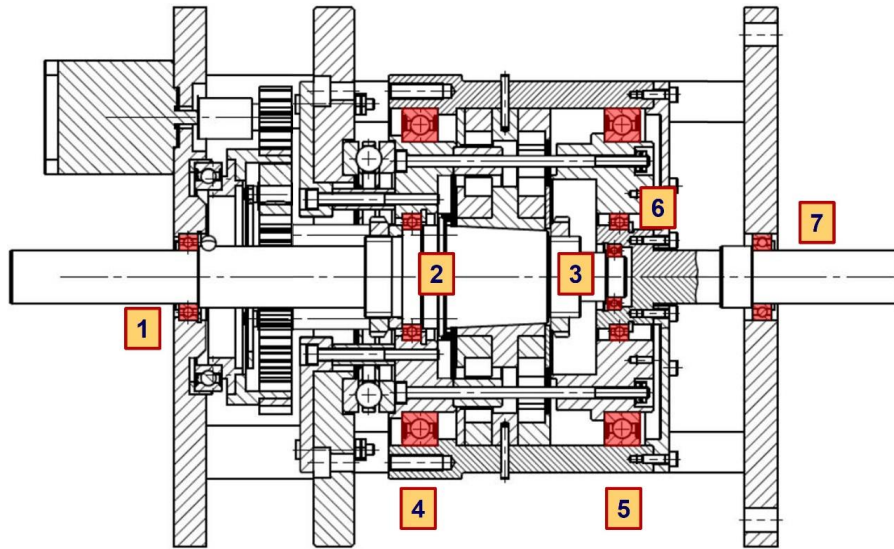


Figure 3.32 – 2D section view of the magnetic gearbox with the bearings highlighted and numbered for identification.

The normalisation to the input power at denominator allows to then derive the mechanical efficiency easily by subtracting the value from the unit.

$$\gamma_B = \frac{(T_{b1} + T_{b2})\omega_1 + (T_{b4} + T_{b5} + T_{b6} + T_{b7})\omega_2 + T_{b3}(\omega_1 + \omega_2)}{T_{in}\omega_{in}} \quad (3.2)$$

This technique, however right in theory, is not well backed up by the SKF tool itself, which is not accurate to the level required as will be explained later in the chapter. This doesn't mean that the relative contribution of the various bearings is not well respected in the values obtained. On the contrary, a good depiction of the contributions is given.

For this reason, together with the display of the SKF points, an interpolation has been made so to have a visual trend of how the individual bearings react to different speeds with different speeds.

Since bearings 1 and 7, 2 and 6, 4 and 5 are the same, only four bearing losses trends are present.

The use of the SKF tool doesn't allow to immediately know the type of analytical trend best fitted for the torque losses given. Therefore, a custom function named polyLMS has been initially used.

This tool allows to interpolate the points in a polynomial function, and to choose the degree of the said polynomial. However, the nature of this type of interpolation gives results that are not acceptable. As shown in Figure 3.33, although the trend lines give a good interpolation in between the given points, once the function extrapolates outside the range of the points it immediately diverges either to infinity as in this case (with an odd-degree polynomial) or to negative infinity (with an even-degree polynomial).

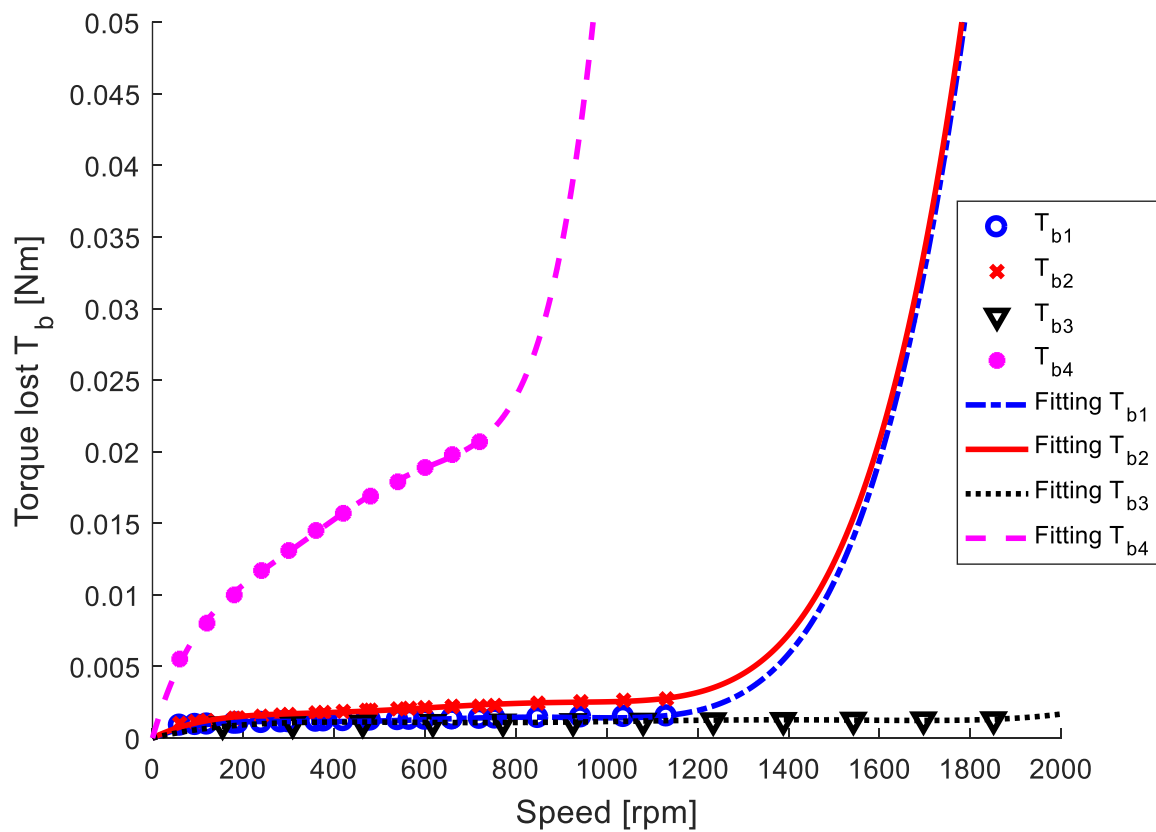


Figure 3.33 – Torque loss trend for the bearings using polyLMS.

For this reason, the type of interpolation has been changed to a better one.

Looking at the points, the trend resembles that of a less than linear function. Starting from this assumption, a new interpolator called polyAlphaLMS has been developed. This function gives an output of the type Cx^{Alpha} , and $Alpha$ is expected to be between zero and one.

In Figure 3.34 the new trends for the singular torques are presented

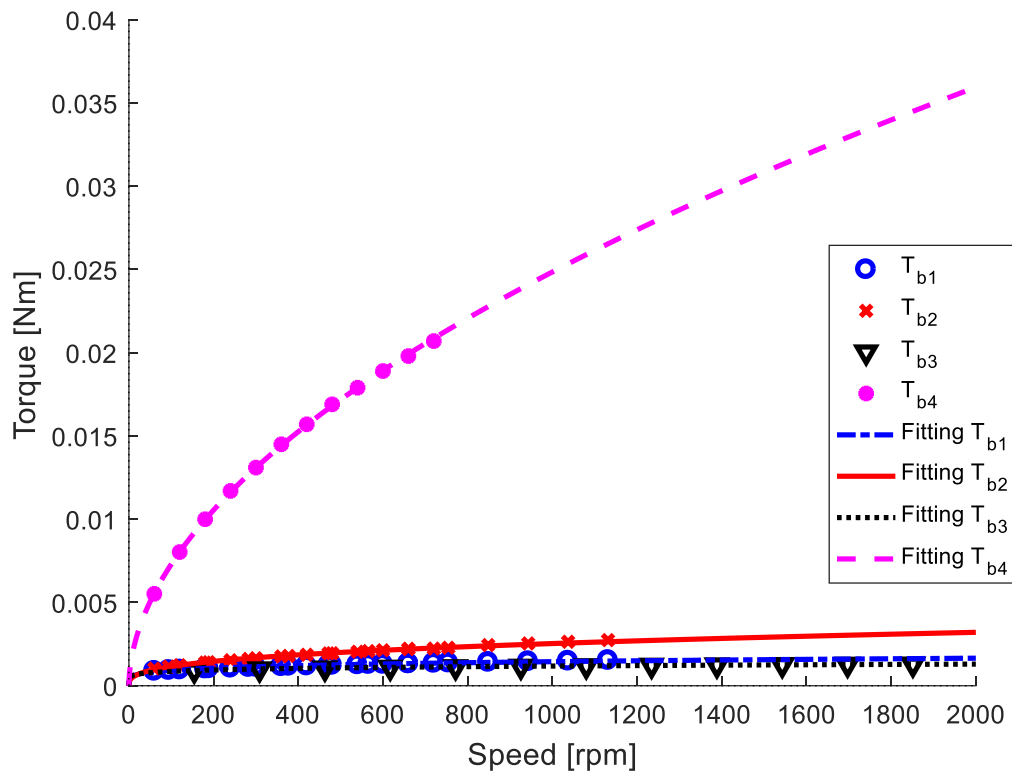


Figure 3.34 – Torque loss trend for the bearings using polyAlphaLMS, contributions.

A cumulative case is shown in Figure 3.35.

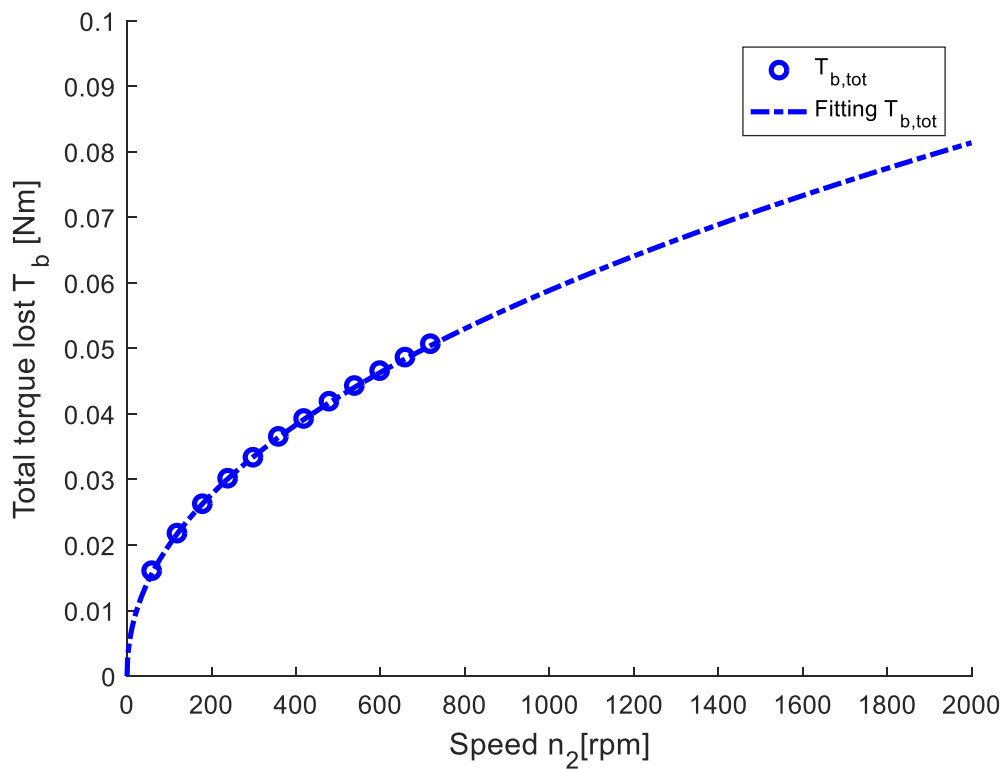


Figure 3.35 – Torque loss trend for the bearings using polyAlphaLMS, cumulative.

This new extrapolation preserves the accuracy between the points and is optimised for higher speeds.

It is then possible to get the amount of power absorbed by the bearings. The results for the individual bearings and the total are shown in Figure 3.36 and Figure 3.37.

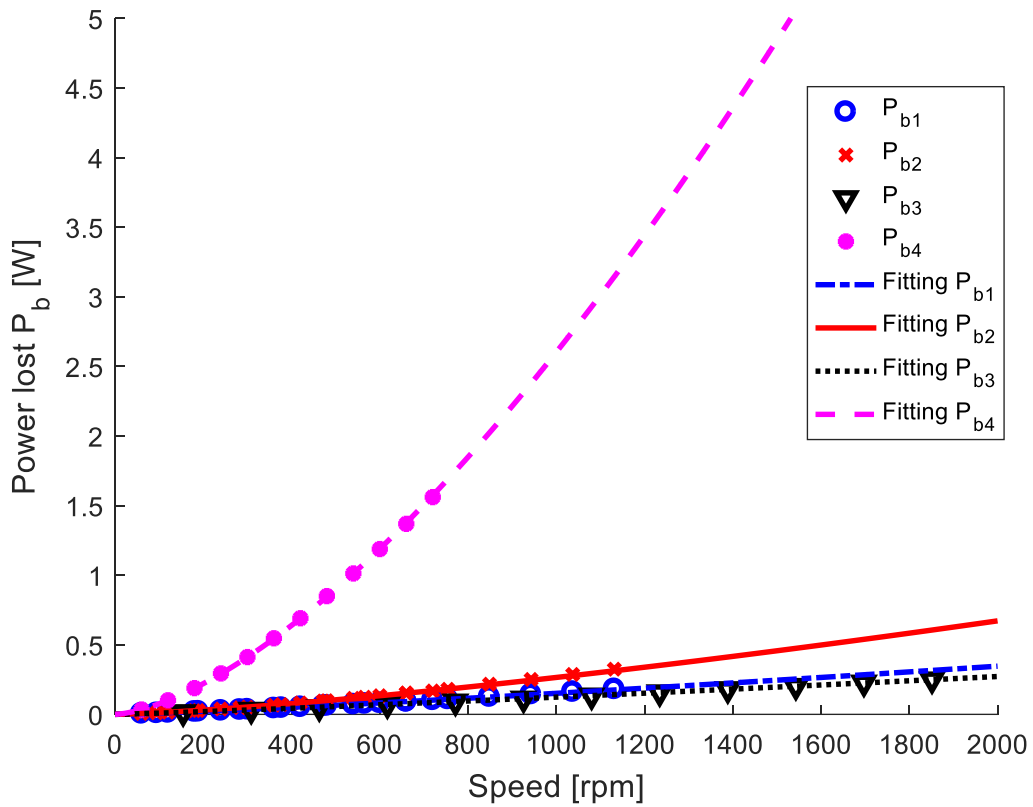


Figure 3.36 – Power loss trend for the bearings using polyAlphaLMS, singular.

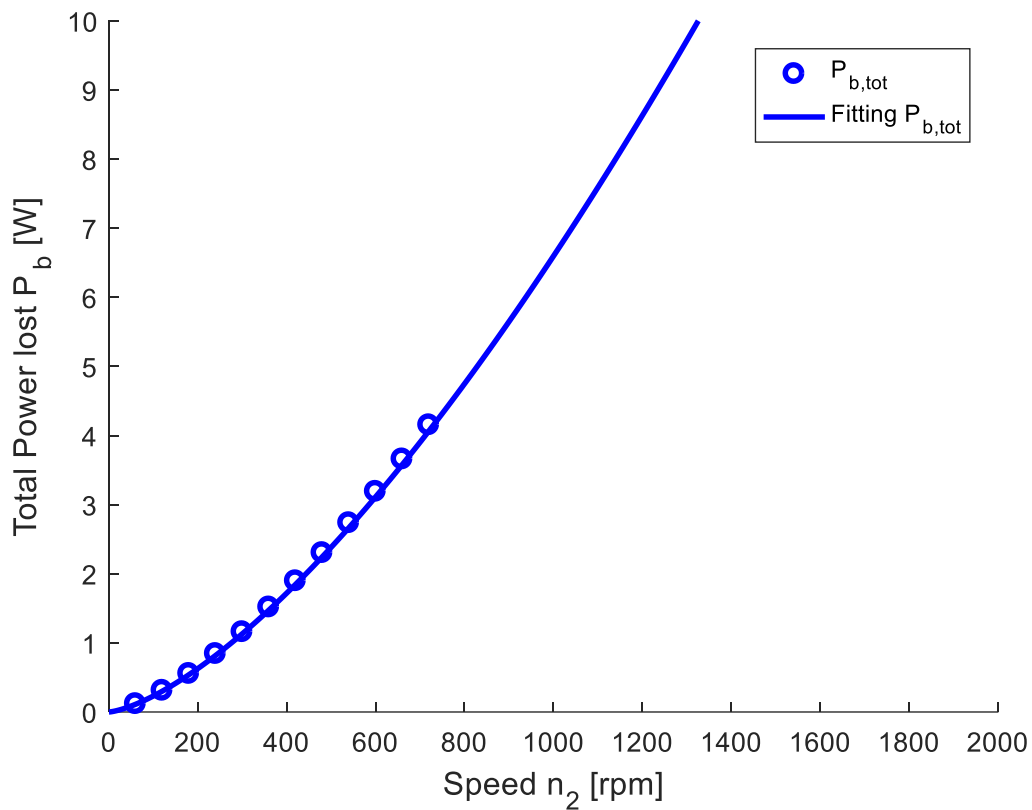


Figure 3.37 – Power loss trend for the bearings using polyAlphaLMS, cumulative.

Provided that, as previously stated, the numerical values are off, the relative contributions are preserved. It is then clear that the bearings number 4 and 5 take on the majority of the losses, while the others have an increasingly marginal role with speed increase. Out of all, the bearing number 3, the only one with relative motion between the two shafts, has the least impact.

3.2.3.1 Mechanical efficiency

Therefore, the mechanical efficiency η_B is the complement to 1 of the loss coefficient (eq. (3.3)), as stated in §2.3.

$$\eta_B = \frac{P_{IN} - P_{LOSS,B}}{P_{IN}} \quad (3.3)$$

Where P_{IN} is the power input and $P_{LOSS,B}$ is the power dissipated in the bearings. As reported in the next figure (Figure 3.38), it is now clear why in §2.3 the SKF method has been deemed unsuitable.

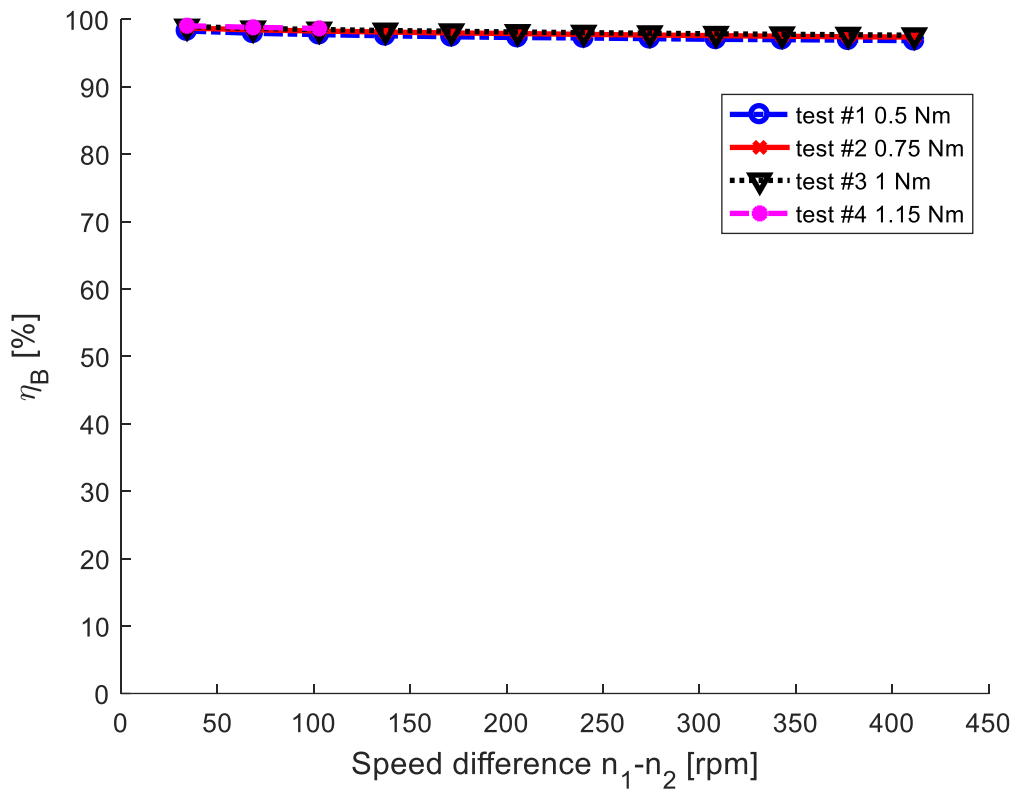


Figure 3.38 – Mechanical efficiency plot, 2nd gear multiplier case.

The mechanical efficiencies, compared to the total efficiencies, are way too high with respect to what would be predicted: the mechanical efficiency should be almost comparable to the total efficiency for the following reason: the dimension of the bearings is significantly higher than the dimension of the magnetic parts, that add up to only a small fraction of the total volume and are not even all active at the same time (either first or second gear).

For this reason, only an example of the graphs obtained through this method is shown in this section. In this case, the graph is referred to the second gear speed multiplier case.

3.2.3.2 Magnetic efficiency

The next step is to investigate the remaining losses. These are the values that, combined with the efficiencies of the mechanical parts, give as a result the total efficiencies.

Given now the magnetic losses being downstream the mechanical losses as stated in §2.3, the magnetic efficiency η_M is identified as reported in eq. (3.4).

$$\eta_M = \frac{P_{OUT}}{P_{IN} - P_{LOSS,B}} \quad (3.4)$$

Where P_{OUT} is the power at disposal of the utilities. This formulation is the only one possible, since if combined with the magnetic one gives the right result as will be shown in §2.3.3.

As for the mechanical efficiency case, here is presented only an example graph from the second gear multiplier case (Figure 2.35).

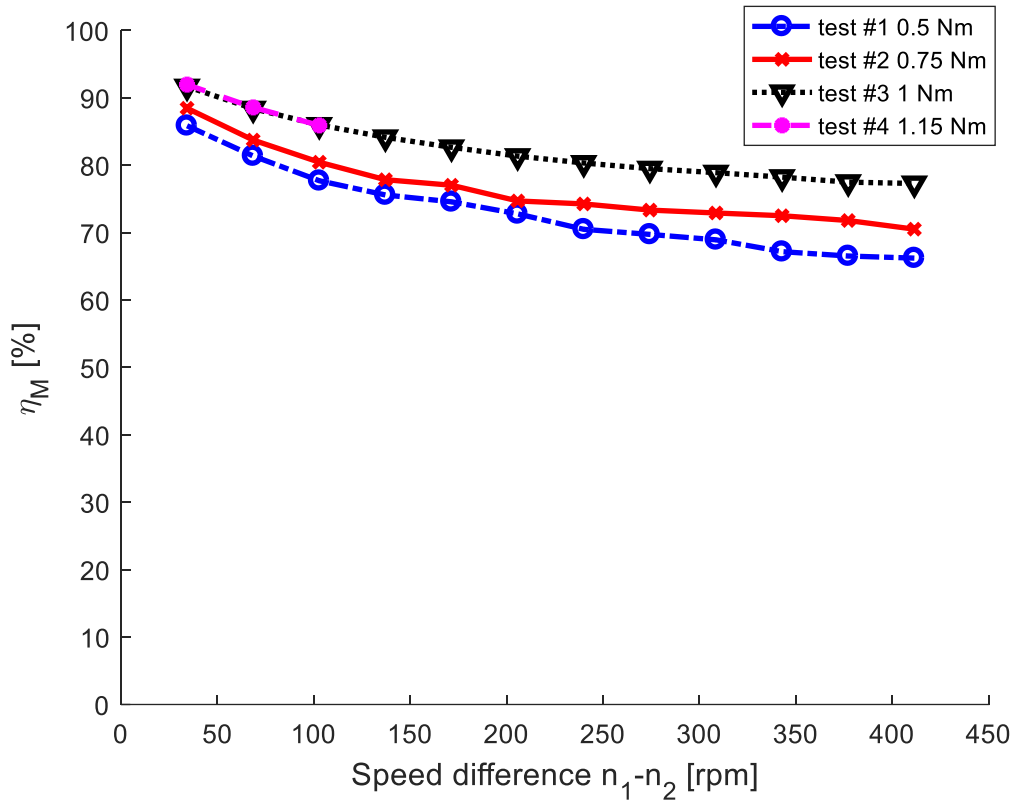


Figure 3.39 – Magnetic efficiency plot, 2nd gear multiplier case.

Once again, the magnetic efficiency is so low that it resembles the total efficiency. Although the formulations are correct, the realisation of the mechanical loss contribution that goes into it needs to be achieved in another way.

3.2.3.3 Total efficiency

Just for the sake of clarity, by multiplying the two efficiency terms the total magnetic-mechanical efficiency is obtained (eq. (3.5)).

$$\eta_{TOT} = \eta_B \eta_M = \frac{P_{IN} - P_{LOSS,B}}{P_{IN}} \frac{P_{OUT}}{P_{IN} - P_{LOSS,B}} \quad (3.5)$$

This value is identical to the efficiency that was calculated in eq. (3.1). as the physical meaning is the same.

3.2.4 Efficiency considering the no-load data

With the data gathered up to this point, it is possible to perform one more procedure. In §2.1.3 it has been stated that the torque registered on the input shaft would have been equal to the total torque dissipated. This assumption is approximate but, if considered, can be useful to understand the power losses better.

In eq. (3.6) this torque is subtracted to the input torque in the loaded case (both have to refer to the same side, speed and engaged gear) and a new type of efficiency is derived with the user power at numerator.

$$\eta = \frac{T_{1,C} \omega_1}{(T_{2,C} - T_{2,V}) \omega_2} \quad (3.6)$$

The more this fraction tends to the unit (100%) the more the assumption made is correct. The results are shown in Figure 3.40.

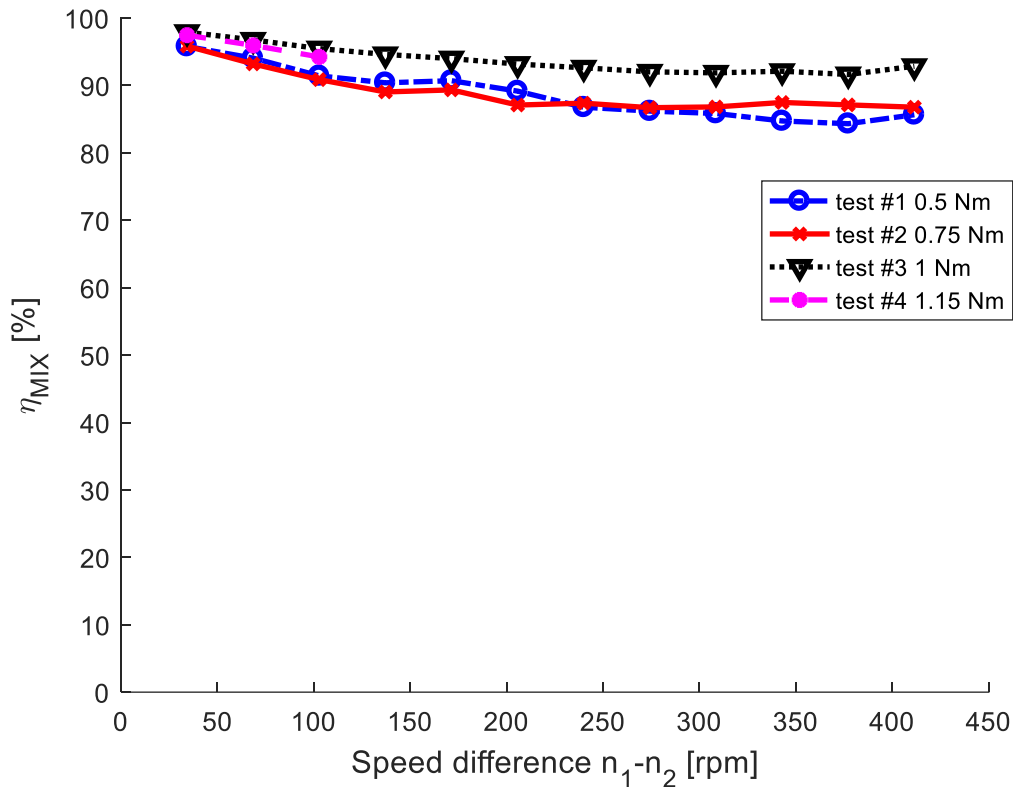


Figure 3.40 – Combined efficiency plot, 2nd gear multiplier case.

3.2.5 Functional failure

As was said earlier, the physical limit of transmission has been reached in multiple cases. In the second gear multiplier case between the 180 rpm and the 240 rpm levels with 1.15 Nm load, as shown in Figure 3.41 with a screenshot of the LabView project with the functional failure moment.

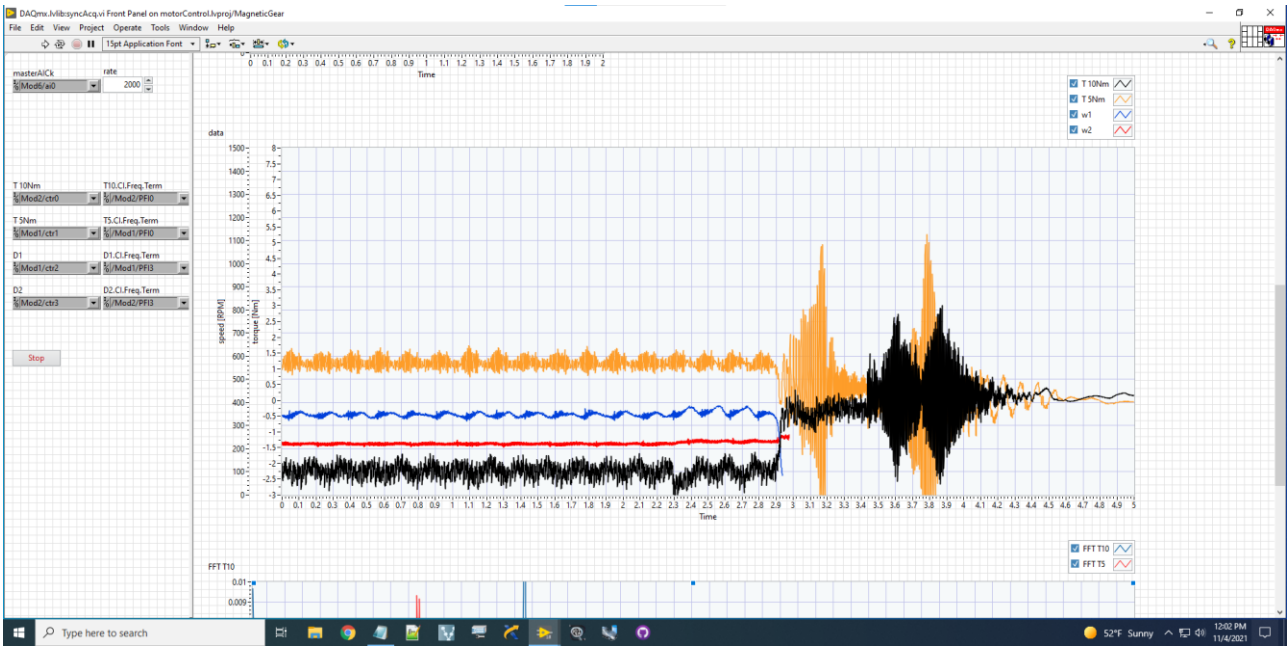


Figure 3.41 – Graphical representation of the failure, 2nd gear multiplier.

Since, as stated before, the software stops sampling once the speed goes below 60 rpm, the graph automatically interrupts the recording and presents the portrayal of what happened to the torques and the speeds. In particular, it is possible to see that, as soon as we try to pass from 230 rpm to 240 rpm, the speed on the sun side drops rapidly to zero until it eventually starts increasing in the other direction; this cannot be displayed for the sampling reasons just stated but can be only seen in person. The input torque drops almost to zero and the resistant torque starts oscillating vigorously around a value which is inferior to the nominal one. After this failure, the emergency button is pushed, and both torques are forced to go to zero. making another big oscillation in the process. The failure graph for the first gear multiplier case has been collected as well. In this case the test stops at 360 rpm and 0.6 Nm resistant load (Figure 3.42).

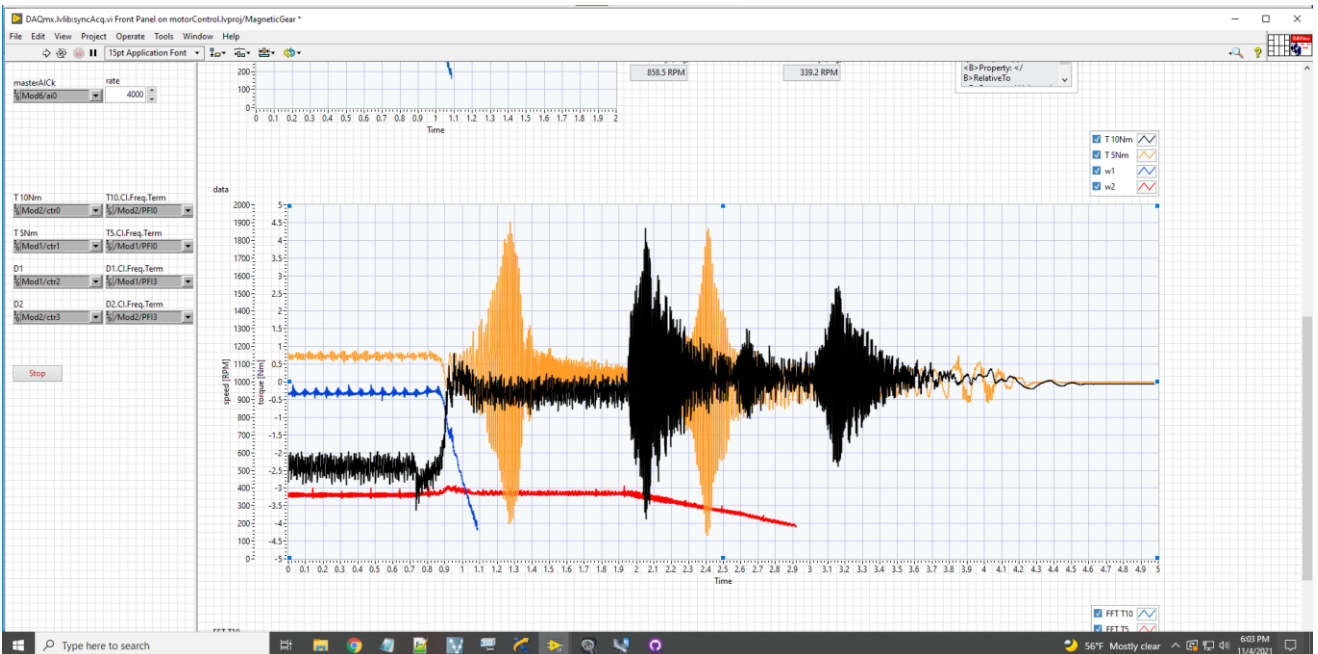


Figure 3.42 – Graphical representation of the failure, 1st gear multiplier.

In this case the system fails as soon as the speed is brought from 360 rpm to 370 rpm. The software shows a greater portion of speed data just because it takes longer to reach the 60 rpm limit starting from 370 rpm, but the process is fundamentally the same as before. The point of initial failure and the point of intervention with the emergency button are identifiable as before.

3.2.6 Conclusions

Resuming the content of this chapter, after the acquisition phase of both the no-load and loaded tests, a visual representation of the efficiency of the system is offered. The graphs show how the efficiency, keeping other conditions constant, decreases increasing the speed of the system (coherently with the graphs that show how the no-load losses increase with speed), and increases increasing the resistant load. After this, an attempt to address the specific contribution to power losses has been done. The division of the mechanical and magnetic efficiency relies on the determination of the mechanical losses, that has been initially attempted by using the SKF tool. This tool, however, doesn't provide an exact depiction of what these mechanical losses are, just by looking at the results given for the efficiencies. It is still a useful tool to determine the relative contribution of the singular bearings, nonetheless.

3.3 Neutral gear

In this section the neutral operation on the PMG is tested. The neutral is a non-engaged position of the static carrier inside the magnetic gear, meaning that the ferromagnetic carrier couples with neither the first nor the second gear but is kept at an intermediate position.

The goal of the lab activity is to gather different sets of values in order to have a full understanding of the mechanical behaviour of the test bench. Once the acquisition phase is over, the post processing takes place so that a quantitative analysis can be implemented.

In this way, at least in principle, an isolation of the mechanical losses can be obtained, assuming the border effects to be zero since the magnetic components don't interact with one another.

An image from the CAD project of the PMG in Figure 3.43 represents the position of the carrier during the neutral operation.



Figure 3.43 – Internal position of the carrier for neutral gear

3.3.1 Neutral operation

For the neutral position tests, the two sides are decoupled and therefore the motion is not transmitted. In doing so both sides can simultaneously work in speed control as there are no constraints downstream. In this condition valuable data can be extrapolated: the torques detected by the load cells only reflect the torques needed by the respective side of acquisition to maintain the fixed speeds, and therefore only take into account possible mechanical frictions as the magnetic interferences are prevented from happening.

3.3.2 Old data

3.3.2.1 Acquisitions

The acquisitions involve two different set of data, with the first one being the old set of data and the second one being the new and definitive set, as anticipated in §1.7.

The first set involves a thick coverage of a very brief range of speeds, going from 60 rpm up to 360 rpm and a with a step of 30 rpm for both the ring and the sun, with every possible combination of the two sides; this formed a 11x11 table for a total of 121 single tests.

In this phase, to see if the torques have a dependence on the sequence of acquisition, a reduced set of decreasing speeds has been performed from 300 rpm to 60 rpm with a 60 rpm step.

The direction of rotation for the shafts is key: if the two were to rotate in the opposite direction as in the engaged operation, the data would not be gatherable, since the torque wouldn't oscillate around an equilibrium position but would have an impulse-like behaviour. Therefore, the two shaft need to rotate in the same direction.

The tests were performed at 1 kHz of sampling frequency.

3.3.2.2 Signals filtering

In this case the filtering only involved the torques acquired, and it did so by using the same digital filter that was used in the engaged tests. The speeds involved were just considered as their nominal input value since it doesn't make a difference and reduces the passages.

3.3.2.3 Torque losses

Starting from the former 11x11 grid data, the values themselves are correct, but the needs of this work don't coincide with them.

The utility of these data is, as stated in §3.2.1, to see if there is a dependence with the sequence of acquisition; in Figure 3.44 and Figure 3.45 the trending lines from the sun side confirm that there is no correlation.

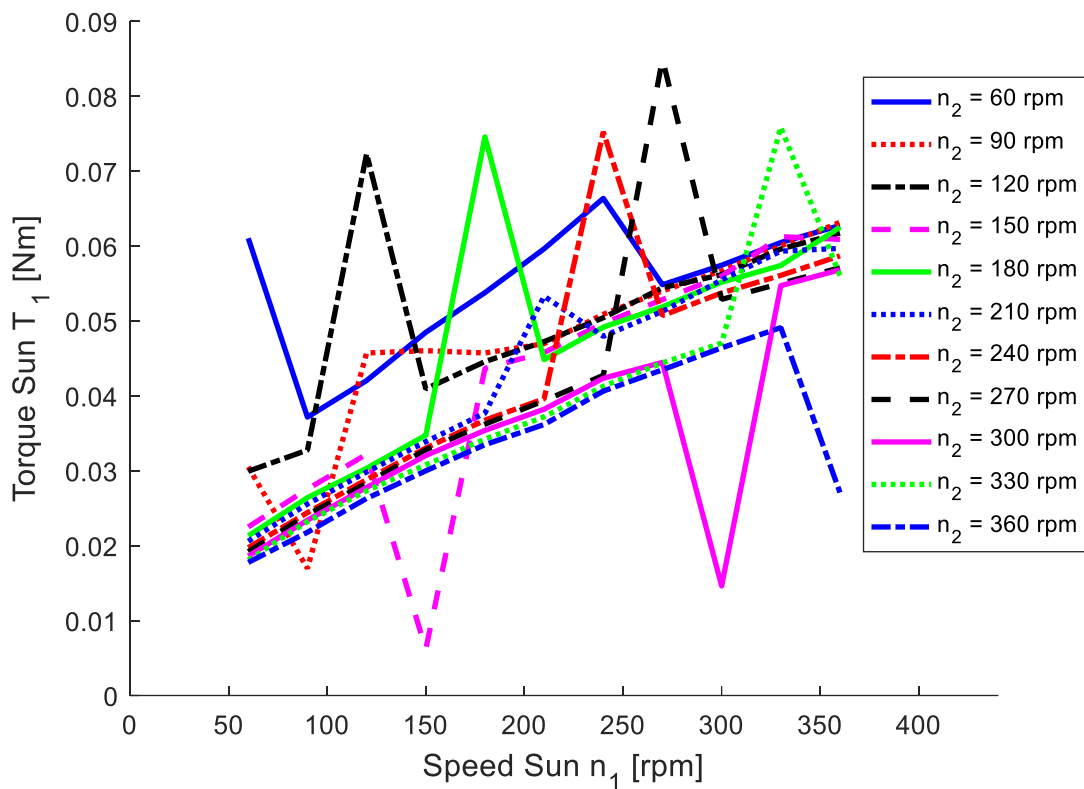


Figure 3.44 – Torque loss values in the sun side load cell, ascent principal data.

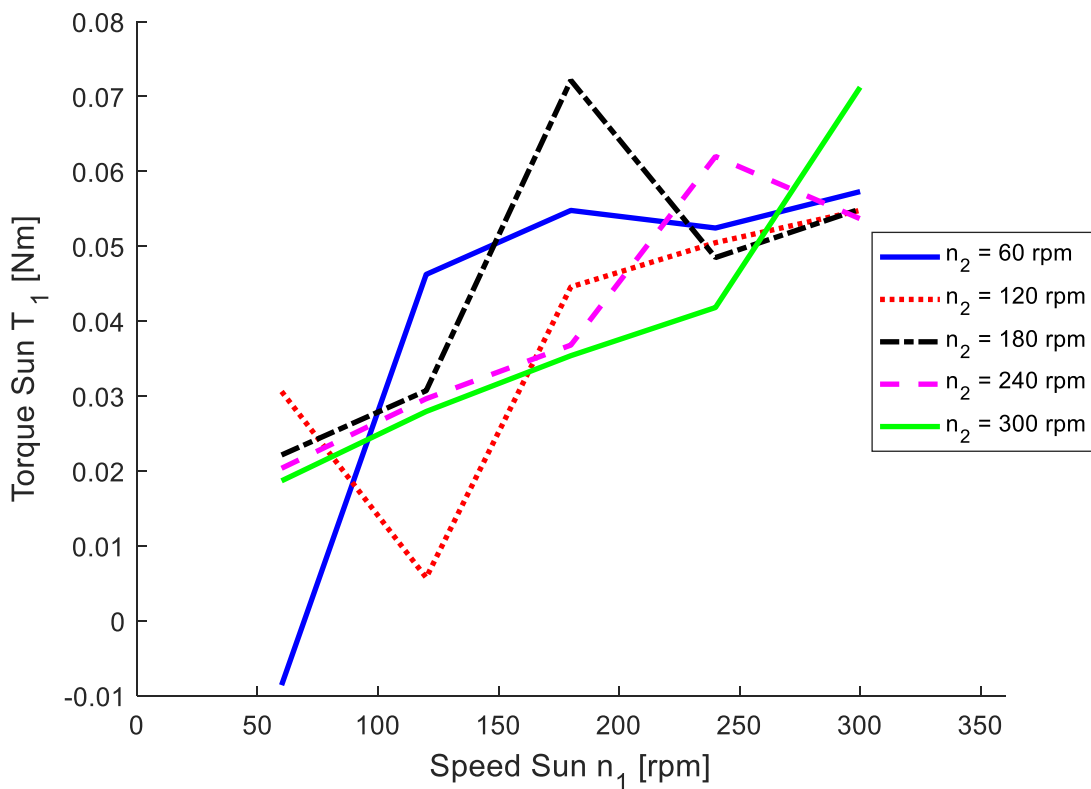


Figure 3.45 – Torque loss values in the sun side load cell, descent confirming data.

The graphs from the ring side show the same results (Figure 3.46, Figure 3.47).

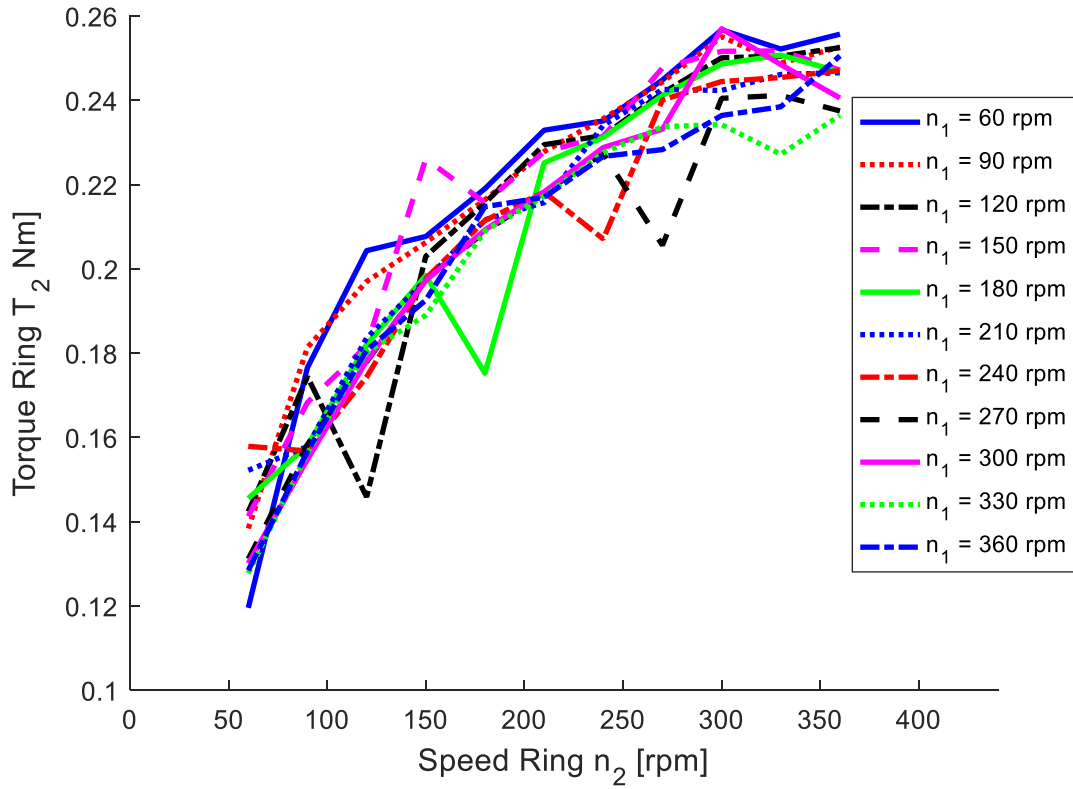


Figure 3.46 – Torque loss values in the ring side load cell, ascent principal data.

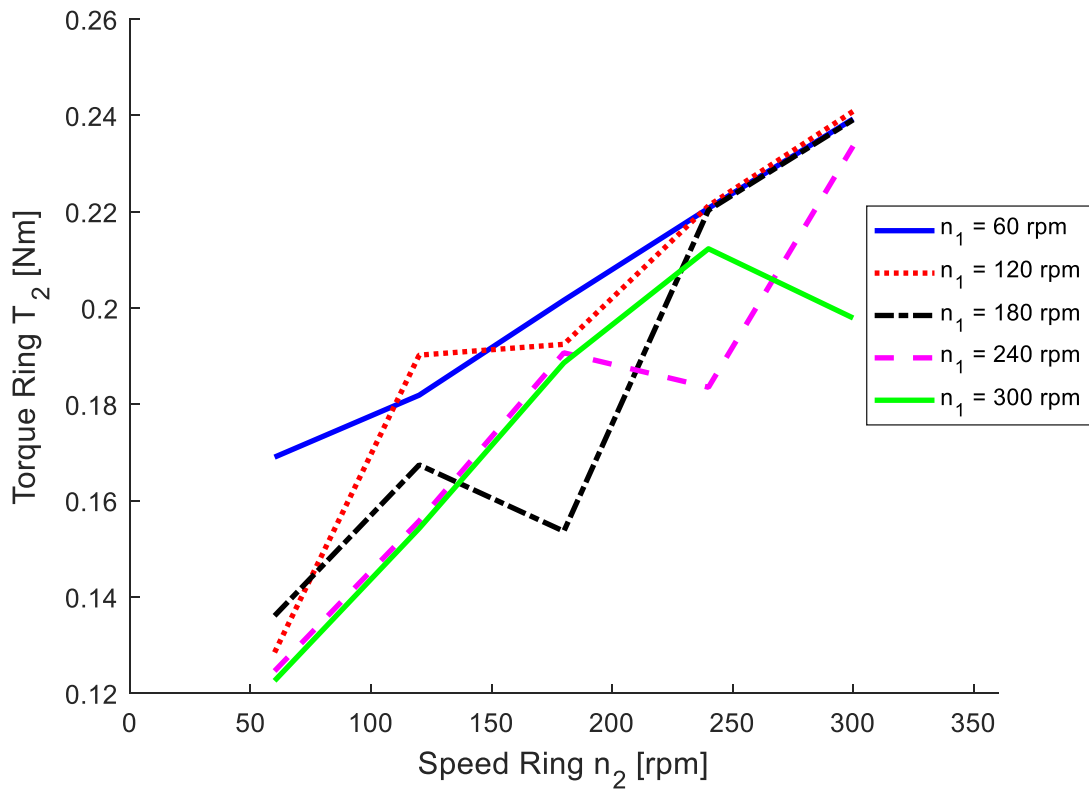


Figure 3.47 – Torque loss values in the ring side load cell, descent confirming data.

It is possible to witness two peculiar behaviours from these old data already: the torque lost diminishes with an increase in the opposite side speed, for both sun and ring, and undergoes sudden jumps that break the main trend when the two speeds are equal.

3.3.2.4 Interpolation

A visual representation of the reason for the dismissal of the old 11x11 matrix data is shown in Figure 3.48 and Figure 3.49. The interest zone goes way past the experimental range and, being polyAlphaLMS the function used, the level of precision lost is not bearable.

Plus, as will be shown in the next section, the very data for the ring shaft undergoes a change in tendency that would be impossible to witness with these values.

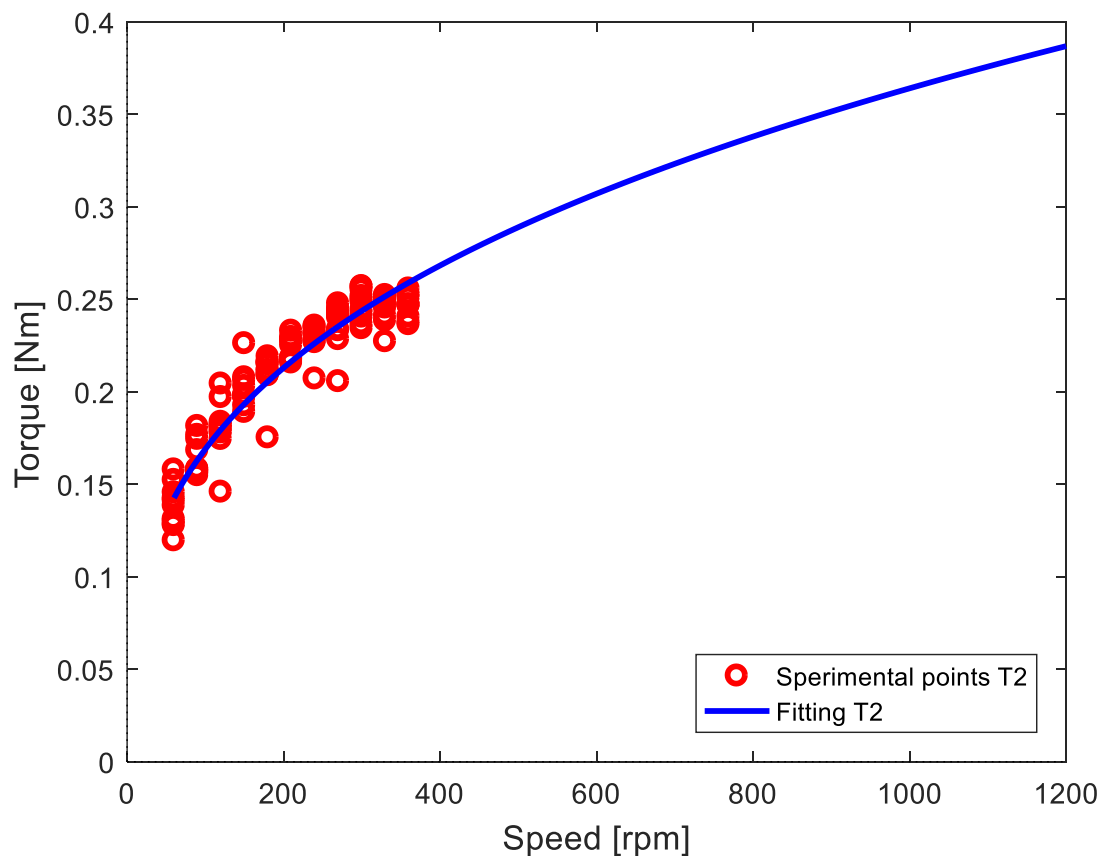


Figure 3.48 – Curve fitting for ring torque, old data.

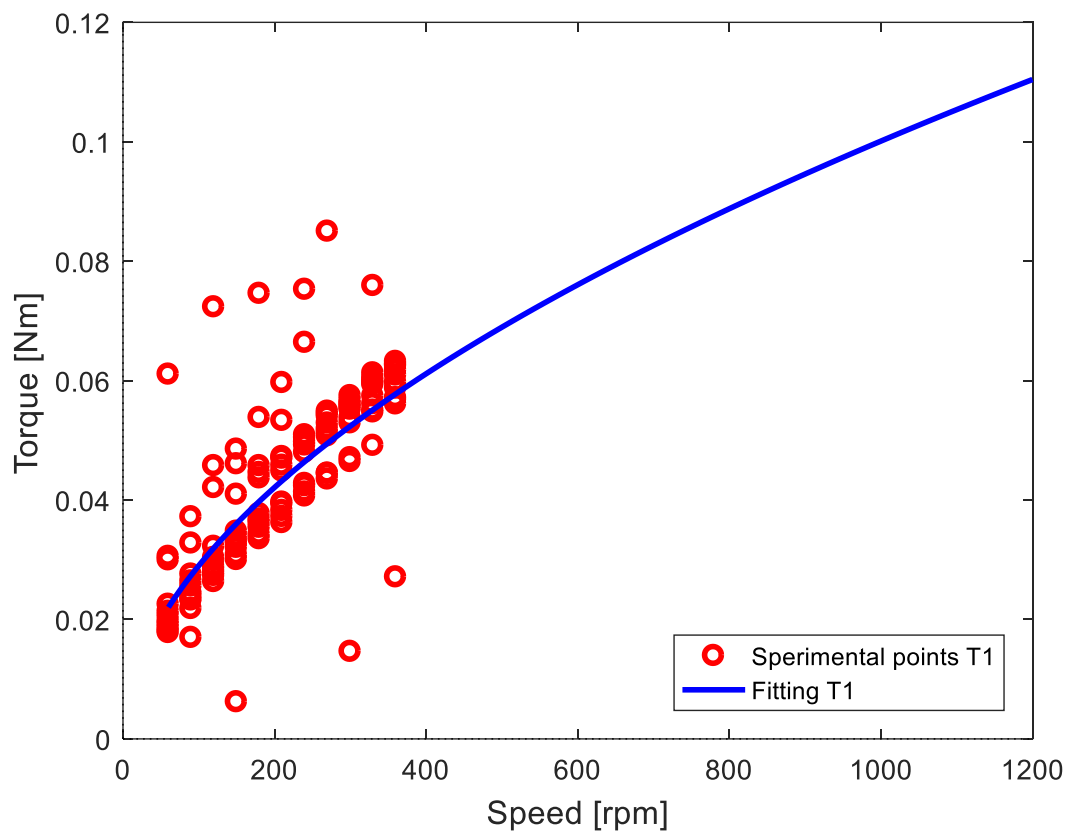


Figure 3.49 – Curve fitting for sun torque, old data.

3.3.3 New data

3.3.3.1 Acquisitions

Since the previous data hasn't shown a good coverage of working values of speed through extrapolation, a second set of points has been used to perform other experiments which cover all the range of speeds for both the first and the second gear in the sun and the ring. Therefore, on the sun side the tests start from 60 rpm, passing by 90 and 120 rpm just to increase the total volume of data, only to then reach 156 rpm and, from there on, increasing with steps of 60 multiplied by the first gear ratio, going up to 1872, the maximum speed in the engaged tests on the sun side. In this way the points for the second gear can easily be obtained by interpolation inside the experimental range. On the ring side the points go from 60 rpm to 720 rpm with a step of 60 rpm. The final matrix of all possible combination is a 15x12 grid for a total of 180 points.

Also in this case the two shafts are made to rotate in the same direction for the reason explained in §3.2.1.

The tests were performed at 1 kHz of sampling frequency.

3.3.3.2 Signals filtering

The filtering is the same described in §3.2.2.

3.3.3.3 Torque losses

The new trends are shown in Figure 3.50 and Figure 3.51 with regards to the sun side and in Figure 3.52 and Figure 3.53 for the ring side.

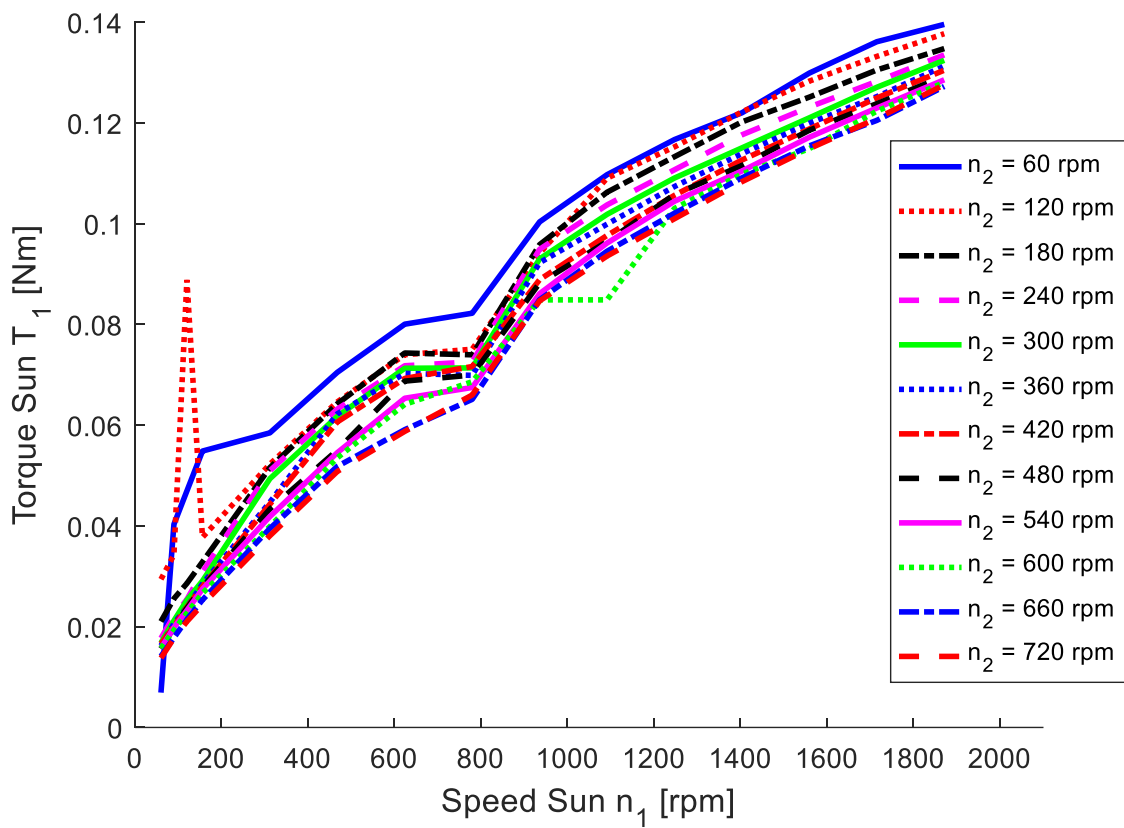


Figure 3.50 – Torque loss values in the sun side, 2D with dependence from sun speed.

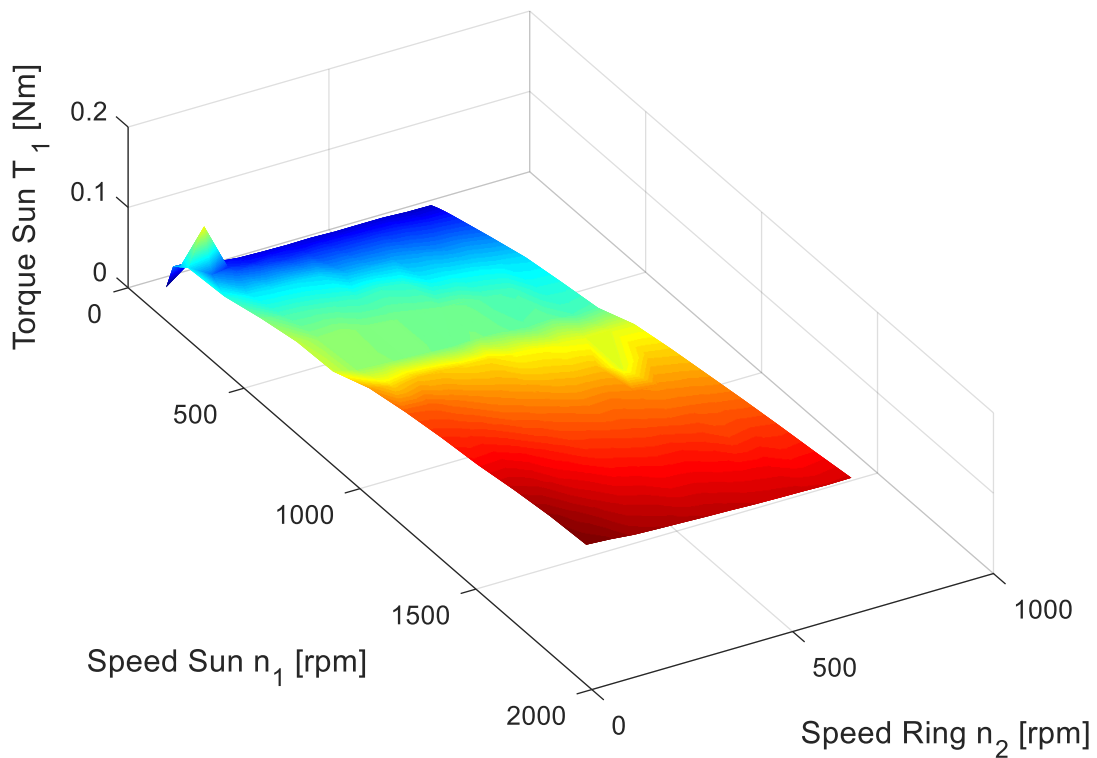


Figure 3.51 – Torque loss values in the sun side, 3D with dependence from sun and ring speed.

The trend is going up with the sun speed as expected, and in a quasi-linear way. There still is a descending trend concerning the increase of the ring speed that has been visualized in a better way via the 3D plot, in which a very limited dependence is presented, nevertheless. Since the grid of speeds has changed, the spike in torque at the same value of sun and ring speed doesn't occur anymore, except for two points (60-60 and 90-90). This is a less important aspect for the processing of data but a plus considering clarity of representation.

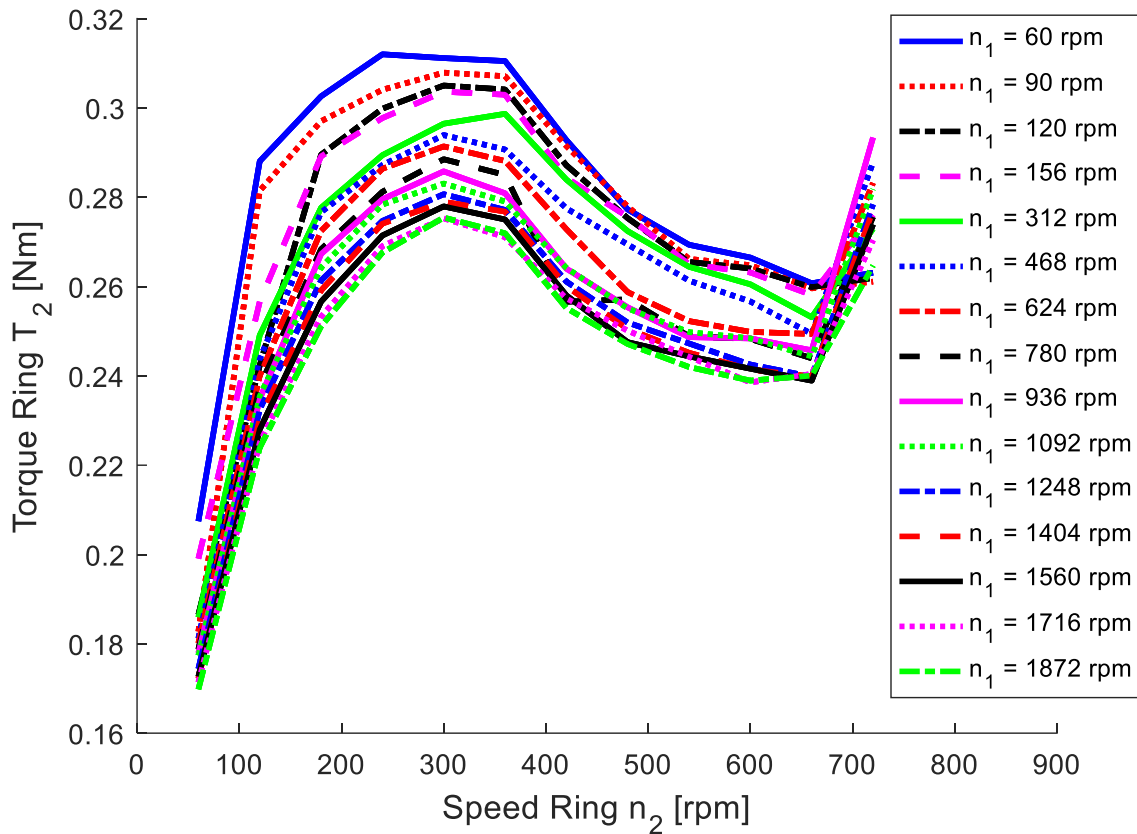


Figure 3.52 – Torque loss values in the ring side, 2D with dependence from ring speed.

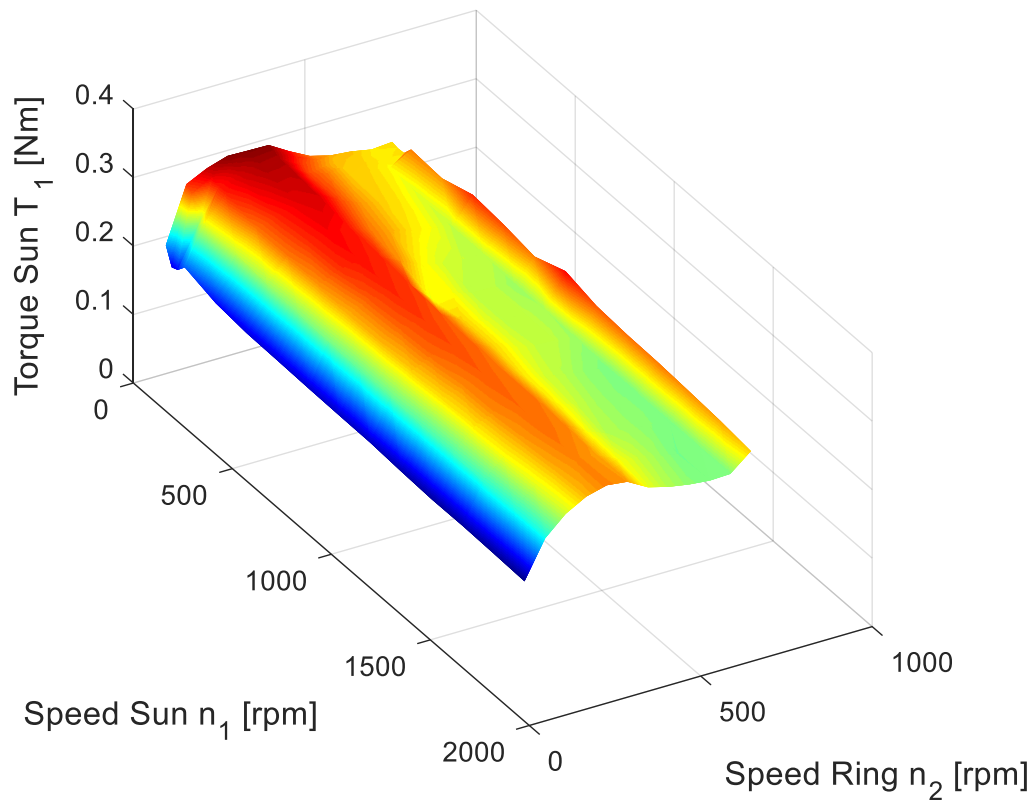


Figure 3.53 – Torque loss values in the ring side, 3D with dependence from sun and ring speed.

Here is presented a trend that with the former points couldn't be witnessed, since it begins just between 300 rpm and 400 rpm: the torque reaches a peak and then smoothly declines up until the 720 rpm mark, where a sudden spike is registered.

3.3.4 Curve fitting

The data is now interpolated again, but in this case there are two differences. First of all, the interpolation is limited inside the region of acquisition. Also, since the trend for the ring torque is not monotone, the polyLMS function has been used instead of polyAlphaLMS. In this scenario it is allowable for the interpolation to lose the real trend outside the experimental region because it is not needed there. A fourth grade polynomial has been used. For the sun torque the polyAlphaLMS function has been used because the trend remains monotone.

The results are shown in Figure 3.54 and Figure 3.55.

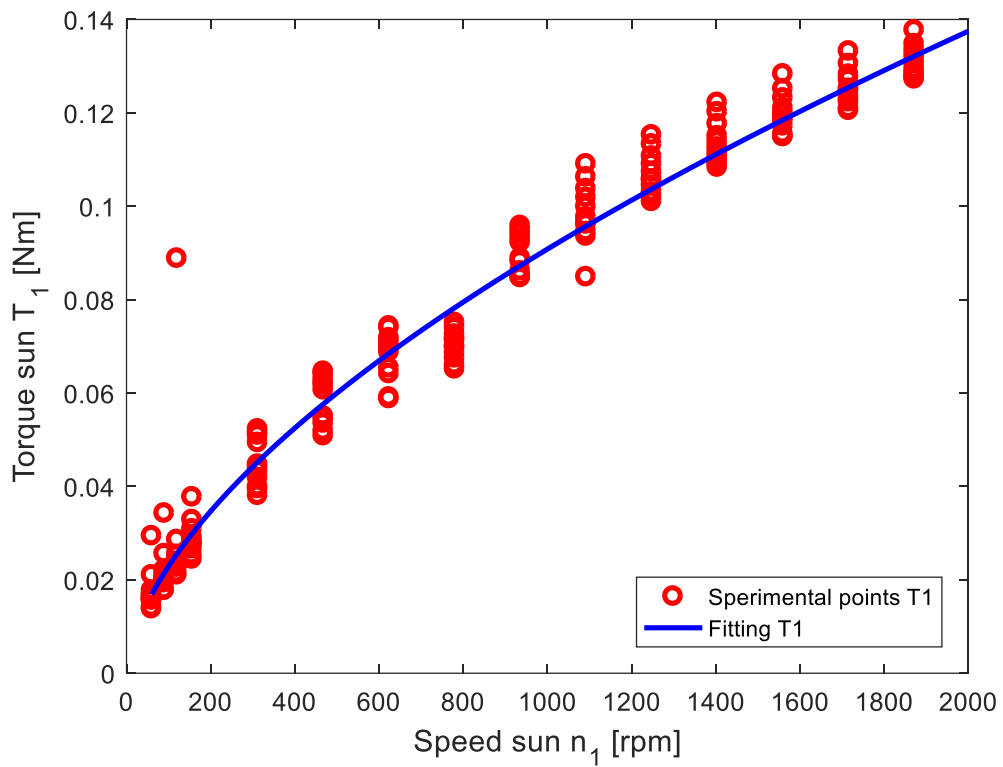


Figure 3.54 – Curve fitting for sun torque with polyAlphaLMS.

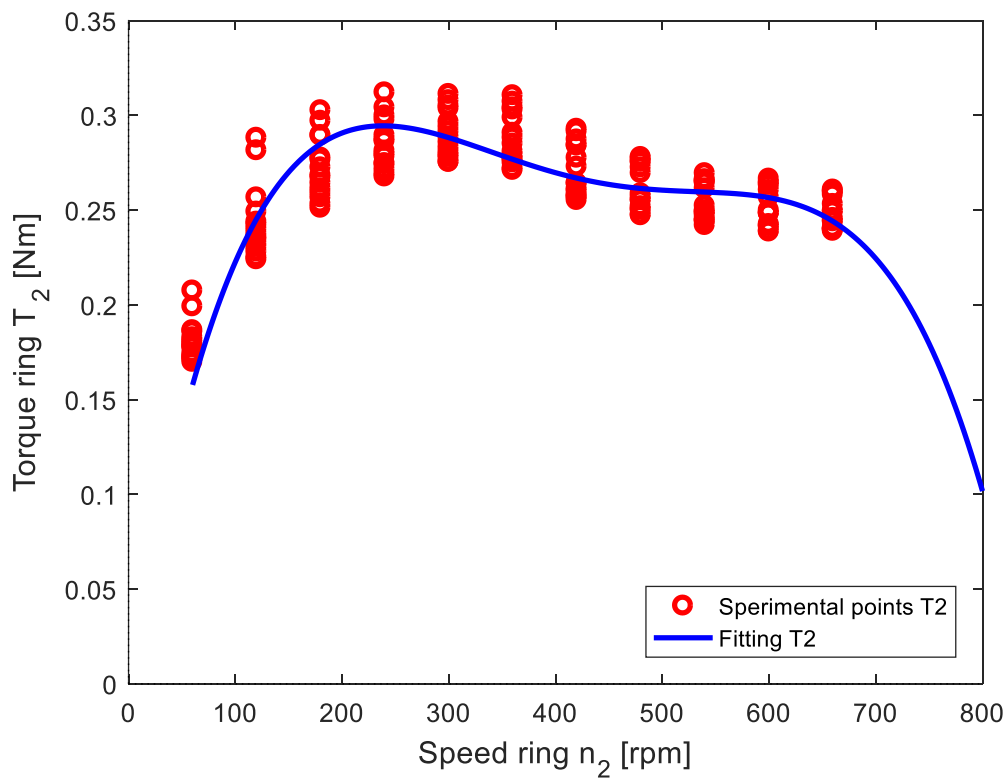


Figure 3.55 – Curve fitting for ring torque with polyLMS.

3.3.5 Alternative curve fitting

An alternative approach has been taken in order to get an analytical trend to adapt to the experimental points.

The concept comes from the consideration that a monotone trend can be reported as a function of the type

$$T_{loss} = Cn^\alpha \quad (3.7)$$

In this particular case however, since the ring torque has shown to vary in a non-trivial manner, this type of association results impracticable and relegated to the sun torque only.

To complete the formulation, since the ring speed also plays a role, it is sufficient to add a factor to the equation

$$T_1 = C_1 n_1^{\alpha_1} n_2^{\alpha_2} \quad (3.8)$$

to get a complete description.

The property of polynomial functions is the possibility to transform them through logarithms into sums. These sums can then be managed in a matrixial manner to obtain the coefficients through an inversion.

So, the new equation is

$$\ln T_1 = C_{1,0} + \alpha_1 x_1 + \alpha_2 x_2 \quad (3.9)$$

where:

$C_{1,0}$: natural logarithm of C_1 ;

x_1 : natural logarithm of n_1 ;

x_2 : natural logarithm of n_2 .

The matrix that contains all the data is then

$$\begin{Bmatrix} \ln T_{1,1} \\ \vdots \\ \ln T_{1,180} \end{Bmatrix} = \begin{bmatrix} 1 & n_{1,1} & n_{2,1} \\ \vdots & \vdots & \vdots \\ \vdots & n_{1,1} & n_{2,12} \\ \vdots & n_{1,2} & n_{2,1} \\ \vdots & \vdots & \vdots \\ \vdots & n_{1,2} & n_{2,12} \\ \vdots & \vdots & \vdots \\ \vdots & \vdots & \vdots \\ \vdots & \vdots & \vdots \\ \vdots & n_{1,15} & n_{2,1} \\ \vdots & \vdots & \vdots \\ 1 & n_{1,15} & n_{2,12} \end{bmatrix} \begin{Bmatrix} C_{1,0} \\ \alpha_1 \\ \alpha_2 \end{Bmatrix} \quad (3.10)$$

The torque vector is 180 points long since this is the total number of cases obtained from the tests.

From this, since the matrixes are not symmetrical, the only way to get the values of the coefficients is to use the pseudoinverse of the speed matrix and multiply it by the torque matrix. By reversing the logarithms, it is eventually possible to obtain the new analytical values of torque, presented in Figure 3.56.

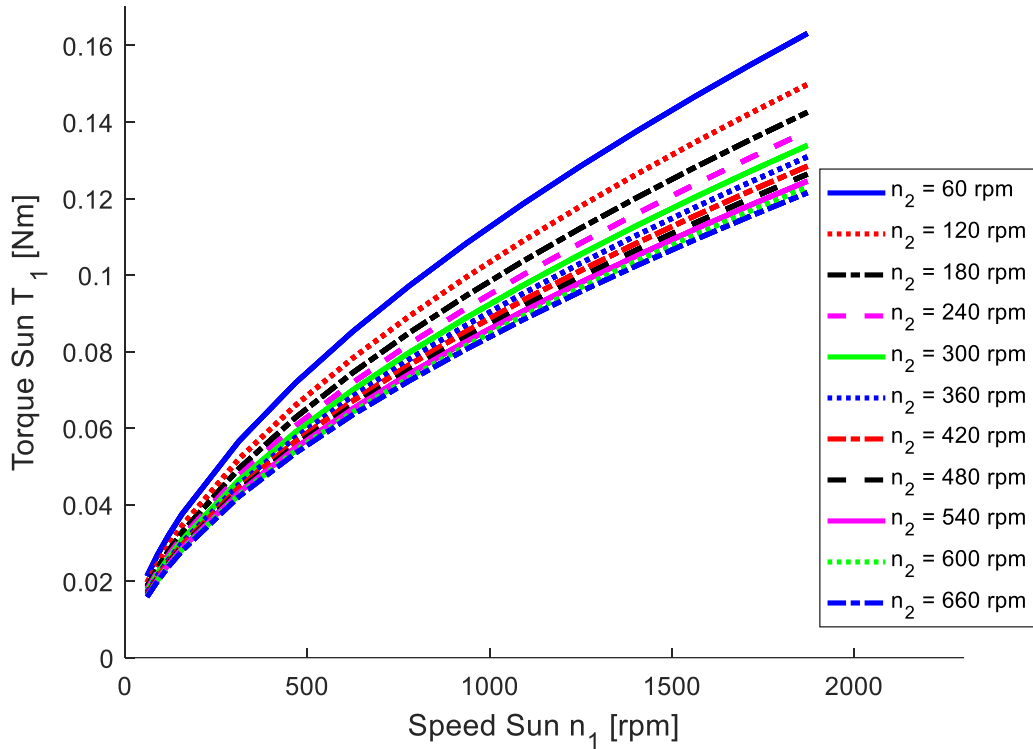


Figure 3.56 – Curve fitting for sun torque with pseudoinverse matrix.

If compared to the empirical points, it is clear that at low ring speeds the interpolation is not good, while it stabilizes at higher values (Figure 3.57). This can be due to the poor quality of the data itself at low speed, where the 60 rpm ring speed curve has a trend less precise than that of the other curves.

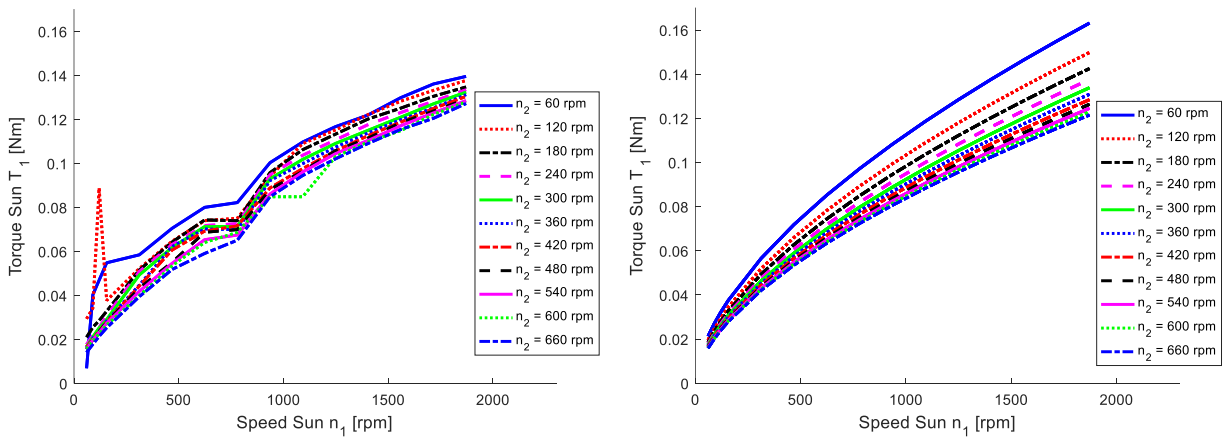


Figure 3.57 – Comparison between empirical (left) and fitted (right) sun torque.

3.3.6 Conclusions

The study showed that, as expected, the losses increase increasing the speed of the same side. However, the slight decrease assessed while increasing the speed on the opposite side has to be further investigated.

Moreover, the torque on the ring side has a non-monotone trend that makes its understanding difficult. This type of trend couldn't be spotted if the tests were to stop at the 360 rpm mark as the old grid does.

Chapter 4

4. Efficiency contributions

In this chapter, the combination of the data from the engaged tests and the neutral tests is put together.

The idea is to treat the neutral values as if they were mechanical loss values to insert into the efficiency equations.

While the first strategy was to use standardized data from the SKF tool to derive loss contributions from the rolling bearings, we can now rely on empirical data from the test bench. Having both sun and ring side torque data allows to combine them in a total power loss value.

The aim in this section, as stated in §2.3.2, is to see if, once the SKF path was abandoned, the new method can provide with realistic values of efficiency.

4.1 Efficiencies using neutral tests

The new case of study with the neutral tests has the potential to let us see if the previous method is actually fallacious and to be replaced.

The power lost in the bearings is calculated as follows:

$$P_{LOSS,B} = T_{1,N}\omega_{1,N} + T_{2,N}\omega_{2,N} \quad (4.1)$$

where $T_{1,N}$ and $T_{2,N}$ are respectively the lost torque measured on the sun side and on the ring side.

It is key to remind that the values of torque on the ring side are interpolated from the empirical data, but thanks to the new grid of chosen points these interpolations are all done inside the said empirical range.

The formulas with the newly calculated mechanical loss for the mechanical efficiency (eq (4.2)) and the magnetic efficiency (eq (4.3)) are displayed as follows:

$$\eta_B = \frac{P_{IN} - P_{LOSS,B}}{P_{IN}} \quad (4.2)$$

$$\eta_M = \frac{P_{OUT}}{P_{IN} - P_{LOSS,B}} \quad (4.3)$$

In a first time, in order to obtain reliable results, two interventions on the original data have been made. Firstly, all values at a ring speed of 720 rpm for the treatment of the ring torque have been removed because of the sudden rise in torque. Secondly, all values at a ring speed of 60 rpm for the treatment on the sun torque have been removed because they have an unsteady trend that differs from all the other speeds. From this, new tendency lines using the same methods as in §3.4 have been applied.

These interventions, however, were not enough: provided that the values of mechanical and magnetic gear have successfully been reversed, with the first now being less than the second, some values of magnetic gear were not acceptable.

The next step, then, has been to focus on the empirical data only, and to take the trends for both ring and sun torque with the lower values.

The results, in this case, satisfy the requests for this aim of the project. In the following chapters the final, correct results are displayed.

4.1.2 Mechanical efficiency

Following the chronological order of acquisitions, the graphs and the tables with the respective numerical values are presented.

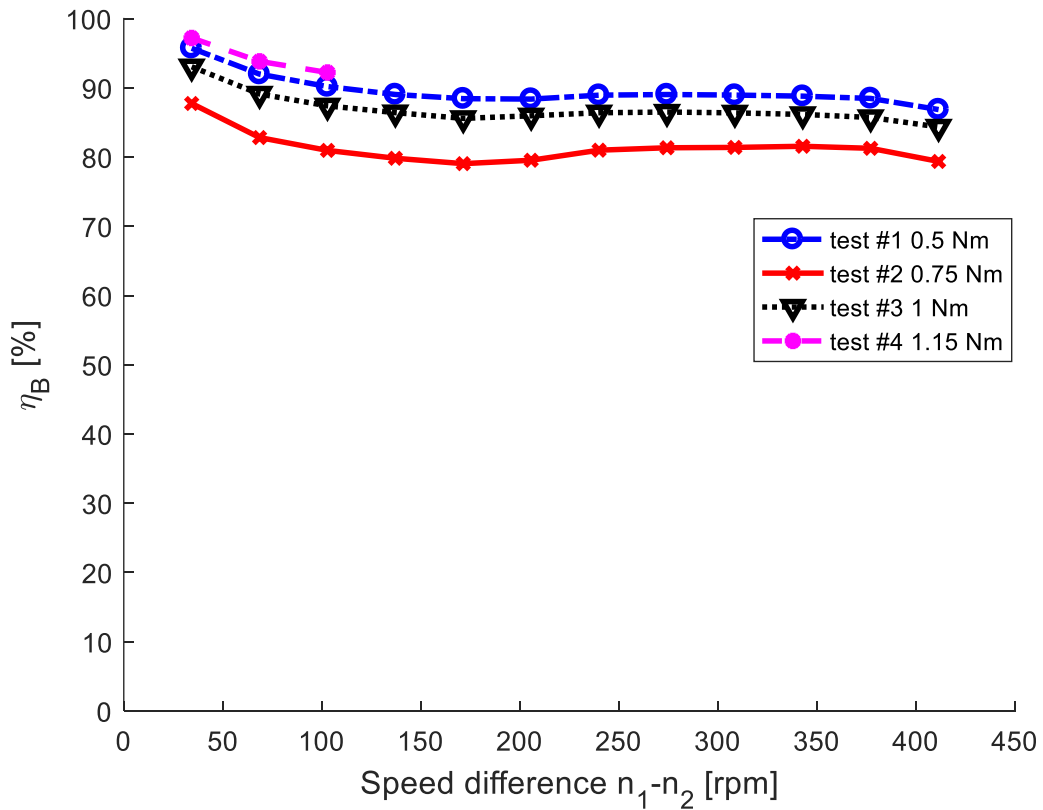


Figure 4.1 – mechanical efficiency plot, 2nd gear multiplier corrected values.

Table 4.1 – Mechanical efficiency values for $T_1=0,5$ Nm, 2nd gear multiplier.

Input speed ω_2 [rpm]	Efficiency η [%]
60	95.71
120	91.97
180	90.18
240	89.03
300	88.43
360	88.37
420	88.94
480	89.03
540	88.95

600	88.79
660	88.46
720	86.86

Table 4.2 – Mechanical efficiency values for $T_1=0,75$ Nm, 2nd gear multiplier.

Input speed ω_2 [rpm]	Efficiency η [%]
60	87.73
120	82.81
180	80.96
240	79.82
300	79.04
360	79.53
420	80.99
480	81.34
540	81.39
600	81.56
660	81.26
720	79.36

Table 4.3 – Mechanical efficiency values for $T_1=1$ Nm, 2nd gear multiplier.

Input speed ω_2 [rpm]	Efficiency η [%]
60	93.04
120	89.11
180	87.39
240	86.41
300	85.58
360	85.96
420	86.39
480	86.50
540	86.38
600	86.16
660	85.72
720	84.34

Table 4.4 – Mechanical efficiency for $T_1=1,15$ Nm, 2nd gear multiplier.

Input speed ω_2 [rpm]	Efficiency η [%]
60	97.19
120	93.82
180	92.21

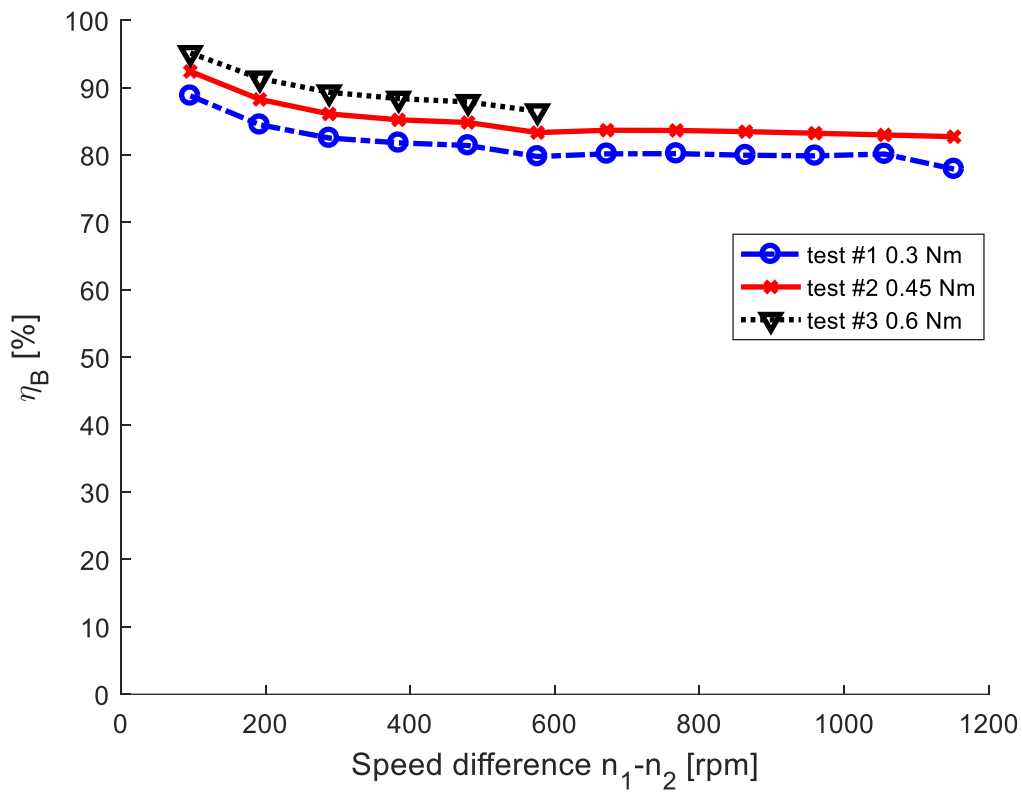


Figure 4.2 – mechanical efficiency plot, 1st gear multiplier corrected values.

Table 4.5 – Mechanical efficiency values for $T_1=0.3$ Nm, 1st gear multiplier.

Input speed ω_2 [rpm]	Efficiency η [%]
60	88.77
120	84.48
180	82.51
240	81.80
300	81,40
360	79.77
420	80.16
480	80.20
540	79.96
600	79.86
660	80.14
720	77.90

Table 4.6 – Mechanical efficiency values for $T_1=0.45$ Nm, 1st gear multiplier.

Input speed ω_2 [rpm]	Efficiency η [%]
60	92.38
120	88.24
180	86.09
240	85.21
300	84.81
360	83.32
420	83.66
480	83.64
540	83.45i
600	83.23
660	82.97
720	82.71

Table 4.7 – Mechanical efficiency values for $T_1=0.6$ Nm, 1st gear multiplier.

Input speed ω_2 [rpm]	Efficiency η [%]
60	95.13
120	91.35
180	89.30
240	88.36
300	87.87
360	86.48

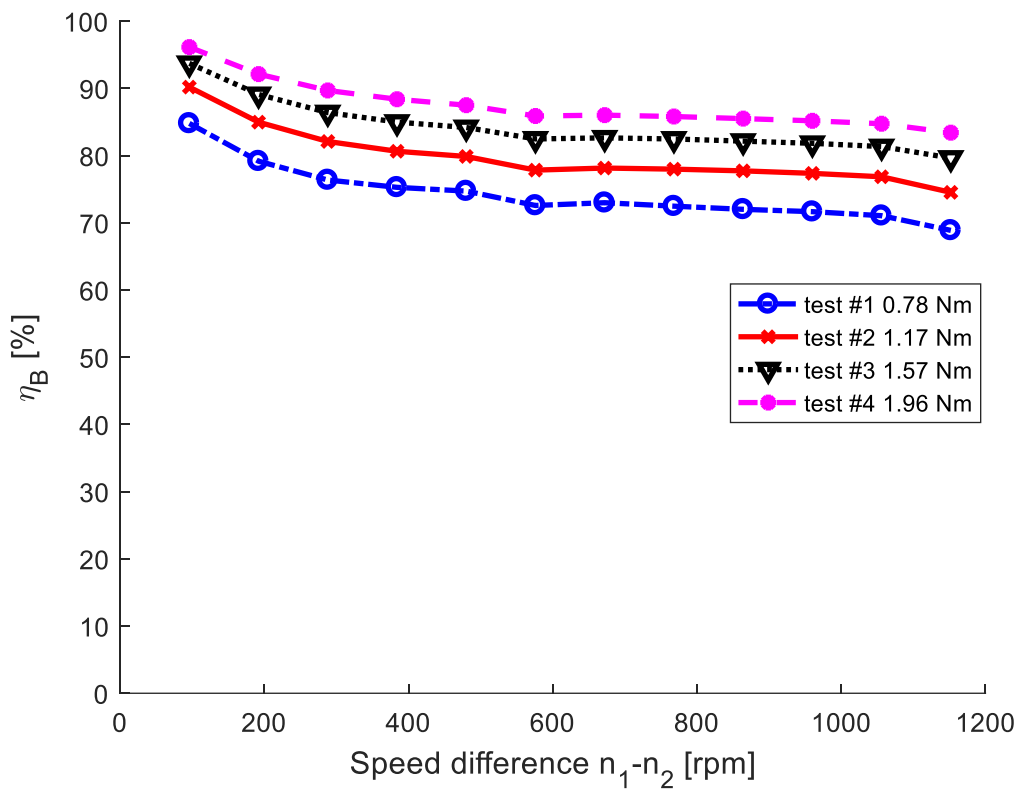


Figure 4.3 – mechanical efficiency plot, 1st gear reducer corrected values.

Table 4.8 – Mechanical efficiency values for $T_2=0.78$ Nm, 1st gear reducer.

Output speed ω_2 [rpm]	Efficiency η [%]
60	84.78
120	79.16
180	76.36
240	75.27
300	74.71
360	72.57
420	72.98
480	72.47
540	72.00
600	71.65
660	71.05
720	68.87

Table 4.9 – Mechanical efficiency values for $T_2=1.17$ Nm, 1st gear reducer.

Output speed ω_2 [rpm]	Efficiency η [%]
60	90.18
120	84.97
180	82.09
240	80.64
300	79.86
360	77.83
420	78.14
480	77.98
540	77.72
600	77.35
660	76.84
720	74.52

Table 4.10 – Mechanical efficiency values for $T_2=1.57$ Nm, 1st gear reducer.

Output speed ω_2 [rpm]	Efficiency η [%]
60	93.72
120	89.09
180	86.39
240	84.98
300	84.18
360	82.47
420	82.63
480	82.46
540	82.14
600	81.82
660	81.33
720	79.63

Table 4.11 – Mechanical efficiency values for $T_2=1.96$ Nm, 1st gear reducer.

Output speed ω_2 [rpm]	Efficiency η [%]
60	96.13
120	92.12
180	89.68
240	88.38
300	87.49
360	85.88
420	86.01
480	85.81
540	85.49
600	85.17
660	84.73
720	83.40

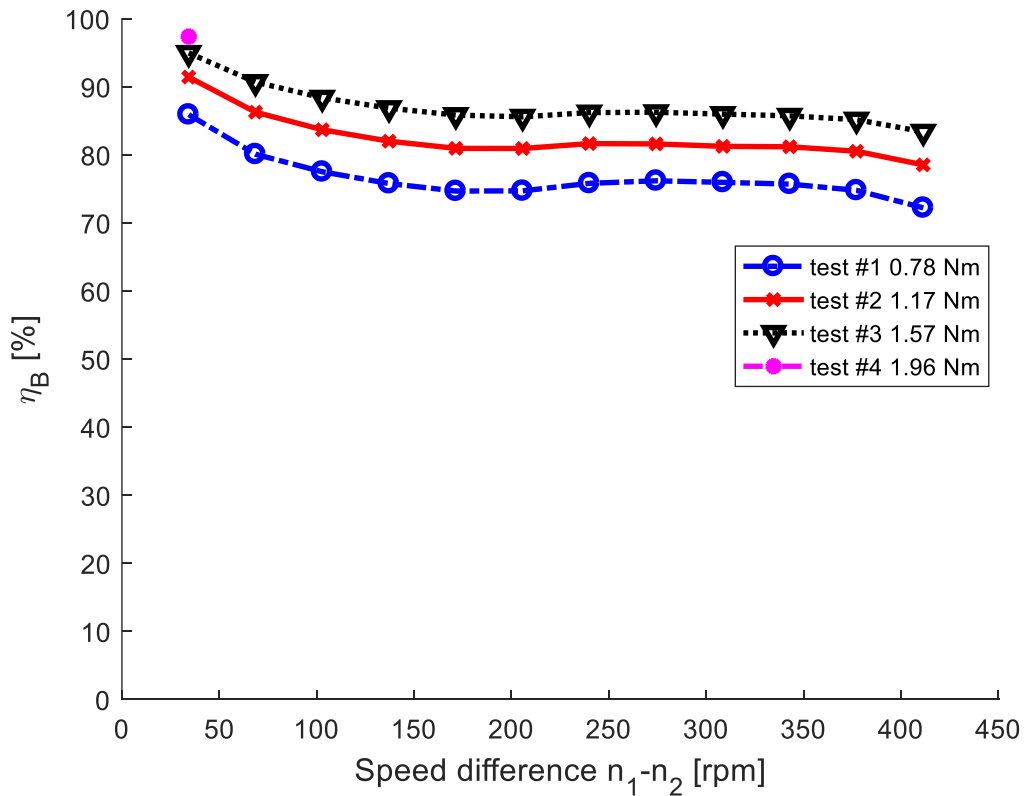


Figure 4.4 – mechanical efficiency plot, 2nd gear reducer corrected values.

Table 4.12 – Mechanical efficiency values for $T_2=0,78$ Nm, 2nd gear reducer.

Output speed ω_2 [rpm]	Efficiency η [%]
60	85.89
120	80.07
180	77.50
240	75.77
300	74.66
360	74.69
420	75.80
480	76.17
540	75.94
600	75.69
660	74.77
720	72.20

Table 4.13 – Mechanical efficiency values for $T_2=1,17$ Nm, 2nd gear reducer.

Output speed ω_2 [rpm]	Efficiency η [%]
60	91.40
120	86.26
180	83.67
240	81.99
300	80.93
360	80.92
420	81.64
480	81.59
540	81.23
600	81.17
660	80.51
720	78.51

Table 4.14 – Mechanical efficiency values for $T_2=1,57$ Nm, 2nd gear reducer.

Output speed ω_2 [rpm]	Efficiency η [%]
60	94.95
120	90.67
180	88.36
240	86.84
300	85.82
360	85.57
420	86.19
480	86.24
540	85.97
600	85.71
660	85.15
720	83.37

Table 4.15 – Mechanical efficiency values for $T_2=1,96$ Nm, 2nd gear reducer.

Output speed ω_2 [rpm]	Efficiency η [%]
60	97.36

These graphs show that not only the values are now lower, but that the empirical trend of the ring side torques impacts the trend lines for the efficiency, leaving a wave form.

4.1.3 Magnetic efficiency

Following the chronological order of tests for the representation of magnetic efficiencies too, the results are presented as follows.

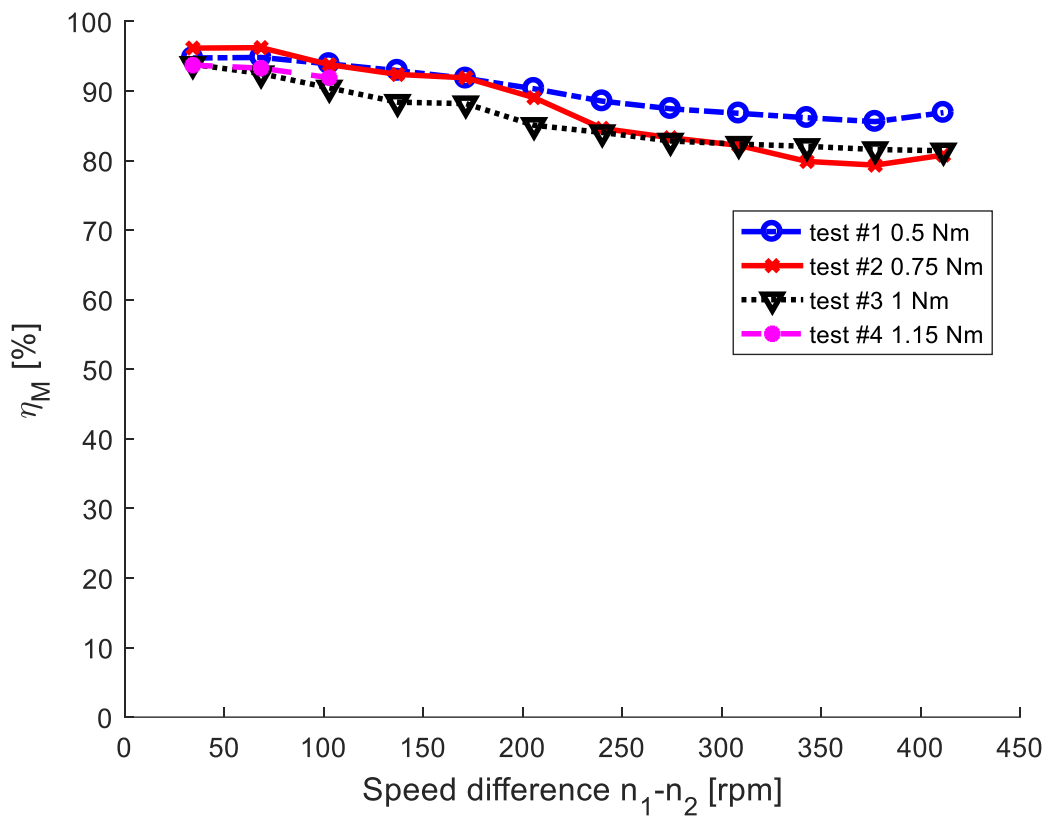


Figure 4.5 – Magnetic efficiency plot, 2nd gear multiplier corrected values.

Table 4.16 – Magnetic efficiency values for $T_1=0,5$ Nm, 2nd gear multiplier.

Input speed ω_2 [rpm]	Efficiency η [%]
60	94.73
120	94.81
180	93.88
240	92.92
300	91.80
360	90.31
420	88.53
480	87.44
540	86.78
600	86.15
660	85.59
720	86.88

Table 4.17 – Magnetic efficiency values for $T_1=0,75$ Nm, 2nd gear multiplier.

Input speed ω_2 [rpm]	Efficiency η [%]
60	96.16
120	96.22
180	93.78
240	92.37
300	91.89
360	89.03
420	84.61
480	83.27
540	82.17
600	79.87
660	79.33
720	80.78

Table 4.18 – Magnetic efficiency values for $T_1=1$ Nm, 2nd gear multiplier.

Input speed ω_2 [rpm]	Efficiency η [%]
60	93.83
120	92.49
180	90.44
240	88.38
300	88.18
360	85.06
420	84.02
480	82.81
540	82.36
600	82.04
660	81.58
720	81.40

Table 4.19 – Magnetic efficiency values for $T_1=1,15$ Nm, 2nd gear multiplier.

Input speed ω_2 [rpm]	Efficiency η [%]
60	93.70
120	93.28
180	91.90

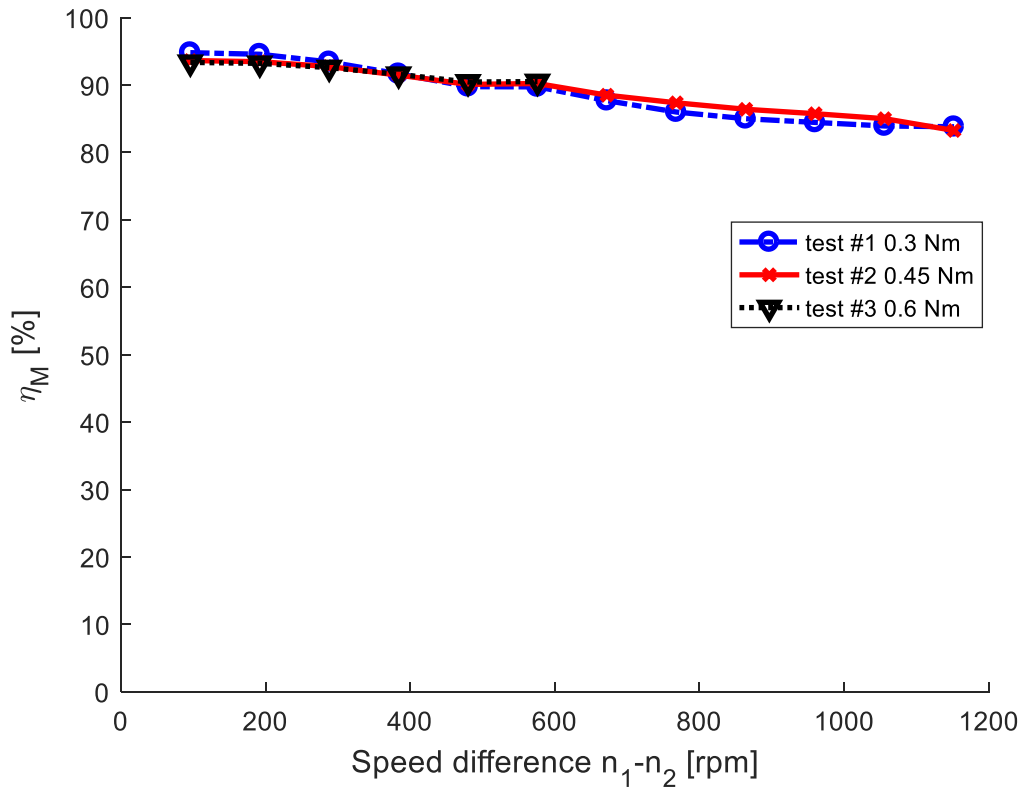


Figure 4.6 – Magnetic efficiency plot, 1st gear multiplier corrected values.

Table 4.20 – Magnetic efficiency values for $T_1=0.3$ Nm, 1st gear multiplier.

Input speed ω_2 [rpm]	Efficiency η [%]
60	94.79
120	94.56
180	93.42
240	91.65
300	89.75
360	89.72
420	87.67
480	85.99
540	85.00
600	84.45
660	83.92
720	83.81

Table 4.21 – Magnetic efficiency values for $T_1=0.45$ Nm, 1st gear multiplier.

Input speed ω_2 [rpm]	Efficiency η [%]
60	93.60
120	93.45
180	92.73
240	91.46
300	90.08
360	90.22
420	88.49
480	87.36
540	86.40
600	85.74
660	85.00
720	83.25

Table 4.22 – Magnetic efficiency values for $T_1=0.6$ Nm, 1st gear multiplier.

Input speed ω_2 [rpm]	Efficiency η [%]
60	93.35
120	93.21
180	92.57
240	91.58
300	90.45
360	90.50

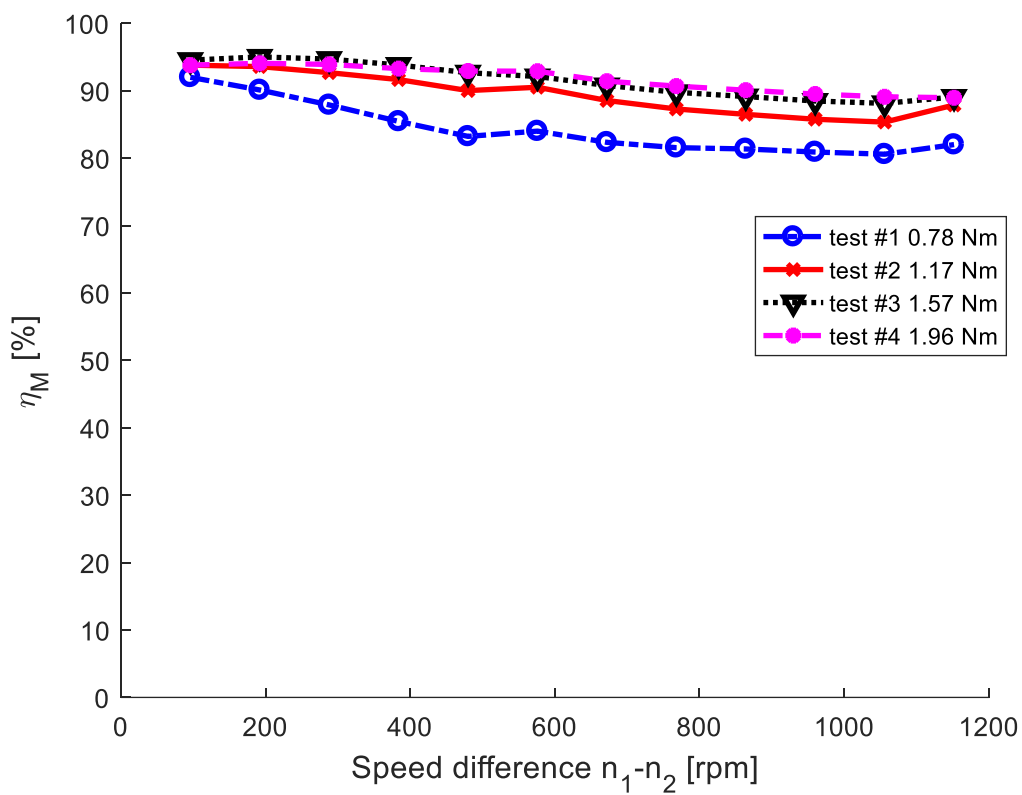


Figure 4.7 – Magnetic efficiency plot, 1st gear reducer corrected values.

Table 4.23 – Magnetic efficiency values for $T_2=0.78$ Nm, 1st gear reducer.

Output speed ω_2 [rpm]	Efficiency η [%]
60	91.98
120	90.10
180	87.88
240	85.44
300	83.22
360	84.00
420	82.33
480	81.54
540	81.35
600	80.90
660	80.57
720	82.00

Table 4.24 – Magnetic efficiency values for $T_2=1.17$ Nm, 1st gear reducer.

Output speed ω_2 [rpm]	Efficiency η [%]
60	93.78
120	93.57
180	92.67
240	91.64
300	90.01
360	90.50
420	88.54
480	87.28
540	86.48
600	85.76
660	85.33
720	87.87

Table 4.25 – Magnetic efficiency values for $T_2=1.57$ Nm, 1st gear reducer.

Output speed ω_2 [rpm]	Efficiency η [%]
60	94.53
120	95.01
180	94.68
240	93.81
300	92.66
360	92.10
420	90.76
480	89.76
540	89.12
600	88.47
660	88.12
720	89.06

Table 4.26 – Magnetic efficiency values for $T_2=1.96$ Nm, 1st gear reducer.

Output speed ω_2 [rpm]	Efficiency η [%]
60	93.77
120	94.06
180	93.89
240	93.27
300	92.91
360	92.88
420	91.40
480	90.68
540	90.07
600	89.50
660	89.09
720	88.95

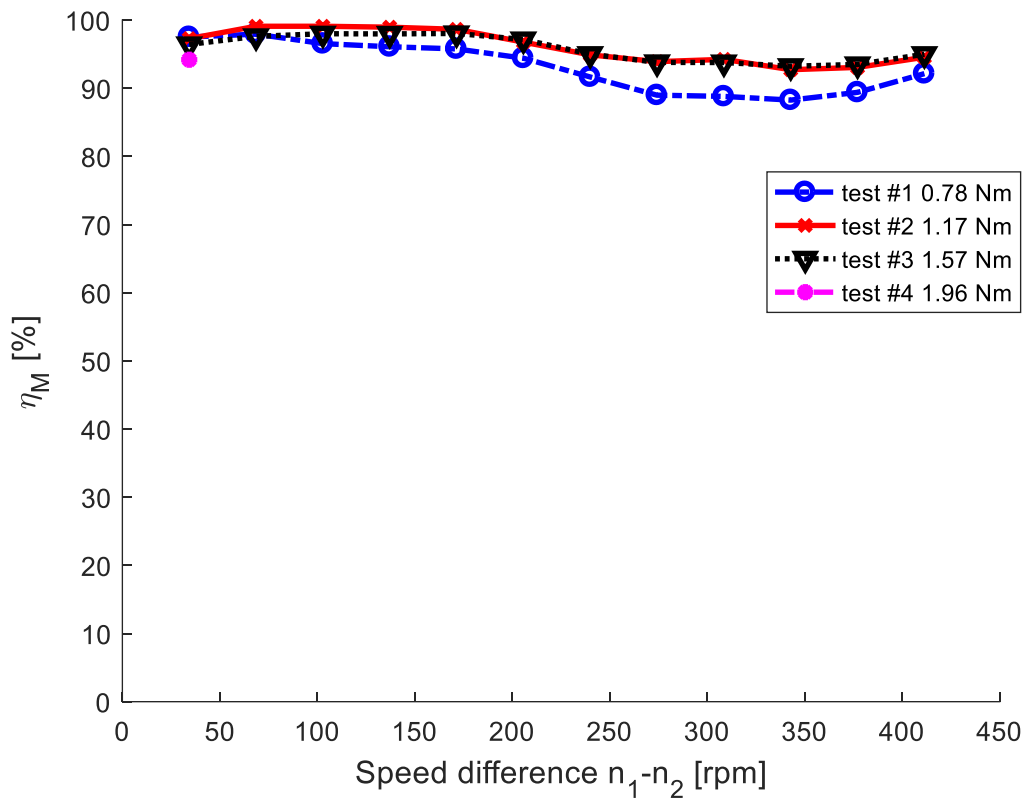


Figure 4.8 – Magnetic efficiency plot, 2nd gear reducer corrected values.

Table 4.27 – Magnetic efficiency values for $T_2=0,78$ Nm, 2nd gear reducer.

Output speed ω_2 [rpm]	Efficiency η [%]
60	97.50
120	97.92
180	96.53
240	96.08
300	95.76
360	94.40
420	91.64
480	88.97
540	88.79
600	88.25
660	89.39
720	92.13

Table 4.28 – Magnetic efficiency values for $T_2=1,17$ Nm, 2nd gear reducer.

Output speed ω_2 [rpm]	Efficiency η [%]
60	97.27
120	99.08
180	99.08
240	98.95
300	98.63
360	96.75
420	94.89
480	93.89
540	94.23
600	92.71
660	93.05
720	94.53

Table 4.29 – Magnetic efficiency values for $T_2=1,57$ Nm, 2nd gear reducer.

Output speed ω_2 [rpm]	Efficiency η [%]
60	96.42
120	97.60
180	97.98
240	97.96
300	98.03
360	97.14
420	94.99
480	93.78
540	93.76
600	93.22
660	93.48
720	94.98

Table 4.30 – Magnetic efficiency values for $T_2=1,96$ Nm, 2nd gear reducer.

Output speed ω_2 [rpm]	Efficiency η [%]
60	94.17

The new values are eventually significantly higher, consistently staying above 80% and in most cases even 90%. The wave form is still present but reversed compared to that of the mechanical efficiencies, since the total efficiency doesn't have significant curvatures.

4.2 Conclusions

The study showed that the combination of engaged and neutral tests using the latest 15x12 grid is better than the previous method of using the SKF tool, since the efficiency contributions relative weight on the total are reversed, with the magnetic contribution now being less impacting and more near 100% efficiency, provided that the best empirical data is used.

5. Final conclusions

Finally, to summarize the work performed on the PMG test bench and the results obtained, it is possible to start with a reminder of what a magnetic gear can accomplish.

The key points in using magnetic gears over the more conventional mechanical gears need to be found in the functioning differences: magnetic gears don't need physical contact to work and transfer torque and power and therefore there is a new safety aspect that can be useful for a variety of reasons, like the reduced maintenance need, lower risk of breakage or wear and the noise and vibration reduction. Also, since many major downsides have been solved throughout the years, such as the performance of materials and geometry, the confrontation can now be held on the same level. In this study, the specific performance in terms of power transmission and power loss are analysed in order to see what the most favourable conditions of operation for the specific PMG are tested and therefore for the whole category of magnetic gears, and to find out if there are significant flaws that can be corrected at an early prototyping phase.

Many different tests were conducted, covering every possible mode of functioning of the PMG in order to extract important data, since the evaluation of the particular contributions to the efficiency of the system is not an easy task to accomplish, and still restrains a certain dose of uncertainty due to the combination of different values.

Both positive aspects and critical issues have been addressed.

Going through the tests in order, the first good result comes from the comparison between the current bearings and the old ones via the no-load tests, that sees the new ones as giving the fewest losses overall, increasing the total efficiency.

The first challenge has been the behaviour of the torque at high speed in the initial phases of the descending tests, where it suddenly increases just to go back to the main trend after a couple speed stages.

Then, the loaded tests have shown that the efficiency of the system is as high as expected and the reduction when the speed increases was expected too.

An important point here is the slight increase in efficiency when the resistant torque is increased, for all speed points and for all four operation mode. This phenomenon can be attributed to the bearings behaviour: as expected, they don't get involved into outside torsional loads, as they would with an axial or radial load. This means that, holding the speed still, the dissipations through these elements are constant (maintaining all the boundary conditions such as environment factors fixed). Then, increasing the load makes the input torque increase as the sum of the resistant load and the constant dissipations, and therefore in a less than proportional way, making the efficiency fraction increase in value.

Passing on to neutral tests, the 15x12 grid data with extended speed examined has shed a light on the behaviour of the two sides: the sun side has a monotone and less than proportional trend for torque loss (just as the no-load tests), at least up to the 1872 rpm mark tested. The ring side has a trend that initially increases as the sun side trend, and then hits a maximum and smoothly declines towards a horizontal asymptote. This behaviour is not easy to interpret but it is most certainly due to magnetic effects.

Eventually, some important considerations can be made regarding the final results coming from the combination of the main tests performed.

The partitioning of the mechanical and magnetic contribution of the losses that occur, and therefore to the efficiency of the system, eventually reaches the right balance, with the magnetic losses being overall the lowest of the two. This is due to the fact that the prototype has an extremely thin portion occupied by the magnetically active components compared to the mechanical elements that are the bearings.

The numerical values have been derived from the best performing experimental curves for the neutral tests for both the sun and the ring side.

The final results can be accepted, keeping in mind the initial suppositions for the neutral tests stating that the involvement of mechanical contributions only takes place.

The consideration for future updates and corrections are many: first of all, a thermal evaluation during tests under different conditions and for prolonged times can be important for a deeper understanding of the behaviour of the bearings in particular. Then, for the neutral tests, a wider set of data for the sun side to see if, at higher speeds, the same behavioural pattern witnessed for the ring applies. Also, the assumption of non-interference of magnetic effects on the neutral tests needs to be revisited, since to be really mechanically driven only, a good isolation from magnetic influxes through the carrier could be evaluated, as much as a wider space between the two gears. This last step would involve the opening of the prototype and a work on the components.

Eventually, in order to increase the performance of the prototype and to get near the torques formulated in the FEM model and to avoid the slipping occurred, the length of the PMs could be increased.

Reference

- [1] Esnoz-Larraya J., Valiente-Blanco I., Cristache C., Sanchez-Garcia-Casarrubios J., Rodriguez-Celis F., Diez-Jimenez E., Perez-Diaz J, OPTIMAGDRIVE: HIGH-PERFORMANCE MAGNETIC GEARS DEVELOPED FOR SPACE APPLICATIONS, ESA.
- [2] McGilton B., Crozier R., McDonald A., Mueller M., Review of magnetic gear technologies and their applications in marine energy, IET Renewable Power Generation, Vol. 12 Iss. 2, 2018.
- [3] Desvaux M., Le Goff Latimier R., Multon B., Ben Ahmed H., Sire S., Design and Optimization of Magnetic Gears with Arrangement and Mechanical Constraints for Wind Turbine Applications, hal-01312302, EVER'16, April 2016.
- [4] Tlali P.M., Wang R-J., Gerber S., Magnetic Gear Technologies: A Review, IEEE, 2014, pp. 544.
- [5] Barnouin R., Genta G., Magnetic Gears, Description and Application for Car Industry, Politecnico of Turin, 2016, pp. 11.
- [6] Uppapalati K. K., Bomela W., Bird J. Z., Calvin M., Wright J., Construction of Low Speed Flux Focusing Magnetic Gear, Laboratory of Electromagnetic Energy Conversion and Control, Department of Electrical and Computer Engineering, University of North Carolina at Charlotte, NC, USA, 2013.
- [7] Barnouin R., Genta G., Magnetic Gears, Description and Application for Car Industry, Politecnico of Turin, 2016, pp. 33-34.
- [8] Al-Qarni A. H., Wu F., El-Refaie A. M., High-Torque-Density Low-Cost Magnetic Gear Utilizing Hybrid Magnets and Advanced Materials, IEEE International Electric Machines & Drives Conference (IEMDC), 2019.
- [9] Al-Qarni A. H., El-Refaie A. Magnetic Gears and Magnetically Geared Machines with Reduced Rare-Earth Elements for Vehicle Applications, World Electric Vehicles Journal, 2021.
- [10] Hetzel M., Low friction miniature gear drive for transmitting small forces, and method of making same, US Patent 3 792 578, 1974.
- [11] Mabe W. J., Magnetic transmission, US Patent 5 013 949, 1991.
- [12] Kikuchi S., Tsurumoto K., Design and characteristics of a new magnetic worm gear using permanent magnets, IEEE Transactions on Magnetics, Vol. 29, No6, 1933, pp. 2923-2925.
- [13] Yao Y., Huang D. R., Hsieh C. C., Chiang D. Y., Wang S. J., Ying T. F., The radial magnetic coupling studies of perpendicular magnetic gears, IEEE Transactions on Magnetics, Vol. 32, No 5., 1996, pp. 5061-5063.
- [14] Atallah K., Howe D., A Novel High-Performance Magnetic Gear, IEEE TRANSACTIONS ON MAGNETICS, VOL. 37, NO 4, 2001, pp. 2844.
- [15] Neves C. G. C., Goettens M. F., Flores Filho A. F., Construction of a Coaxial Magnetic Gear, CENG/Universidade Federal de Pelotas, 2017 , pp. 1.
- [16] Miladinovic S., Ivanovic L., Blagojevic M., Stojanovic B., THE DEVELOPMENT OF MAGNETIC GEARS FOR TRANSPORTATION APPLICATIONS, Mobility & Vehicle Mechanics, Volume 43, Number 1, 2017, pp. 42.
- [17] Uppapalati K. K., Kadel J., Wright J., Li K., Williams W., Bird J., A Low Assembly Cost Coaxial Magnetic Gearbox, Electrical and Computer Engineering Faculty Publications and Presentations, 2017.
- [18] Desvaux M., Multon B., H.B. Ahmed, Sire S., Behaviour comparison between mechanical epicyclic gears and magnetic gears, Multibody Mechatronic Systems, 54, Mechanism and Machine Science, <10.1007/978-3-319-67567-1_38>. <hal-01629812>, 2017 , pp. 401-410.

- [19] Kowol M, Kołodziej J., Lukaniszyn M., An analysis of magnetic gear performance, Faculty of Electrical Engineering, Automatic Control and Informatics, Opole University of Technology, 2015, pp. 88.
- [20] Halim M. F. M. A., Sulaiman E., Jenal M., Othman R. N. F. K. R., Buried PM inner rotor magnetic gear evaluation, IOP Conference Series: Materials Science and Engineering 917 012002, 2020.
- [21] Atallah K., Howe D., S.D. Calverley, Design, analysis and realisation of a high-performance magnetic gear, IEE Proc.-Electr., VOL. 151, NO 2, March 2004, pp. 135.
- [22] Barnouin R., Genta G., Magnetic Gears, Description and Application for Car Industry, Politecnico of Turin, 2016, pp. 36-37.
- [23] Tlali P.M., Wang R-J., Gerber S., Magnetic Gear Technologies: A Review, IEEE, 2014, pp. 545.
- [24] Neves C. G. C, Filho A. F. F., Coaxial Magnetic Gear: A Pedagogic Approach, Universidade Federal do Pampa (unipampa), 2015.
- [25] Bonisoli E., Dimauro L., Vigliani A., Velardocchia M., Repetto M., Cirimele V., Alotto P., Filippini M., Magnetic Gearshift System, WO2022013774A1, 2022
- [26] Liu X., Chau K. T., Jiang J. Z., Yu C., Design and analysis of interior-magnet outer-rotor concentric magnetic gears, Journal of Applied Physics 105, 07F101, 2009.
- [27] Cameron Z. A., Talerico T. T., Scheidler J. J, Lessons Learned in Fabrication of High-Specific_Torque Concentric Magnetic Gear, Independent Research and Development (IRAD) Program and Revolutionary Vertical Lift Technology (RVLT) Project, NASA, 2019, pp. 9.
- [28] Halim M. F. M. A., Sulaiman E., Aziz R., Othman R. N. F. K. R., Rahman A. A., Torque Density Design Optimization of Rotating Pole Piece Concentric Magnetic Gear, Arabian Journal for Science and Engineering, 2021.
- [29] Dimauro L., Bonisoli E., Power transmission systems: from traditional to magnetic gearboxes, Politecnico of Turin, 2022, pp. 99.
- [30] Pirra G., Repetto M., Dimauro L., Squillari P., REALIZATION OF A SYSTEM FOR CONTROLLING AND MEASURING THE PERFORMANCE OF A MAGNETIC GEARBOX, Politecnico of Turin, November 2021.
- [31] Filippini M., Alotto P., Cirimele V., Repetto M., Ragusa C., Dimauro L., Bonisoli E., Magnetic Loss Analysis in Coaxial Magnetic Gears, Politecnico of Turin, November 2019, pp. 10-14.
- [32] Dimauro L., Bonisoli E., Power transmission systems: from traditional to magnetic gearboxes, Politecnico of Turin, 2022, pp. 162.
- [33] Mateev V., Marinova I., Loss estimation of magnetic gears, Springer-Verlag GmbH Germany, November 2019, pp. 388.

